

AD-A259 765



## DOCUMENTATION PAGE

Form Approved  
OMB No. 0704-0188

2

Information is estimated to average 1 hour per response, including the time for reviewing instructions, searching existing data sources, gathering and reviewing the collection of information. Send comments regarding this burden estimate or any other aspect of this collection of information, including suggestions for reducing this burden, to Washington Headquarters Services, Directorate for Information Operations and Reports, 1215 Jefferson Avenue, 4302, and to the Office of Management and Budget, Paperwork Reduction Project (0704-0188), Washington, DC 20503.

1. AGENCY USE ONLY (Leave blank)		2. REPORT DATE 1-26-93		3. REPORT TYPE AND DATES COVERED Final 10/1/88 - 11/30/92	
4. TITLE AND SUBTITLE Active and Passive Remote Sensing of Ice				5. FUNDING NUMBERS  N00014-89-J-1107  425f023-08	
6. AUTHOR(S)  Prof. J.A. Kong					
7. PERFORMING ORGANIZATION NAME(S) AND ADDRESS(ES) Research Laboratory of Electronics Massachusetts Institute of Technology 77 Massachusetts Avenue Cambridge, MA 02139				8. PERFORMING ORGANIZATION REPORT NUMBER	
9. SPONSORING/MONITORING AGENCY NAME(S) AND ADDRESS(ES)  Office of Naval Research 800 North Quincy St. Arlington, VA 22217				10. SPONSORING/MONITORING AGENCY REPORT NUMBER	
11. SUPPLEMENTARY NOTES The view, opinions and/or findings contained in this report are those of the author(s) and should not be construed as an official Department of the Army position, policy, or decision, unless so designated by other documentation.					
12a. DISTRIBUTION/AVAILABILITY STATEMENT  Approved for public release; distribution unlimited.				12b. DISTRIBUTION CODE	
13. ABSTRACT (Maximum 200 words)  Work by Prof. Kong and his collaborators is summarized here  <div data-bbox="310 1394 680 1671" data-label="Text"> <p>DTIC SELECTE FEB 02 1993 S B</p> </div> <div data-bbox="908 1512 1311 1675" data-label="Text"> <p>34000 93-01796</p> </div>					
14. SUBJECT TERMS				15. NUMBER OF PAGES	
				16. PRICE CODE	
17. SECURITY CLASSIFICATION OF REPORT  UNCLASSIFIED		18. SECURITY CLASSIFICATION OF THIS PAGE  UNCLASSIFIED		19. SECURITY CLASSIFICATION OF ABSTRACT  UNCLASSIFIED	
				20. LIMITATION OF ABSTRACT  UL	

NSN 7540-01-280-5500

Standard Form 298 (Rev. 2-89)  
Prescribed by ANSI Std. Z39-18  
298-102

## GENERAL INSTRUCTIONS FOR COMPLETING SF 298

The Report Documentation Page (RDP) is used in announcing and cataloging reports. It is important that this information be consistent with the rest of the report, particularly the cover and title page. Instructions for filling in each block of the form follow. It is important to *stay within the lines* to meet optical scanning requirements.

**Block 1. Agency Use Only (Leave blank).**

**Block 2. Report Date.** Full publication date including day, month, and year, if available (e.g. 1 Jan 88). Must cite at least the year.

**Block 3. Type of Report and Dates Covered.** State whether report is interim, final, etc. If applicable, enter inclusive report dates (e.g. 10 Jun 87 - 30 Jun 88).

**Block 4. Title and Subtitle.** A title is taken from the part of the report that provides the most meaningful and complete information. When a report is prepared in more than one volume, repeat the primary title, add volume number, and include subtitle for the specific volume. On classified documents enter the title classification in parentheses.

**Block 5. Funding Numbers.** To include contract and grant numbers; may include program element number(s), project number(s), task number(s), and work unit number(s). Use the following labels:

C - Contract	PR - Project
G - Grant	TA - Task
PE - Program Element	WU - Work Unit Accession No.

**Block 6. Author(s).** Name(s) of person(s) responsible for writing the report, performing the research, or credited with the content of the report. If editor or compiler, this should follow the name(s).

**Block 7. Performing Organization Name(s) and Address(es).** Self-explanatory.

**Block 8. Performing Organization Report Number.** Enter the unique alphanumeric report number(s) assigned by the organization performing the report.

**Block 9. Sponsoring/Monitoring Agency Name(s) and Address(es).** Self-explanatory.

**Block 10. Sponsoring/Monitoring Agency Report Number.** (If known)

**Block 11. Supplementary Notes.** Enter information not included elsewhere such as: Prepared in cooperation with...; Trans. of...; To be published in.... When a report is revised, include a statement whether the new report supersedes or supplements the older report.

**Block 12a. Distribution/Availability Statement.** Denotes public availability or limitations. Cite any availability to the public. Enter additional limitations or special markings in all capitals (e.g. NOFORN, REL, ITAR).

DOD - See DoDD 5230.24, "Distribution Statements on Technical Documents."

DOE - See authorities.

NASA - See Handbook NHB 2200.2.

NTIS - Leave blank.

**Block 12b. Distribution Code.**

DOD - Leave blank.

DOE - Enter DOE distribution categories from the Standard Distribution for Unclassified Scientific and Technical Reports.

NASA - Leave blank.

NTIS - Leave blank.

**Block 13. Abstract.** Include a brief (Maximum 200 words) factual summary of the most significant information contained in the report.

**Block 14. Subject Terms.** Keywords or phrases identifying major subjects in the report.

**Block 15. Number of Pages.** Enter the total number of pages.

**Block 16. Price Code.** Enter appropriate price code (NTIS only).

**Blocks 17. - 19. Security Classifications.** Self-explanatory. Enter U.S. Security Classification in accordance with U.S. Security Regulations (i.e., UNCLASSIFIED). If form contains classified information, stamp classification on the top and bottom of the page.

**Block 20. Limitation of Abstract.** This block must be completed to assign a limitation to the abstract. Enter either UL (unlimited) or SAR (same as report). An entry in this block is necessary if the abstract is to be limited. If blank, the abstract is assumed to be unlimited.

## **FINAL REPORT**

**Title: ACTIVE AND PASSIVE REMOTE SENSING OF ICE**

**Sponsored by: Department of the Navy  
Office of Naval Research**

**Contract number: N00014-89-J-1107**

**Research Organization: Center for Electromagnetic Theory and Applications  
Research Laboratory of Electronics  
Massachusetts Institute of Technology**

**OSP number: 71367**

**Principal Investigator: J. A. Kong**

**Period covered: October 1, 1988 — November 30, 1992**

**ACTIVE AND PASSIVE REMOTE SENSING OF ICE**  
**FINAL REPORT**

This annual report covers research under the sponsorship of the ONR contract N00014-89-J-1107 from October 1, 1988 to September 30, 1992. We have published 44 journal and conference papers and 5 student theses during this period.

The theoretical approach that has been developed to interpret the polarimetric active measurements of saline ice is a random medium model using the radiative transfer theory. The ice layer is described as a host ice medium embedded with randomly distributed inhomogeneities, and the underlying sea water is considered to be a homogeneous halfspace. Multiple scattering effects are accounted for by solving the radiative transfer equations numerically. The effects of random roughness at the air - ice, and ice - water interfaces are accounted for by modifying the boundary conditions in the radiative transfer equations. Analysis of the model for reconstruction of sea ice parameters is made. An optimization approach is used for inversion. The discrepancy between the data and the results of the forward model is minimized by changing the inversion parameters according to a nonlinear programming scheme. Reconstruction of correlation lengths in the horizontal and vertical dimensions has been accomplished using the polarimetric backscattering coefficients at different angles of incidence as input data. Effects of data diversity and noise on the reconstruction of the physical parameters of sea ice from the backscattering coefficients are being investigated.

Recent theoretical works have suggested the potential of passive polarimetry in the remote sensing of geophysical media. It has been shown that the third Stokes parameter

$U$  of the thermal emission may become large for azimuthally asymmetric fields of observation. In one experiment, values of  $U$  of as high as 40 K were measured from a periodic triangular soil surface at 10 GHz. In order to investigate the potential applicability of passive polarimetry to the remote sensing of ocean surface, a numerical study of the polarimetric thermal emission from randomly rough ocean surface was performed. A Monte Carlo technique utilizing an exact method for calculating thermal emission was chosen for the study to avoid any of the limitations of the commonly used approximate methods in rough surface scattering.

In this Monte Carlo technique, a set of finite rough surface profiles in two dimensions with desired statistics was generated. Each finite surface was then extended periodically to create a set of infinite rough surfaces. The polarimetric thermal emission from each surface of the set was then calculated using both the extended boundary condition method and the method of moments. Finally, the results from the set were then averaged to obtain the estimate of the polarimetric brightness temperatures for the given surface statistics. The surface statistics chosen were intended to model a wind perturbed ocean surface in the  $X$  to  $X_u$  band microwave region. For this purpose, a power law surface spectrum corresponding to the capillary wave portion of the ocean spectrum was chosen with rms surface heights corresponding to wind speeds of up to 10 m/s. The effects of varying the azimuthal and polar looking angles, rms surface height, ocean permittivity, exponent of the power law spectrum, and the necessary high and low frequency cutoffs of the spectrum were investigated in this numerical study.

The results of the study indicate that the  $U$  parameter is sensitive to the azimuthal angle between the surface periodicity and the looking angle and to the rms height of the surface, and that the  $U$  parameter is fairly insensitive to variations in polar angle, permittivity, surface power law spectrum, and surface spectrum high frequency cutoff.

These properties give further strength to the idea of using the  $U$  parameter to detect wind direction over the ocean.

We studied an anisotropic layer model with ellipsoidal scatterers for applications to polarimetric remote sensing of geophysical media at microwave frequencies. The scattering configuration includes an isotropic layer covering an anisotropic layer above a homogeneous half space. The isotropic layer consists of randomly oriented spheroids. The anisotropic layer contains ellipsoidal scatterers with preferential vertical alignment and random azimuthal orientations. Effective permittivities of the scattering media are calculated with the strong permittivity theory extended to account for the non-spherical shapes and the scatterer orientation distributions. Based on the analytic wave theory, the dyadic Green's function for layer media is used to derive polarimetric backscattering coefficients under the distorted Born approximation. The ellipsoidal shape of the scatterers gives rise to non-zero cross-polarized returns from the untilted anisotropic medium even in the first order approximation. The effect of rough interface is estimated by incoherent addition method. Theoretical results and experimental data are matched at 9 GHz for thick first-year sea ice with bare surface and with snow cover at Point Barrow, Alaska. The model is then used to study the sensitivity of the scattering coefficients with respect to correlation lengths representing the geometry of brine inclusions in the model for sea ice. Finally, polarimetric signatures of bare and snow-covered sea ice are also simulated based on the model to investigate effects of different scattering mechanisms.

A model to calculate the effective permittivity of saline ice under thermal variation is presented in this paper. The model includes multi-phase inhomogeneities with multiple species characterized by orientation, size, and shape distributions. The model is then used to derive the effective permittivity as a function of temperature under the strong fluctuation theory which is extended to account for the complexity. The results calculated from the model are compared with experimental data at 4.8 GHz for saline ice grown at the

DTIC QUALITY INSPECTED 3

1A-1

SEARCHED	INDEXED
SERIALIZED	FILED
OCT 1980	
FBI - NEW YORK	
1	

US Army gold Regions Research and Engineering Laboratory (CRREL). The comparison between measured and calculated complex permittivities is good for the imaginary part and the difference is within 10% for the real part.

Fully polarimetric scattering of electromagnetic waves from snow and ice is studied with a multi-layered random medium model and applied to interpret experimental data obtained under laboratory controlled conditions such as CRRELEX. The snow layer is modeled as an isotropic random medium. The sea ice is described as an anisotropic random medium due to the nonspherical shape of brine inclusions. The underlying sea water is considered as a homogeneous half-space. The random media in both layers are characterized by three-dimensional correlation functions with variances and correlation lengths corresponding to the fluctuation strengths and the physical geometries of the inhomogeneities, respectively. The strong fluctuation theory is used to calculate the effective permittivities of the random media. The distorted Born approximation is then employed to obtain the covariance matrix which represents the fully polarimetric scattering properties of the snow-ice media. It has been shown that the polarimetric covariance matrix contains more information than the conventional scattering coefficients on the remotely sensed media.

In saline ice sheets under quiescent condition, the background ice grows in columnar form and saline water is trapped between ice platelets in the form of brine inclusions which are usually ellipsoidal. The ice tends to grow vertically downward rendering the ellipsoidal inclusions aligned preferably in the vertical direction and the crystallographic C axes parallel to the horizontal plane. In this case, the C axes are, however, random in azimuthal direction. The strong fluctuation theory is extended to account for vertically aligned ellipsoidal brine inclusions with C axes randomly oriented in the horizontal direction. The brine inclusions are described by three-dimensional local correlation functions.

The configuration average over the azimuthal orientation angles is carried out in the process of deriving the global correlation tensor. The distorted Born approximation is applied to obtain the covariance matrix for the multi-layered snow-ice configuration. The theoretical results show non-zero cross-polarized returns under the first-order distorted Born approximation. We have also compared the results with experimental data obtained by the US Army Cold Regions Research and Engineering Laboratory (CRREL).

In sea ice, the scatterers can have various shapes, sizes, and permittivities. We have also investigated the modeling of radar backscatter from random media with multiple scatterer species. We consider each type of scatterers as a species which can take on a shape, size, and complex permittivity different from other species. The multiple species in the random medium are considered as randomly oriented ellipsoids and described by multiple three-dimensional ellipsoidal local correlation functions. The variances and correlation lengths of the correlation functions characterize the fluctuation strengths and the physical geometries of each species of scatterers. The effective permittivity of the random medium is derived under the strong fluctuation theory and the polarimetric scattering coefficients are calculated for the layer configuration with the distorted Born approximation. Due to the non-spherical shape and the random orientation of the scatterers, the correlation coefficient between the HH and VV returns has a magnitude different from unity and a small phase angle. The scattering coefficients are also used to calculate the Mueller matrix for synthesis of polarization signatures. The co-polarized signature of the random medium has a rather straight distortion track and a recognizable pedestal.

Accurate calibration of polarimetric radar systems is essential for the polarimetric remote sensing of earth terrain. Polarimetric calibration algorithms using in-scene reflectors and distributed targets are studied. The transmitting and receiving ports of the polarimetric radar are modeled by two unknown polarization transfer matrices. These unknown matrices are determined using the the measured scattering matrices from the



calibration targets. For the case of polarimetric calibration using three in-scene reflectors, a Polarization-basis Transformation (PT) technique is introduced to find out a new transmitting and receiving polarization basis under which the scattering matrices of the calibration targets will fall into one of six simpler sets. The calibration solution can then be solved easily in the new polarization basis and converted to obtain the solution in the original polarization basis. The uniqueness of polarimetric calibration using three targets is addressed for all possible target combinations. The PT technique can also be applied to the polarimetric calibration using a combination of arbitrary in-scene reflectors and distributed targets. The effect of misalignment of calibration targets and the sensitivity of polarimetric calibration algorithms to the noise are illustrated by investigating several sets of calibration targets.

We have studied the SAR image classification by using the neural network methods. Supervised methods, including both conventional Maximum Likelihood (ML) and more recent multi-layer perceptron neural network classifiers have yielded higher accuracy than unsupervised techniques, but suffer from the need for human interaction to predetermine classes and training regions. In contrast, unsupervised methods determine classes automatically, but generally show limited ability to accurately divide terrain into natural classes. We introduced a new terrain classification technique to discriminate sea ice signatures in polarimetric SAR images by utilizing unsupervised neural networks to provide automatic classification, but employing an iterative algorithm which overcomes the poor accuracy of other unsupervised techniques.

Several types of unsupervised neural networks are first applied to the classification of SAR images, and the results are compared with those of more conventional unsupervised methods. Neural network approaches include Adaptive Resonance theory (ART), Learning Vector Quantization (LVQ), and Kohonen's self-organizing feature map. Conventional classifiers utilized are the migrating means clustering algorithm and the K-means clustering

method. Preprocessing is performed with the SAR images to reduce speckle noise and stabilize the training process for the neural networks. Results after preprocessing show that LVQ and Kohonen's self-organizing feature map outperform the conventional unsupervised classifiers, but are still inferior to supervised methods.

To overcome this poor accuracy, an iterative algorithm is constructed where the SAR image is reclassified using a Maximum Likelihood (ML) classifier. Training of the ML classifier is performed using a training data set first classified by the above unsupervised method, thus, requiring no human intervention, and preserving the unsupervised nature of the overall classification scheme. The process is then repeated iteratively, training a second ML classifier using data classified by the first. It is shown that this algorithm converges rapidly, and significantly improves classification accuracy. Performance after convergence is seen to be comparable to that obtained with a supervised ML classifier, while maintaining the advantages of an unsupervised technique.

The unsupervised and iterative techniques developed have been applied to the polarimetric SAR images of Beaufort sea ice acquired by the C-, L-, and P-band SAR instruments of Jet Propulsion Laboratory. The results obtained with the new algorithms are compared with the results obtained with other techniques by classifying terrain features in polarimetric SAR images.

A multivariate K-distribution has been developed to model the statistics of fully polarimetric radar data from earth terrain with polarizations HH, HV, VH, and VV. In this approach, correlated polarizations of radar signals, as characterized by a covariance matrix, are treated as the sum of  $N$  n-dimensional random vectors;  $N$  obeys the negative binomial distribution with a parameter  $\alpha$  and mean  $\bar{N}$ . Subsequently, an n-dimensional K-distribution, with either zero or nonzero mean, is developed in the limit of infinite  $\bar{N}$  or

illuminated area. The probability density function (PDF) of the K-distributed vector normalized by its Euclidean norm is independent of the parameter  $\alpha$  and is the same as that derived from a zero-mean Gaussian-distributed random vector. The above model is well supported by experimental data provided by MIT Lincoln Laboratory and the Jet Propulsion Laboratory in the form of polarimetric measurements. The results are illustrated by comparing the higher-order normalized intensity moments and cumulative density functions (CDF) of the experimental data with theoretical results of the K-distribution.

Among the various theoretical models applied to study the electromagnetic wave scatterings from geophysical terrain, such as snow and ice, the radiative transfer theory has drawn intensive attention in the microwave remote sensing society during the past years. In most of the scattering models, the volume scattering and the surface scattering effects have been investigated separately. Recently, there has been a growing interest in the construction of composite models which can take into account both types of scattering. We derived the first order iterative solution to the vector radiative transfer equations for a two-layer medium with a diffuse top boundary and an irregular bottom boundary of Gaussian roughness. The Kirchhoff approximation and the geometrical optics approach with shadowing correction are used in formulating the boundary conditions. To demonstrate the utilities of the theory, randomly oriented spheroidal discrete scatterer model is used to calculate the backscattering coefficients from soybean field in different growing stages and compared to the experimental measurements. Good agreement has been achieved for both the co-polarized and the cross-polarized data. It is observed that the presence of the rough surface can significantly enhance the backscattering at small incident angles and increase the cross-polarized returns. The polarization signatures calculated based on the Mueller matrix show a straight distortion track and an observable pedestal. Numerical comparison to the backscattering coefficients calculated by using planar bottom boundary conditions with or without the incoherent addition of the rough surface effects are also made.

The concept of polarimetry in active remote sensing is extended to passive remote sensing. The potential use of the third and fourth Stokes parameters  $U$  and  $V$ , which play an important role in polarimetric active remote sensing, is demonstrated for passive remote sensing. It is shown that, by the use of the reciprocity principle, the polarimetric parameters of passive remote sensing can be obtained through the solution of the associated direct scattering problem. In particular, the full polarimetric information, including the corresponding brightness temperatures of  $U$  and  $V$ , can be obtained from the solution of the direct scattering problem for four different polarizations of the incident wave. These ideas are applied to study polarimetric passive remote sensing of periodic surfaces. The solution of the direct scattering problem is obtained by an integral equation formulation. Incidence on a penetrable, lossy, medium is considered. Since the kernels of the integral equations are the periodic Green's functions and their normal derivatives on the surface, rapid evaluation of the slowly convergent series associated with these functions is observed to be critical for the feasibility of the method. The study has shown that the brightness temperature of the Stokes parameter  $U$  can be significant in passive remote sensing. Values as high as 50 K are observed for certain configurations.

To demonstrate the use of polarimetry in passive remote sensing of azimuthally asymmetric features on a terrain surface, an experiment was designed and implemented. A triangular corrugation pattern was made on the sandy soil surface. Polarimetric brightness temperatures are measured with horizontal, vertical, and 45° polarization orientations for various observation angles. From the measured temperatures, absolute values as high as 30–40 K of the third Stokes brightness temperatures are observed. A theoretical analysis of the data indicates that the high values of  $U$  are caused by the azimuthal asymmetry on the remotely sensed soil surface. It is also observed from the experiment that the brightness temperatures for all three Stokes parameters vary as the observation direction varies from being parallel to the surface row structure to being perpendicular to the row

structure. The significant implication of this experiment is that the surface asymmetry can be detected with a measurement of  $U$  at a single azimuthal angle.

## PUBLICATIONS SPONSORED BY THE ONR CONTRACT:

Polarimetric scattering model for inversion of sea ice parameters, (M. E. Veysoglu, J. A. Kong, and C. C. Hsu), submitted for presentation at the USRI General Assembly'93, Kyotok, Japan, August 25-September 2, 1993.

Polarimetric thermal emission from randomly rough ocean surfaces: a numerical study, (J. T. Johnson, R. T. Shin, J. A. Kong, S. H. Yueh, S. V. Nghiem, and R. Kwok), submitted for presentation on Applied Computational Electrodynamics Symposium, Monterey, California, March 22-26, 1993.

Anisotropic layer model with ellipsoidal scatterers (S. V. Nghiem, R. Kwok, J. A. Kong, and R. T. Shin), submitted for publication on Radio Science, August 1992.

Effective permittivity of saline ice under thermal variation (S. V. Nghiem, R. Kwok, J. A. Kong, R. T. Shin, A. J. Gow, and S. A. Arcone), International Geoscience and Remote Sensing Symposium, Houston, Texas, 26-29, May 1992.

Theoretical models for polarimetric microwave remote sensing of earth terrain (M. Borgeaud, J. A. Kong, R. T. Shin, and S. V. Nghiem), in Direct and Inverse Methods in Radar Polarimetry, Part 2, 1139-1190, Kluwer Academic Publishers, The Netherlands, 1992.

Polarimetric passive remote sensing of periodic surfaces (M. E. Veysoglu, H. A. Yueh, R. T. Shin, and J. A. Kong), *J. Electromag. Waves Applic.*, Vol. 5, No. 3, 267-280, 1991.

Polarimetric passive remote sensing of a periodic soil surface: Microwave measurements and analysis (S. V. Nghiem, M. E. Veysoglu, J. A. Kong, R. T. Shin, K. O'Neill, and A. W. Lohanick), *J. Electromag. Waves Applic.*, 1991. Vol. 5, No. 9, 997-1005, 1991.

Application of neural network to polarimetric SAR image classification (Y. Hara, R. G. Atkins, S. H. Yueh, R. T. Shin, J. A. Kong, and R. Kwok), *Progress in Electromag. Research Symposium*, Cambridge, Massachusetts, July 1-5, 1991.

Multiple ellipsoidal species in layer random medium model for polarimetric remote sensing (S. V. Nghiem, J. A. Kong, R. T. Shin, and T. Le Toan), *Progress in Electromag. Research Symposium*, Cambridge, Massachusetts, July 1-5, 1991.

Polarimetric passive remote sensing of an azimuthally asymmetric periodic soil surface (S. V. Nghiem, M. E. Veysoglu, J. A. Kong, R. T. Shin, K. O'Neill, and A. Lohanick), *Progress in Electromag. Research Symposium*, Cambridge, Massachusetts, July 1-5, 1991.

Polarimetric passive remote sensing of periodic surfaces (M. E. Veysoglu, H. A. Yueh, R. T. Shin, and J. A. Kong), *Progress in Electromag. Research Symposium*, Cambridge, Massachusetts, July 1-5, 1991.

Analytical solution of the vector radiative transfer equation with rough surface boundary condition (H. C. Han, J. A. Kong, S. V. Nghiem, and T. Le Toan), *Progress in Electromag. Research Symposium*, Cambridge, Massachusetts, July 1-5, 1991.

External calibration of polarimetric radars using point and distributed targets (S. H. Yueh, J. A. Kong, and R. T. Shin), *Second Annual JPL Airborne Geoscience Workshop*, JPL, Pasadena, CA, May 20-24, 1991

Application of neural networks to radar image classification (Y. Hara, R. G. Atkins, S. H. Yueh, R. T. Shin, and J. A. Kong), submitted for publication in *IEEE Trans. Geoscience Remote Sensing*, 1991.

K-distribution and multi-frequency polarimetric terrain radar clutter (H. A. Yueh, J. A. Kong, R. T. Shin, H. A. Zebker, and T. Le Toan), *J. Electromag. Waves Applic.*, Vol. 5, No. 1, 1-15, 1991.

Calibration of polarimetric radars using in-scene reflectors (S. H. Yueh, J. A. Kong, and R. T. Shin), *Progress In Electromag. Research*, edited by J. A. Kong, Chapter 9, Vol. 3, 451-510, Elsevier, New York, 1990.

Classification and maximum contrast of earth terrain using polarimetric synthetic aperture radar images (J. A. Kong, S. H. Yueh, H. H. Lim, R. T. Shin, and J. J. van Zyl), *Progress In Electromag. Research*, edited by J. A. Kong, Chapter 6, Vol. 3, 327-370, Elsevier, New York, 1990.

Scattering from randomly oriented scatterers with strong permittivity fluctuations (H. A. Yueh, R. T. Shin, and J. A. Kong), *J. Electromag. Waves Applic.*, Vol. 4, No. 10, 983-1004, 1990.

Polarimetric remote sensing of geophysical media with layer random medium model (S. V. Nghiem, M. Borgeaud, J. A. Kong, and R. T. Shin), *Progress in Electromag. Research*, edited by J. A. Kong, Chapter 1, Vol. 3, 1-73, Elsevier, 1990.

Theoretical models and experimental measurements for polarimetric remote sensing of snow and sea ice (S. V. Nghiem, J. A. Kong, R. T. Shin, H. A. Yueh, and R. Onstott), *URSI International Commission F meeting*, Hyannis, Massachusetts, May 16-18, 1990.

Calibration of polarimetric radars using in-scene reflectors (S. H. Yueh, J. A. Kong, and R. T. Shin), *10th International Geoscience & Remote Sensing Symposium*, College Park, Maryland, May 20-24, 1990.

Correlation function for a random collection of discrete scatterers (H. H. Lim, S. H. Yueh, R. T. Shin, and J. A. Kong), *10th International Geoscience & Remote Sensing Symposium*, College Park, Maryland, May 20-24, 1990.

Statistical modeling for polarimetric remote sensing of earth terrain (S. H. Yueh, J. A. Kong, R. T. Shin, and H. A. Zebker), *10th International Geoscience & Remote Sensing Symposium*, College Park, Maryland, May 20-24, 1990.

Study of polarimetric response of sea ice with layered random medium model (S. V. Nghiem, J. A. Kong, and R. T. Shin), *10th International Geoscience & Remote Sensing Symposium*, (IGARSS'90), College Park, Maryland, USA, May 20-24, 1990.

Electromagnetic wave modeling for remote sensing (S. V. Nghiem, J. A. Kong, and T. Le Toan), *International Conference on Directions in Electromagnetic Wave Modeling*, New York, October 22-24, 1990.

K-distribution and polarimetric terrain radar clutter (S. H. Yueh, J. A. Kong, J. K. Jao, R. T. Shin, H. A. Zebker, T. Le Toan, and H. Öttl), *Progress in Electromag. Research*, edited by J. A. Kong, Chapter 4, Vol. 3, 237-275, Elsevier, 1990.

Calibration of polarimetric radar using in-scene reflectors (H. A. Yueh, J. A. Kong, R. M. Barnes, and R. T. Shin), *J. Electromag. Waves Applic.*, Vol. 4, No. 1, 27-48, 1990.

Application of three-layer random medium model for microwave remote sensing of snow-covered sea ice (F. C. Lin, J. A. Kong, and R. T. Shin), *J. Geophysical Research*, 1989.

Classification of earth terrain using synthetic aperture radar images (H. H. Lim, A. A. Swartz, H. A. Yueh, J. A. Kong, R. T. Shin, and J. J. van Zyl), *J. Geophysical Research*, Vol. 94, No. B6, 7049-7057, June 10, 1989.

Radiative transfer theory for active remote sensing of two-layer random medium (R. T. Shin and J. A. Kong), *Progress In Electromag. Research*, Elsevier, New York, Vol. 1, Chapter 5, 359-417, 1989.

Scattering from randomly perturbed periodic and quasiperiodic surfaces (H. A. Yueh, R. T. Shin, and J. A. Kong), *Progress In Electromag. Research*, Elsevier, New York, Vol. 1, Chapter 4, 297-358, 1989.

Contrast and classification studies of polarimetric SAR images for remote sensing of earth terrain (H. H. Lim, H. A. Yueh, J. A. Kong, R. T. Shin, and J. J. van Zyl), *Progress in Electromag. Research Symposium*, Boston, Massachusetts, July 25-27, 1989.

K-distribution and polarimetric terrain radar clutter (H. A. Yueh, J. A. Kong, J. K. Jao, R. T. Shin, and L. M. Novak), *Progress in Electromag. Research Symposium*, Boston, Massachusetts, July 25-26, 1989.

Calibration of polarimetric radars using in-scene reflectors (H. A. Yueh, J. A. Kong, R. M. Barnes, and R. T. Shin), *Progress in Electromag. Research Symposium*, Boston, Massachusetts, July 25-26, 1989.

Three-layer random medium model for fully polarimetric remote sensing of geophysical media (S. V. Nghiem, F. C. Lin, J. A. Kong, R. T. Shin, and H. A. Yueh), *Progress in Electromag. Research Symposium*, Boston, Massachusetts, July 25-26, 1989.

Correlation function study for random media with multiphase mixtures (F. C. Lin, H. A. Yueh, J. A. Kong and R. T. Shin), *Progress in Electromag. Research Symposium*, Boston, Massachusetts, July 25-26, 1989.



Polarimetric remote sensing of earth terrain with two-layer random medium model (M. Borgeaud, J. A. Kong, R. T. Shin, and S. V. Nghiem), *Progress in Electromag. Research Symposium*, Boston, Massachusetts, July 25-26, 1989.

Application of three-layer random medium model to polarimetric remote sensing of snow and sea ice (S. V. Nghiem, J. A. Kong, R. T. Shin, and H. A. Yueh), *North American Sea Ice Work Shop*, Amherst, Massachusetts, June 26-28, 1989.

Theoretical models for polarimetric microwave remote sensing of earth terrain (M. Borgeaud, S. V. Nghiem, R. T. Shin, and J. A. Kong), *J. Electromag. Waves and Application*, Vol. 3, No. 1, 61-81, 1988.

The optimal polarizations for achieving maximum contrast in radar polarimetry (A. A. Swartz, H. A. Yueh, J. A. Kong, L. M. Novak, and R. T. Shin), *J. Geophysical Research*, Vol. 93, No. B12, 15235-15260, 1988.

Bayes classification of terrain cover using normalized polarimetric data (H. A. Yueh, A. A. Swartz, J. A. Kong, R. T. Shin, and L. M. Novak), *J. Geophysical Research*, Vol. 93, No. B12, 15261-15267, 1988.

Correlation function study for sea ice (F. C. Lin, J. A. Kong, R. T. Shin, A. J. Gow, and S. A. Arcone), *J. Geophysical Research*, Vol. 93, No. C11, 14055-14063, November 1988.

Polarimetric remote sensing of earth terrain with three-layer random medium model (S. V. Nghiem, F. C. Lin, J. A. Kong, R. T. Shin, and H. A. Yueh), MIT Research Lab. of Electronics, EWT-RS124-8810, 1988.

Theoretical models for polarimetric microwave remote sensing of earth terrain (M. Borgeaud, J. A. Kong, R. T. Shin, and S. V. Nghiem), *Proceedings of the 1988 NATO Advanced Research Workshop*, Nuremberg, Germany, 1988.

Office of Naval Research

DISTRIBUTION LIST

Charles A. Luther

Code: 1121 R5  
Office of Naval Research  
800 North Quincy Street  
Arlington, VA 22217

3 copies

Administrative Contracting Officer  
E19-628  
Massachusetts Institute of Technology  
Cambridge, MA 02139

1 copy

Director  
Naval Research Laboratory  
Washington, DC 20375  
Attn: Code 2627

18 <sup>copy</sup> copies

Defense Technical Information Center  
Bldg. 5, Cameron Station  
Alexandria, VA 22314

2 copies

## F2: Remote sensing of sea ice

### Polarimetric Scattering Model For Reconstruction of Sea Ice Parameters

M. E. Veysoglu, J. A. Kong, C. C. Hsu  
Department of Electrical Engineering and Computer Science  
Massachusetts Institute of Technology  
Cambridge, MA 02139  
(Phone: 617-253-8535, Fax: 617-253-0987)

#### Abstract

To interpret the polarimetric active remote sensing data of saline ice, we have developed a random medium model using the radiative transfer theory. The ice layer is described as a host ice medium embedded with randomly distributed inhomogeneities, and the underlying sea water is considered to be a homogeneous halfspace. The random medium model is characterized by a correlation function described by correlation lengths in both the horizontal and vertical directions. Multiple scattering effects are accounted for by solving the radiative transfer equations numerically. The effects of random roughness at the air - ice, and ice - water interfaces are accounted for by modifying the boundary conditions in the radiative transfer equations. Analysis of the model for reconstruction of sea ice parameters is made. An optimization approach is used for inversion. The discrepancy between the data and the results of the forward model is minimized by changing the inversion parameters according to a nonlinear programming scheme. Reconstruction of correlation lengths in the horizontal and vertical dimensions has been accomplished using the polarimetric backscattering coefficients at different angles of incidence as input data. Effects of data diversity and noise on the reconstruction of the physical parameters of sea ice from the backscattering coefficients are being investigated.

# **Polarimetric Thermal Emission from Randomly Rough Ocean Surfaces: A Numerical Study**

**J. T. Johnson, R. T. Shin, and J. A. Kong**  
Department of Electrical Engineering and Computer Science  
and Research Laboratory of Electronics  
Massachusetts Institute of Technology, Cambridge, MA

**S. H. Yueh, S. V. Nghiem, and R. Kwok**  
Jet Propulsion Laboratory  
California Institute of Technology, Pasadena, CA

Recent theoretical works have suggested the potential of passive polarimetry in the remote sensing of geophysical media. It has been shown that the third Stokes parameter  $U$  of the thermal emission may become large for azimuthally asymmetric fields of observation. In one experiment, values of  $U$  of as high as 40 K were measured from a periodic triangular soil surface at 10 GHz. In order to investigate the potential applicability of passive polarimetry to the remote sensing of ocean surface, a numerical study of the polarimetric thermal emission from randomly rough ocean surfaces was performed. A Monte Carlo technique utilizing an exact method for calculating thermal emission was chosen for the study to avoid any of the limitations of the commonly used approximate methods in rough surface scattering.

In this Monte Carlo technique, a set of finite rough surface profiles in two dimensions with desired statistics was generated. Each finite surface was then extended periodically to create a set of infinite rough surfaces. The polarimetric thermal emission from each surface of the set was then calculated using both the extended boundary condition method and the method of moments. Finally, the results from the set were then averaged to obtain the estimate of the polarimetric brightness temperatures for the given surface statistics. The surface statistics chosen were intended to model a wind perturbed ocean surface in the  $X$  to  $K_u$  band microwave region. For this purpose, a power law surface spectrum corresponding to the capillary wave portion of the ocean spectrum was chosen with rms surface heights corresponding to wind speeds of up to 10 m/s. The effects of varying the azimuthal and polar looking angles, rms surface height, ocean permittivity, exponent of the power law spectrum, and the necessary high and low frequency cutoffs of the spectrum were investigated in this numerical study.

The results of the study indicate that the  $U$  parameter is sensitive to the azimuthal angle between the surface periodicity and the looking angle and to the rms height of the surface, and that the  $U$  parameter is fairly insensitive to variations in polar angle, permittivity, surface power law spectrum, and surface spectrum high frequency cutoff. These properties give further strength to the idea of using the  $U$  parameter to detect wind direction over the ocean.

# Anisotropic Layer Model with Ellipsoidal Scatterers

S. V. Nghiem and R. Kwok

Jet Propulsion Laboratory  
California Institute of Technology  
Pasadena, California 91109

J. A. Kong and R. T. Shin

Department of Electrical Engineering and Computer Science  
and Research Laboratory of Electronics  
Massachusetts Institute of Technology  
Cambridge, Massachusetts 02139

**Abstract** – This paper presents an anisotropic layer model with ellipsoidal scatterers for applications to polarimetric remote sensing of geophysical media at microwave frequencies. The scattering configuration includes an isotropic layer covering an anisotropic layer above a homogeneous half space. The isotropic layer consists of randomly oriented spheroids. The anisotropic layer contains ellipsoidal scatterers with preferential vertical alignment and random azimuthal orientations. Effective permittivities of the scattering media are calculated with the strong permittivity theory extended to account for the non-spherical shapes and the scatterer orientation distributions. Based on the analytic wave theory, the dyadic Green's function for layer media is used to derive polarimetric backscattering coefficients under the distorted Born approximation. The ellipsoidal shape of the scatterers gives rise to non-zero cross-polarized returns from the untilted anisotropic medium even in the first order approximation. The effect of rough interface is estimated by incoherent addition method. Theoretical results and experimental data are matched at 9 GHz for thick first-year sea ice with bare surface and with snow cover at Point Barrow, Alaska. The model is then used to study the sensitivity of the scattering coefficients with respect to correlation lengths representing the geometry of brine inclusions in the model for sea ice. Finally, polarimetric signatures of bare and snow-covered sea ice are also simulated based on the model to investigate effects of different scattering mechanisms.

## 1. INTRODUCTION

Technology in remote sensing has been advanced considerably especially for airborne and space borne radar with multi-frequency and multi-polarization capabilities. Theoretical models have been developed to interpret multi-frequency polarimetric data for remote sensing of geophysical media. Several approaches including radiative transfer, modified radiative transfer, and analytic wave theory have been considered in model developments [1]. The analytical wave theory, while remains mathematically tractable for some complexity of the media, preserves the phase information which is appropriate for the calculation of polarimetric scattering coefficients [2]. Under the Born approximation for sparse and tenuous media, conventional scattering coefficients have been derived for isotropic multi-layer [3], anisotropic layer [4], and isotropic-anisotropic layer [5] configurations. Fully polarimetric scattering coefficients have also been calculated for isotropic [6] and anisotropic [7] layer configurations. In these models, the scatterers are spherical or spheroidal and the cross-polarized returns come from second (or higher) order [8] or the tilted anisotropy [4]. For denser or less tenuous media, the distorted Born approximation has been applied [9-11]. This approximation considers dissipation loss, scattering loss, and the modification of wave speed due to the scatterers; thus, multiple scattering has been included to some extent. For media with strong permittivity fluctuations, the strong permittivity fluctuation theory is used in conjunction with the distorted Born approximation [12]. In this case, conventional backscattering coefficients have been computed for an isotropic half-space [13], an anisotropic half-space [14], and a configuration for an isotropic layer of spherical scatterers above an anisotropic layer of aligned spheroids [15].

In this paper, the isotropic-anisotropic layer configuration containing non-spherical scatterers is considered to obtain fully polarimetric backscattering coefficients for geophysical media. The scattering configuration is illustrated in Figure 1 where  $\theta_0$  is the incident angle. The covering isotropic layer is composed of randomly oriented spheroids as described in reference [16]. In the anisotropic layer, the scatterers are modeled with an ellipsoidal correlation function with the orientation characterized by a probability density function of the Eulerian rotation angles. The orientation of the ellipsoids is vertically aligned and azimuthally random. The strong permittivity fluctuation theory is extended to calculate the effective permittivities and the distorted Born approximation is applied to derive the polarimetric scattering coefficients. Theoretical results are compared with measured data for bare and snow-covered sea ice. The effects of rough interfaces are also estimated by the incoherent addition approach [4]. Variations of polarimetric backscatter are studied for various correlation lengths and polarization signatures of sea ice are simulated and discussed for different scattering mechanisms. Following this plan, the paper consists of 5 sections. Section 2 is for effective permittivities, Section 3 for polarimetric scattering coefficients, Section 4 for results and discussion, and finally Section 5 for the summary.

## 2. EFFECTIVE PERMITTIVITY

In the isotropic scattering medium of Region 1 in Figure 1, the embedded scatterers are modeled as spheroids and the effective permittivity has been derived under the strong fluctuation theory and reported in [16,17]. In the anisotropic medium, the ellipsoidal scatterers have preferential alignment resulting in the effective anisotropy. The effective permittivity tensor of the scattering anisotropic medium will be calculated in this section for the ellipsoids with vertical alignment and random azimuthal orientations.

In an inhomogeneous medium such as sea ice, sea water is trapped in an ice medium in form of brine inclusions which are usually ellipsoidal. The ice tends to grow vertically downward rendering the ellipsoidal inclusions aligned preferentially in the vertical direction. In the absence of sea currents, the crystallographic c-axes are random in the horizontal plane as seen in Figure 2, which depicts a horizontal thin section of sea ice. Consequently, the minor axes of the ellipsoids have random orientations parallel to the horizontal plan. In this model, a correlation function corresponding locally to a scatterer is used in the derivation of the effective permittivity with the strong permittivity fluctuation theory, extended to account for the orientations of the ellipsoidal scatterers. When the average process is performed over orientation angle  $\phi_f$  shown in Figure 3, the effective permittivity is an untilted uniaxial tensor with vertical optic axis, which effectively manifests the azimuthal symmetry of the inhomogeneous medium.

Let  $\epsilon_b$  be the permittivity of the host medium and  $\epsilon_s$  be the permittivity of the embedded ellipsoidal scatterers occupying a total fractional volume of  $f_s$ . The subscript for the anisotropic medium (Region 2) is omitted in this section for convenience since the following derivation is for Region 2 only. Similar to the method in [12], auxiliary permittivity  $\bar{\epsilon}_g = \text{diag}[\epsilon_{g\rho}, \epsilon_{g\rho}, \epsilon_{gz}]$  is introduced into the wave equation for latter consideration of the singularity in anisotropic dyadic Green's function  $\bar{\bar{G}}_g(\bar{r}, \bar{r}')$ . The singularity is accounted for by decomposing  $\bar{\bar{G}}_g(\bar{r}, \bar{r}') = \bar{\bar{G}}_g(\bar{r} - \bar{r}')$  into a principal value part and a Dirac delta part with dyadic coefficient  $\bar{\bar{S}}$  which, in this case, is a diagonal tensor with three distinctive diagonal elements  $S_{x'}$ ,  $S_{y'}$ , and  $S_{z'}$  in the local coordinates  $(x', y', z')$ . These coordinates are related to the global coordinates  $(x, y, z)$  by the Eulerian rotation tensor

$$\bar{\bar{T}} = \begin{bmatrix} \cos \phi_f & \sin \phi_f & 0 \\ -\sin \phi_f & \cos \phi_f & 0 \\ 0 & 0 & 1 \end{bmatrix} \quad (1)$$

The effective permittivity of the inhomogeneous medium is composed of a quasi-static part and a scattering-effect part which accounts for the attenuation and the modification in the wave speed due to the inhomogeneities

$$\bar{\epsilon}_{eff} = \bar{\epsilon}_g + \epsilon_0 \left[ \bar{\bar{I}} - \bar{\bar{\xi}}_{eff} \cdot \langle \bar{\bar{S}} \rangle \right]^{-1} \cdot \bar{\bar{\xi}}_{eff} \quad (2)$$

where auxiliary permittivity  $\bar{\epsilon}_g$  and dyadic coefficient  $\langle \bar{S} \rangle$ , which is the ensemble average of  $\bar{S}$ , are determined by the condition of secular-term elimination. The effective dyadic scatterer  $\bar{\xi}_{eff}$ , under the low-frequency approximation, is given by

$$[\bar{\xi}_{eff}]_{jm} = \int_0^{2\pi} d\phi_f p(\phi_f) \sum_{k,l}^{x,y,z} \Gamma_{\xi jklm}^{(0)} \left\{ k_0^2 \int_{-\infty}^{\infty} d\bar{k}' [\bar{G}_g(\bar{k}')]_{kl} \Phi_{\xi}(\bar{k}') + [\bar{S}]_{kl} \right\} \Big|_{\phi_f} \quad (3)$$

in which  $p(\phi_f)$  is the probability density function of orientation angle  $\phi_f$ ,  $\Gamma_{\xi jklm}^{(0)}$  is the variance defined in [2],  $k_0$  is the free-space wave number, and  $\Phi_{\xi}$  is the Fourier transform of the normalized local correlation function. The anisotropic Green's function  $\bar{G}_g$  [12], which is invariant under the azimuthal Eulerian rotation (1), is expressed in the  $k'$  domain as

$$\begin{aligned} \bar{G}_g(\bar{k}') &= \frac{1}{(k_x'^2 + k_y'^2)D_o(\bar{k}')} \begin{bmatrix} k_y'^2 & -k_x'k_y' & 0 \\ -k_x'k_y' & k_x'^2 & 0 \\ 0 & 0 & 0 \end{bmatrix} + \\ &\frac{1}{(k_x'^2 + k_y'^2)D_e(\bar{k}')} \begin{bmatrix} k_x'^2 & k_x'k_y' & 0 \\ k_x'k_y' & k_y'^2 & 0 \\ 0 & 0 & \frac{k_{gz}^2}{k_{gz}^2}(k_x'^2 + k_y'^2) \end{bmatrix} - \frac{\bar{k}'\bar{k}'}{k_{gz}^2 D_e(\bar{k}')} \end{aligned} \quad (4a)$$

where the quantities  $D_o(\bar{k}')$ ,  $D_e(\bar{k}')$ ,  $k_{g\rho}^2$ , and  $k_{gz}^2$  are in the following equations with angular frequency  $\omega$  and permeability  $\mu_0$

$$D_o(\bar{k}') = k_x'^2 + k_y'^2 + k_z'^2 - k_{g\rho}^2 \quad (4b)$$

$$D_e(\bar{k}') = k_z'^2 + \frac{k_{g\rho}^2}{k_{gz}^2}(k_x'^2 + k_y'^2 - k_{gz}^2) \quad (4c)$$

$$k_{g\rho}^2 = \omega^2 \mu_0 \epsilon_{g\rho}, \text{ and } k_{gz}^2 = \omega^2 \mu_0 \epsilon_{gz} \quad (4d)$$

As in (2), the effective permittivity has been approximated by truncating the series in the renormalization method. The validity condition for the approximation is  $|\bar{\xi}_{eff}(\bar{k})|_{jm} \ll 1$ .

The ellipsoidal scatterer is described with a normalized local correlation function of the form

$$R_{\xi}(\bar{r}') = \exp \left( -\sqrt{\frac{x'^2}{\ell_{x'}^2} + \frac{y'^2}{\ell_{y'}^2} + \frac{z'^2}{\ell_{z'}^2}} \right) \quad (5a)$$

with correlation length  $\ell_{x'}$ ,  $\ell_{y'}$ , and  $\ell_{z'}$  in the local coordinates corresponding to the minor, the meridian, and the major axes of the scatterer. In this model, the correlation lengths are related to the effective size and shape of the scatterers. This local correlation function



can be reduced to spheroidal shape for two equal correlation lengths and to spherical shape for three identical correlation lengths. Applying the Fourier transform on (5a) yields

$$\Phi_{\xi}(\vec{k}') = \frac{\ell_{x'}\ell_{y'}\ell_{z'}}{\pi^2(1 + k_{x'}^2\ell_{x'}^2 + k_{y'}^2\ell_{y'}^2 + k_{z'}^2\ell_{z'}^2)^2} \quad (5b)$$

For random horizontal orientations with no preference in azimuthal direction, the probability density function of orientation is simply

$$p(\phi_f) = 1/(2\pi) \quad (6)$$

To calculate the effective permittivity according to (2),  $\bar{\epsilon}_g$  and  $\langle \bar{S} \rangle$  need be determined. Due to the global azimuthal symmetry, auxiliary permittivity  $\bar{\epsilon}_g$  in the coordinate  $(x, y, z)$  is uniaxial as afore indicated and the elements in  $\bar{\epsilon}_g$  are subjected to the condition  $\langle \bar{\xi} \rangle = 0$  such that

$$\begin{aligned} \langle \bar{\xi} \rangle &= \int_0^{2\pi} d\phi_f p(\phi_f) \bar{T}^{-1} \cdot \left\langle \begin{bmatrix} \xi_{x'} & 0 & 0 \\ 0 & \xi_{y'} & 0 \\ 0 & 0 & \xi_{z'} \end{bmatrix} \right\rangle \cdot \bar{T} \\ &= \frac{1}{2} \left\langle \begin{bmatrix} \xi_{x'} + \xi_{y'} & 0 & 0 \\ 0 & \xi_{x'} + \xi_{y'} & 0 \\ 0 & 0 & 2\xi_{z'} \end{bmatrix} \right\rangle = 0 \end{aligned} \quad (7)$$

Local quantities  $\xi_{x'}$ ,  $\xi_{y'}$ , and  $\xi_{z'}$  in (7) are related to the elements of dyadic coefficient  $\bar{S} = \text{diag}[S_{x'}, S_{y'}, S_{z'}]$  by

$$\xi_{x'}(\epsilon) = \frac{\epsilon - \epsilon_{g\rho}}{\epsilon_0 + S_{x'}(\epsilon - \epsilon_{g\rho})} \quad (8a)$$

$$\xi_{y'}(\epsilon) = \frac{\epsilon - \epsilon_{g\rho}}{\epsilon_0 + S_{y'}(\epsilon - \epsilon_{g\rho})} \quad (8b)$$

$$\xi_{z'}(\epsilon) = \frac{\epsilon - \epsilon_{gz}}{\epsilon_0 + S_{z'}(\epsilon - \epsilon_{gz})} \quad (8c)$$

where  $\epsilon$  can take on the value of  $\epsilon_s$  in a scatterer or  $\epsilon_b$  in the background medium. From (7) and (8),  $\epsilon_{g\rho}$  and  $\epsilon_{gz}$  can be written as, respectively,

$$\begin{aligned} \epsilon_{g\rho} &= \epsilon_b + f_s \frac{\epsilon_s - \epsilon_{g\rho}}{1 - f_s} \frac{2\epsilon_0 + (S_{x'} + S_{y'}) (\epsilon_s - \epsilon_{g\rho})}{2\epsilon_0 + (S_{x'} + S_{y'}) (\epsilon_b - \epsilon_{g\rho})} \\ &\quad \frac{\epsilon_0 + S_{x'} (\epsilon_b - \epsilon_{g\rho})}{\epsilon_0 + S_{x'} (\epsilon_s - \epsilon_{g\rho})} \frac{\epsilon_0 + S_{y'} (\epsilon_b - \epsilon_{g\rho})}{\epsilon_0 + S_{y'} (\epsilon_s - \epsilon_{g\rho})} \end{aligned} \quad (9a)$$

$$\epsilon_{gz} = \epsilon_b + f_s \frac{\epsilon_s - \epsilon_{gz}}{1 - f_s} \frac{\epsilon_0 + S_{z'} (\epsilon_b - \epsilon_{gz})}{\epsilon_0 + S_{z'} (\epsilon_s - \epsilon_{gz})} \quad (9b)$$

The average dyadic coefficient  $\langle \bar{S} \rangle$  in the global coordinates is obtained by the averaging integration over the probability density function of orientation

$$\begin{aligned} \langle \bar{S} \rangle &= \int_0^{2\pi} d\phi_f p(\phi_f) \bar{T}^{-1} \cdot \begin{bmatrix} S_{x'} & 0 & 0 \\ 0 & S_{y'} & 0 \\ 0 & 0 & S_{z'} \end{bmatrix} \cdot \bar{T} \\ &= \frac{1}{2} \begin{bmatrix} S_{x'} + S_{y'} & 0 & 0 \\ 0 & S_{x'} + S_{y'} & 0 \\ 0 & 0 & 2S_{z'} \end{bmatrix} = \begin{bmatrix} S_\rho & 0 & 0 \\ 0 & S_\rho & 0 \\ 0 & 0 & S_z \end{bmatrix} \end{aligned} \quad (10)$$

The coefficients  $S_{x'}$ ,  $S_{y'}$ , and  $S_{z'}$  are derived from the secular elimination condition [12] which renders

$$S_{x'} = \int_0^{2\pi} d\phi \frac{\epsilon_0 \gamma_x^2 \cos^2 \phi}{2\pi \epsilon_{g\rho} a \sqrt{a}} [(1+a) \tan^{-1} \sqrt{a} - \sqrt{a}] \quad (11a)$$

$$S_{y'} = \int_0^{2\pi} d\phi \frac{\epsilon_0 \gamma_y^2 \sin^2 \phi}{2\pi \epsilon_{g\rho} a \sqrt{a}} [(1+a) \tan^{-1} \sqrt{a} - \sqrt{a}] \quad (11b)$$

$$S_{z'} = \int_0^{2\pi} d\phi \frac{\epsilon_0 (1+a)}{2\pi \epsilon_{gz} a \sqrt{a}} [\sqrt{a} - \tan^{-1} \sqrt{a}] \quad (11c)$$

where the values of both the square root and the inverse tangent are chosen on the principal Riemann sheets with branch cuts on the negative real axis. In (11), the integrations over  $\phi$  can be carried out numerically and quantities  $a$ ,  $\gamma_x$ , and  $\gamma_y$  are defined as

$$a = \alpha \gamma^2 - 1, \quad \alpha = \frac{\epsilon_{gz}}{\epsilon_{g\rho}} \quad (12a)$$

$$\gamma = \frac{1}{\ell_{z'}} \left( \frac{\cos^2 \phi}{\ell_{x'}^2} + \frac{\sin^2 \phi}{\ell_{y'}^2} \right)^{-\frac{1}{2}} \quad (12b)$$

$$\gamma_x = \frac{1}{\ell_{x'}} \left( \frac{\cos^2 \phi}{\ell_{x'}^2} + \frac{\sin^2 \phi}{\ell_{y'}^2} \right)^{-\frac{1}{2}} \quad (12c)$$

$$\gamma_y = \frac{1}{\ell_{y'}} \left( \frac{\cos^2 \phi}{\ell_{x'}^2} + \frac{\sin^2 \phi}{\ell_{y'}^2} \right)^{-\frac{1}{2}} \quad (12d)$$

Also due to the azimuthal symmetry of the scattering medium, the effective scatterer tensor  $\bar{\xi}_{eff}$  has the uniaxial form

$$\bar{\xi}_{eff} = \begin{bmatrix} \xi_{eff\rho} & 0 & 0 \\ 0 & \xi_{eff\rho} & 0 \\ 0 & 0 & \xi_{effz} \end{bmatrix} \quad (13)$$

which is obtained by substituting the Green's function, the correlation function, and the probability density function of orientation into (3). The integrations are carried out with the procedure in [2,17]. Followed is how to compute  $\bar{\xi}_{eff}$  :

$$\xi_{eff\rho} = \frac{1}{2} [\delta_{\xi x'} (I_{x'} + S_{x'}) + \delta_{\xi y'} (I_{y'} + S_{y'})] \quad (14a)$$

$$\xi_{effz} = \delta_{\xi z'} (I_{z'} + S_{z'}) \quad (14b)$$

where variance  $\delta_{\xi x'}$ ,  $\delta_{\xi y'}$ , and  $\delta_{\xi z'}$  are respectively determined by

$$\delta_{\xi x'} = \left[ \frac{\epsilon_b - \epsilon_{g\rho}}{\epsilon_0 + S_{x'}(\epsilon_b - \epsilon_{g\rho})} \right]^2 (1 - f_s) + \left[ \frac{\epsilon_s - \epsilon_{g\rho}}{\epsilon_0 + S_{x'}(\epsilon_s - \epsilon_{g\rho})} \right]^2 f_s \quad (15a)$$

$$\delta_{\xi y'} = \left[ \frac{\epsilon_b - \epsilon_{g\rho}}{\epsilon_0 + S_{y'}(\epsilon_b - \epsilon_{g\rho})} \right]^2 (1 - f_s) + \left[ \frac{\epsilon_s - \epsilon_{g\rho}}{\epsilon_0 + S_{y'}(\epsilon_s - \epsilon_{g\rho})} \right]^2 f_s \quad (15b)$$

$$\delta_{\xi z'} = \left[ \frac{\epsilon_b - \epsilon_{gz}}{\epsilon_0 + S_{z'}(\epsilon_b - \epsilon_{gz})} \right]^2 (1 - f_s) + \left[ \frac{\epsilon_s - \epsilon_{gz}}{\epsilon_0 + S_{z'}(\epsilon_s - \epsilon_{gz})} \right]^2 f_s \quad (15c)$$

As observed from (14), expressions for  $I_{x'}$ ,  $I_{y'}$ , and  $I_{z'}$  are necessary to complete the derivation of the anisotropic effective permittivity. The result for  $I_{x'}$  is

$$I_{x'} = \int_0^{2\pi} d\phi \frac{-\epsilon_0}{\pi \epsilon_{gz'}} (I_\phi^s + I_\phi^d) \quad (16a)$$

$$I_\phi^s = -\frac{\alpha\gamma^2\sqrt{\alpha\gamma^2}}{2a^2} \left[ \frac{\sqrt{-\zeta}}{\vartheta_e} + \frac{\vartheta_e + \zeta}{\vartheta_e\sqrt{\vartheta_e}} \left( \frac{\pi}{2} - \tan^{-1} \frac{\sqrt{-\zeta}}{\sqrt{\vartheta_e}} \right) \right] \quad (16b)$$

$$I_\phi^d = \frac{\alpha\gamma^2}{2a^2} \left[ \frac{1 + a\nu_{gz'}^2}{\vartheta_o} + \frac{\vartheta_o(a+2) - (b + a\nu_{gz'}^2)}{\vartheta_o\sqrt{\vartheta_o}} \left( \frac{\pi}{2} - \tan^{-1} \frac{1}{\sqrt{\vartheta_o}} \right) \right] \quad (16c)$$

$$\nu_{gz'}^2 = k_{g\rho}^2 \ell_{z'}^2, \quad k_{g\rho}^2 = \omega^2 \mu_0 \epsilon_{g\rho}, \quad \zeta = \alpha\gamma^2 \nu_{gz'}^2 \quad (16d)$$

$$b = \frac{\alpha\gamma^2 + \zeta}{a}, \quad \vartheta_o = b - 1, \quad \vartheta_e = b + \zeta \quad (16e)$$

For  $I_{x'}$ , the result is expressed as follows

$$I_{x'} = \int_0^{2\pi} d\phi \frac{k_0^2}{\pi} (\ell_{y'}^2 \gamma_y^4 \sin^2 \phi I_\phi^o + \ell_{z'}^2 \gamma_z^4 \cos^2 \phi I_\phi^e) \quad (17a)$$

$$I_\phi^e = \alpha \left[ (I_1^e - I_2^e - I_3^e) + \frac{1}{\zeta} (I_s + I_d - \frac{1}{2}) \right] \quad (17b)$$

$$I_\phi^o = I_1^o - I_2^o - I_3^o \quad (17c)$$

$$I_1^e = \frac{\alpha\gamma^2\sqrt{\alpha\gamma^2}}{2a^2\vartheta_e} \left[ -\frac{\sqrt{-\zeta}}{b} + \frac{1}{\sqrt{\vartheta_e}} \left( \frac{\pi}{2} - \tan^{-1} \frac{\sqrt{-\zeta}}{\sqrt{\vartheta_e}} \right) \right] \quad (17d)$$

$$I_2^e = \frac{1}{2a\vartheta_o} \left[ 1 - \frac{1}{\sqrt{\vartheta_o}} \left( \frac{\pi}{2} - \tan^{-1} \frac{1}{\sqrt{\vartheta_o}} \right) \right] \quad (17e)$$

$$I_3^e = \frac{\alpha\gamma^2}{2a^2\vartheta_o} \left[ -\frac{1}{b} + \frac{1}{\sqrt{\vartheta_o}} \left( \frac{\pi}{2} - \tan^{-1} \frac{1}{\sqrt{\vartheta_o}} \right) \right] \quad (17f)$$

$$I_1^o = I_1^e|_{\alpha=1}, \quad I_2^o = I_2^e|_{\alpha=1}, \quad I_3^o = I_3^e|_{\alpha=1} \quad (17g)$$

From the symmetry,  $I_{y'}(\ell_{x'}, \ell_{y'}, \ell_{z'}) = I_{x'}(\ell_{y'}, \ell_{x'}, \ell_{z'})$ . Explicitly, the result for  $I_{y'}$  is

$$I_{y'} = \int_0^{2\pi} d\phi \frac{k_0^2}{\pi} (\ell_{x'}^2 \gamma_x^4 \cos^2 \phi I_\phi^o + \ell_{y'}^2 \gamma_y^4 \sin^2 \phi I_\phi^e) \quad (18)$$

Substituting  $\bar{\epsilon}_g$ ,  $\langle \bar{S} \rangle$ , and  $\bar{\xi}_{eff}$  in (2) yields the uniaxial effective permittivity tensor  $\bar{\epsilon}_{eff}$  whose lateral and vertical elements are, respectively

$$\epsilon_{eff\rho} = \epsilon_{g\rho} + \epsilon_0 \xi_{eff\rho} / (1 - S_\rho \xi_{eff\rho}) \quad (19a)$$

$$\epsilon_{effz} = \epsilon_{gz} + \epsilon_0 \xi_{effz} / (1 - S_z \xi_{effz}) \quad (19b)$$

As seen from the above expressions, effective permittivity  $\bar{\epsilon}_{eff}$  is anisotropic with optic axis in the vertical direction. In the next section, the anisotropic effective permittivity is used in the derivation of the polarimetric backscattering coefficients under the distorted Born approximation with dyadic Green's function (DGF) for the layer configuration.

### 3. SCATTERING COEFFICIENTS

Consider the scattering configuration in Figure 1. Region 0 is the upper half-space with permittivity  $\epsilon_0$ . Region 1 of thickness  $d_1$  is an isotropic medium consisted of randomly oriented spheroidal scatterers of permittivity  $\epsilon_{s1}$  in a background medium of permittivity  $\epsilon_{b1}$ . Region 2 of thickness  $d_2$  is an anisotropic medium composed of ellipsoidal scatterers of permittivity  $\epsilon_{s2}$  embedded in a host medium of permittivity  $\epsilon_{b2}$ . The ellipsoids are oriented preferentially in the vertical direction and randomly in azimuthal directions as described in the last section. Region 3 is the underlying homogeneous half-space of permittivity  $\epsilon_3$ . The effective permittivities of the scattering regions are calculated as shown in the last section. The distorted Born approximation is applied to derive the complete set of polarimetric backscattering coefficients constituting the covariance matrix and the Mueller matrix characterizing the polarimetric scattering properties of the layer media.

Polarimetric backscattering coefficients have been defined with ensemble averages of scattered fields [2]. The averages are calculated with spatial integrations over products of

the DGFs, the mean fields, and the correlation functions as follows

$$\begin{aligned}
\langle \bar{E}_{0s}(\bar{r}) \cdot \bar{E}_{0s}^*(\bar{r}) \rangle &= \sum_{i,j,k,l,m}^{x,y,z} k_0^4 \int_0^\pi d\psi_f \int_0^{2\pi} d\phi_f p_1(\psi_f, \phi_f) \\
&\cdot \int_{V_1} d\bar{r}_1 \int_{V_1} d\bar{r}_1^\circ C_{\xi 1 j k l m}(\bar{r}_1, \bar{r}_1^\circ; \psi_f, \phi_f) \\
&\cdot [\langle G_{01ij}(\bar{r}, \bar{r}_1) \rangle \langle F_{1k}(\bar{r}_1) \rangle] \cdot [\langle G_{01il}(\bar{r}, \bar{r}_1^\circ) \rangle \langle F_{1m}(\bar{r}_1^\circ) \rangle]^* \\
&+ \sum_{i,j,k,l,m}^{x,y,z} k_0^4 \int_0^{2\pi} d\phi_f p_2(\phi_f) \int_{V_2} d\bar{r}_2 \int_{V_2} d\bar{r}_2^\circ C_{\xi 2 j k l m}(\bar{r}_2, \bar{r}_2^\circ; \phi_f) \\
&\cdot [\langle G_{02ij}(\bar{r}, \bar{r}_2) \rangle \langle F_{2k}(\bar{r}_2) \rangle] \cdot [\langle G_{02il}(\bar{r}, \bar{r}_2^\circ) \rangle \langle F_{2m}(\bar{r}_2^\circ) \rangle]^* \quad (20)
\end{aligned}$$

where  $V_1$  is the volume occupied by Region 1 and  $V_2$  by Region 2. The DGFs and the mean fields have been obtained in [2]; the correlation functions need to be specified next. The integrations are then effectuated to derive the scattering coefficients.

For Region 1, the correlation functions  $C$ 's in (20) are defined in [16] for the spheroids. In Region 2, the correlation functions in the global spatial domain are

$$C_{\xi 2 j k l m}(\bar{r}_2, \bar{r}_2^\circ, \phi_f) = \langle \xi_{2jk}(\bar{r}_2) \xi_{2lm}^*(\bar{r}_2^\circ) | \phi_f(\bar{r}_2) \rangle \quad (21)$$

To facilitate the integration of (20), Fourier transforms of the correlation functions are introduced for the statistically homogeneous scattering media under consideration

$$C_{\xi 2 j k l m}(\bar{r}_2, \bar{r}_2^\circ, \phi_f) = \int_{-\infty}^{\infty} d\bar{\beta} \Phi_{2jk}(\bar{\beta}) e^{-i\bar{\beta} \cdot (\bar{r}_2 - \bar{r}_2^\circ)} \quad (22)$$

which is expressed in the global coordinate system  $(\hat{x}, \hat{y}, \hat{z})$  and related by the Eulerian rotation transformation  $\bar{T}$  (1) to the following non-zero correlations in the local coordinate system  $(\hat{x}', \hat{y}', \hat{z}')$

$$\Phi_{2x'x'}(\bar{\beta}') = \Phi_{2x'x'x'x'}(\bar{\beta}') = \delta_{2x'x'} \Phi_{\xi 2}(\bar{\beta}') \quad (23a)$$

$$\Phi_{2x'y'}(\bar{\beta}') = \Phi_{2x'y'y'}(\bar{\beta}') = \delta_{2x'y'} \Phi_{\xi 2}(\bar{\beta}') \quad (23b)$$

$$\Phi_{2x'z'}(\bar{\beta}') = \Phi_{2x'z'z'}(\bar{\beta}') = \delta_{2x'z'} \Phi_{\xi 2}(\bar{\beta}') \quad (23c)$$

$$\Phi_{2y'x'}(\bar{\beta}') = \Phi_{2y'x'x'}(\bar{\beta}') = \delta_{2y'x'} \Phi_{\xi 2}(\bar{\beta}') \quad (23d)$$

$$\Phi_{2y'y'}(\bar{\beta}') = \Phi_{2y'y'y'}(\bar{\beta}') = \delta_{2y'y'} \Phi_{\xi 2}(\bar{\beta}') \quad (23e)$$

$$\Phi_{2y'z'}(\bar{\beta}') = \Phi_{2y'z'z'}(\bar{\beta}') = \delta_{2y'z'} \Phi_{\xi 2}(\bar{\beta}') \quad (23f)$$

$$\Phi_{2z'x'}(\bar{\beta}') = \Phi_{2z'x'x'}(\bar{\beta}') = \delta_{2z'x'} \Phi_{\xi 2}(\bar{\beta}') \quad (23g)$$

$$\Phi_{2z'y'}(\bar{\beta}') = \Phi_{2z'y'y'}(\bar{\beta}') = \delta_{2z'y'} \Phi_{\xi 2}(\bar{\beta}') \quad (23h)$$

$$\Phi_{2z'z'}(\bar{\beta}') = \Phi_{2z'z'z'z'}(\bar{\beta}') = \delta_{2z'z'} \Phi_{\xi 2}(\bar{\beta}') \quad (23i)$$

where  $\Phi_{\xi 2}(\bar{\beta}')$  is given in (5b), which is the Fourier transform of (5a), and the variance  $\delta_2$ 's in (23) are

$$\delta_{2x'x'} = \left| \frac{\epsilon_{b2} - \epsilon_{g2\rho}}{\epsilon_0 + S_{2x'}(\epsilon_{b2} - \epsilon_{g2\rho})} \right|^2 (1 - f_{s2}) + \left| \frac{\epsilon_{s2} - \epsilon_{g2\rho}}{\epsilon_0 + S_{2x'}(\epsilon_{s2} - \epsilon_{g2\rho})} \right|^2 f_{s2} \quad (24a)$$

$$\delta_{2y'y'} = \left| \frac{\epsilon_{b2} - \epsilon_{g2\rho}}{\epsilon_0 + S_{2y'}(\epsilon_{b2} - \epsilon_{g2\rho})} \right|^2 (1 - f_{s2}) + \left| \frac{\epsilon_{s2} - \epsilon_{g2\rho}}{\epsilon_0 + S_{2y'}(\epsilon_{s2} - \epsilon_{g2\rho})} \right|^2 f_{s2} \quad (24b)$$

$$\delta_{2z'z'} = \left| \frac{\epsilon_{b2} - \epsilon_{g2z}}{\epsilon_0 + S_{2z'}(\epsilon_{b2} - \epsilon_{g2z})} \right|^2 (1 - f_{s2}) + \left| \frac{\epsilon_{s2} - \epsilon_{g2z}}{\epsilon_0 + S_{2z'}(\epsilon_{s2} - \epsilon_{g2z})} \right|^2 f_{s2} \quad (24c)$$

$$\begin{aligned} \delta_{2x'y'} &= \left[ \frac{\epsilon_{b2} - \epsilon_{g2\rho}}{\epsilon_0 + S_{2x'}(\epsilon_{b2} - \epsilon_{g2\rho})} \right] \left[ \frac{\epsilon_{b2} - \epsilon_{g2\rho}}{\epsilon_0 + S_{2y'}(\epsilon_{b2} - \epsilon_{g2\rho})} \right]^* (1 - f_{s2}) \\ &+ \left[ \frac{\epsilon_{s2} - \epsilon_{g2\rho}}{\epsilon_0 + S_{2x'}(\epsilon_{s2} - \epsilon_{g2\rho})} \right] \left[ \frac{\epsilon_{s2} - \epsilon_{g2\rho}}{\epsilon_0 + S_{2y'}(\epsilon_{s2} - \epsilon_{g2\rho})} \right]^* f_{s2} = \delta_{2y'x'}^* \end{aligned} \quad (24d)$$

$$\begin{aligned} \delta_{2x'z'} &= \left[ \frac{\epsilon_{b2} - \epsilon_{g2\rho}}{\epsilon_0 + S_{2x'}(\epsilon_{b2} - \epsilon_{g2\rho})} \right] \left[ \frac{\epsilon_{b2} - \epsilon_{g2z}}{\epsilon_0 + S_{2z'}(\epsilon_{b2} - \epsilon_{g2z})} \right]^* (1 - f_{s2}) \\ &+ \left[ \frac{\epsilon_{s2} - \epsilon_{g2\rho}}{\epsilon_0 + S_{2x'}(\epsilon_{s2} - \epsilon_{g2\rho})} \right] \left[ \frac{\epsilon_{s2} - \epsilon_{g2z}}{\epsilon_0 + S_{2z'}(\epsilon_{s2} - \epsilon_{g2z})} \right]^* f_{s2} = \delta_{2z'x'}^* \end{aligned} \quad (24e)$$

$$\begin{aligned} \delta_{2y'z'} &= \left[ \frac{\epsilon_{b2} - \epsilon_{g2\rho}}{\epsilon_0 + S_{2y'}(\epsilon_{b2} - \epsilon_{g2\rho})} \right] \left[ \frac{\epsilon_{b2} - \epsilon_{g2z}}{\epsilon_0 + S_{2z'}(\epsilon_{b2} - \epsilon_{g2z})} \right]^* (1 - f_{s2}) \\ &+ \left[ \frac{\epsilon_{s2} - \epsilon_{g2\rho}}{\epsilon_0 + S_{2y'}(\epsilon_{s2} - \epsilon_{g2\rho})} \right] \left[ \frac{\epsilon_{s2} - \epsilon_{g2z}}{\epsilon_0 + S_{2z'}(\epsilon_{s2} - \epsilon_{g2z})} \right]^* f_{s2} = \delta_{2z'y'}^* \end{aligned} \quad (24f)$$

Based on the invariant property of the Fourier transform under the rotation transformation, spectral density  $\Phi_{2jklm}(\bar{\beta})$  in the global coordinates can functionally be related to those given in (24) with

$$\begin{aligned} \Phi_{\xi 2}(\bar{\beta}) &= \Phi_{\xi 2}(\beta'_x = \beta_x \cos \phi_f + \beta_y \sin \phi_f, \\ &\quad \beta'_y = -\beta_x \sin \phi_f + \beta_y \cos \phi_f, \\ &\quad \beta'_z = \beta_z) \end{aligned} \quad (25)$$

In the global coordinates, the rotation transformation together with the above invariant property cast the anisotropic spectral densities into the form

$$\Phi_{2jklm}(\bar{\beta}) = \delta_{2jklm} \Phi_{\xi 2}(\bar{\beta}) \quad (26)$$

where variance  $\delta_{2jklm}$  are dependent on the Eulerian angle  $\phi_f$  as

$$\begin{aligned}\delta_{2jklm} = & (\delta_{2x'x'}T_{xxjk} + \delta_{2y'y'}T_{yyjk} + \delta_{2z'z'}T_{zzjk})T_{xxlm} \\ & + (\delta_{2x'y'}T_{xxjk} + \delta_{2y'y'}T_{yyjk} + \delta_{2z'y'}T_{zzjk})T_{yylm} \\ & + (\delta_{2x'z'}T_{xxjk} + \delta_{2y'z'}T_{yyjk} + \delta_{2z'z'}T_{zzjk})T_{zzlm}\end{aligned}\quad (27)$$

The Eulerian rotation has been applied to arrived at (27) where  $T$ 's are elements of the following transforming tensors

$$\bar{\bar{T}}_{xx} = \begin{bmatrix} \cos^2 \phi_f & \sin \phi_f \cos \phi_f & 0 \\ \sin \phi_f \cos \phi_f & \sin^2 \phi_f & 0 \\ 0 & 0 & 0 \end{bmatrix} \quad (28a)$$

$$\bar{\bar{T}}_{yy} = \begin{bmatrix} \sin^2 \phi_f & -\sin \phi_f \cos \phi_f & 0 \\ -\sin \phi_f \cos \phi_f & \cos^2 \phi_f & 0 \\ 0 & 0 & 0 \end{bmatrix} \quad (28b)$$

$$\bar{\bar{T}}_{zz} = \bar{\bar{I}} - \bar{\bar{T}}_{xx} - \bar{\bar{T}}_{yy} = \begin{bmatrix} 0 & 0 & 0 \\ 0 & 0 & 0 \\ 0 & 0 & 1 \end{bmatrix} \quad (28c)$$

By substituting the above correlation functions, the dyadic Green's functions of the layer medium, and the mean fields into (20), the correlations of the scattered field can now be found. Rearranging all the coefficients from the DGF and mean fields, the scattering coefficients can be written as

$$\begin{aligned}\sigma_{\mu\tau\nu\kappa} = & \pi k_0^4 \int_0^\pi d\psi_f \int_0^{2\pi} d\phi_f p_1(\psi_f, \phi_f) \sum_{a,b,c,d}^{-1,1} \sum_{j,k,l,m}^{x,y,z} \Psi_{1\mu\tau,jk}^{ab} \Psi_{1\nu\kappa,lm}^{cd*} \mathcal{I}_{1jklm}^{abcd} \\ & + \pi k_0^4 \int_0^{2\pi} d\phi_f p_2(\phi_f) \sum_{p,q,r,s}^{ou,od} \sum_{j,k,l,m}^{eu,ed} \sum_{j,k,l,m}^{x,y,z} \Psi_{2\mu\tau,jk}^{pq} \Psi_{2\nu\kappa,lm}^{rs*} \mathcal{I}_{2jklm}^{pqrs}\end{aligned}\quad (29)$$

The scattering contribution of the first term in (29) from Region 1 due to the spheroids has been obtained in [16] and the solution consists of 16 terms for downgoing and upgoing incident and scattered waves. Region 2 contains scatterers with preferential vertical alignment, which effectively renders the medium anisotropic. The ordinary and extraordinary waves going down and up give rise to 216 terms in the second term of (29). All coefficient  $\Psi_2$ 's have been derived and given in [2]. For  $\mathcal{I}_{2jklm}^{pqrs}$ , the result is

$$\begin{aligned}\mathcal{I}_{2jklm}^{pqrs} = & i \frac{2\delta_{2jklm} \ell_{2x'} \ell_{2y'} \ell_{2z'}}{\pi \ell_{2x'}^4} \left[ \frac{e^{-i(\kappa_{pq} - \kappa_{rs})d_2}}{(\kappa_{pq} - \kappa_2)^2 (\kappa_{pq} - \kappa_2^*)^2 (\kappa_{pq} - \kappa_{rs})} \right. \\ & \left. + \frac{e^{i(\kappa_{rs} - \kappa_{pq})d_1}}{(\kappa_{rs} - \kappa_2)^2 (\kappa_{rs} - \kappa_2^*)^2 (\kappa_{rs} - \kappa_{pq})} - \mathcal{P}_2(\kappa_2) - \mathcal{Q}_2(\kappa_2^*) \right]\end{aligned}\quad (30a)$$

where  $\mathcal{P}_2(\kappa_2)$  and  $\mathcal{Q}_2(\kappa_2^*)$ , resulted from complex integrations, are determined by, respectively,

$$\begin{aligned} \mathcal{P}_2(\kappa_2) = & \frac{i(d_2 - d_1)e^{-i(\kappa_2 - \kappa_{rs})d_1}e^{i(\kappa_2 - \kappa_{pq})d_2}}{(2i\text{Im } \kappa_2)^2(\kappa_2 - \kappa_{pq})(\kappa_2 - \kappa_{rs})} \\ & + \left[ \frac{e^{-i(\kappa_{pq} - \kappa_{rs})d_1} + e^{-i(\kappa_{pq} - \kappa_{rs})d_2}}{(2i\text{Im } \kappa_2)^2(\kappa_2 - \kappa_{pq})(\kappa_2 - \kappa_{rs})} \right. \\ & \left. - \frac{e^{-i(\kappa_2 - \kappa_{rs})d_1}e^{i(\kappa_2 - \kappa_{pq})d_2}}{(2i\text{Im } \kappa_2)^2(\kappa_2 - \kappa_{pq})(\kappa_2 - \kappa_{rs})} \right] \\ & \cdot \left[ \frac{1}{i\text{Im } \kappa_2} + \frac{1}{\kappa_2 - \kappa_{pq}} + \frac{1}{\kappa_2 - \kappa_{rs}} \right] \end{aligned} \quad (30b)$$

$$\begin{aligned} \mathcal{Q}_2(\kappa_2^*) = & \frac{i(d_2 - d_1)e^{i(\kappa_2^* - \kappa_{pq})d_1}e^{-i(\kappa_2^* - \kappa_{rs})d_2}}{(2i\text{Im } \kappa_2^*)^2(\kappa_2^* - \kappa_{pq})(\kappa_2^* - \kappa_{rs})} \\ & + \frac{e^{i(\kappa_2^* - \kappa_{pq})d_1}e^{-i(\kappa_2^* - \kappa_{rs})d_2}}{(2i\text{Im } \kappa_2^*)^2(\kappa_2^* - \kappa_{pq})(\kappa_2^* - \kappa_{rs})} \\ & \cdot \left[ \frac{1}{i\text{Im } \kappa_2^*} + \frac{1}{\kappa_2^* - \kappa_{pq}} + \frac{1}{\kappa_2^* - \kappa_{rs}} \right] \end{aligned} \quad (30c)$$

In (30), the pole  $\kappa_2$  is computed with the following equations

$$\kappa_2 = i\ell_{2z'}^{-1} \sqrt{1 + k_{\phi x}^2 \ell_{2x'}^2 + k_{\phi y}^2 \ell_{2y'}^2} \quad (31a)$$

$$k_{\phi x} = k_{\rho i} \cos(\phi_i - \phi_f) - k_{\rho s} \cos(\phi_s - \phi_f) \quad (31b)$$

$$k_{\phi y} = k_{\rho i} \sin(\phi_i - \phi_f) - k_{\rho s} \sin(\phi_s - \phi_f) \quad (31c)$$

where  $\phi_i$  and  $\phi_s$  are azimuthal angles of incident and scattered waves, respectively. The remaining integrations over Eulerian angles in (29) can be carried out numerically. When low-frequency condition is valid, the integrations can be done analytically. It should be noted that (29) expresses the scattering coefficients in the scattered basis which can be transformed to the incident basis by changing the sign of  $\sigma_{h\tau\theta\kappa}$  and  $\sigma_{v\tau h\kappa}$  [2]. The scattering effect of the rough boundaries at the medium interfaces can also be estimated by incoherently adding the total contribution from the rough surface scattering with consideration of the propagation loss in the calculations of scattering coefficients. Compared with the model in [2] for the case of vertically oriented spheroids, the new model can give higher co-polarized backscattering coefficients due to higher total cross section of the ellipsoids for the same fractional volume. Another difference is that the new model provides non-zero cross-polarized backscattering in the first-order distorted Born term whereas the former



can only account for the cross-polarized return in the second or higher order term when the spheroids are vertically oriented.

## 4. RESULTS AND DISCUSSION

### a. Data Comparisons

In this subsection, theoretical results are compared with experimental measurements for backscattering coefficients at 9 GHz as a function of incident angle. The radar backscatter data were collected for the thick first-year sea ice near Point Barrow, Alaska [86]. For thick first-year sea ice with bare surface, the scattering configuration is illustrated in Figure 4 representing a sea ice layer over sea water. The ice layer was 1.65-m thick and contained brine inclusions. From ground-truth data, it has been inferred [19] that the brine had a permittivity of  $\epsilon_{s1} = (38.0 + 41.0)\epsilon_0$  and occupied a fractional volume of  $f_{s1} = 4.5\%$ . The background ice permittivity was estimated to be  $\epsilon_{b1} = (3.15 + i0.002)\epsilon_0$  and the permittivity of sea water  $\epsilon_2 = (45.0 + i40.0)\epsilon_0$ . With correlation length  $\ell_{1x'} = 0.70$  mm,  $\ell_{1z'} = 0.25$  mm, and  $\ell_{1x''} = 1.20$  mm, the theoretical results match well with the experimental data, as shown in Figure 5, for co-polarized backscattering coefficient  $\sigma_{hh}$  and  $\sigma_{vv}$  at large incident angles, and cross-polarized backscattering coefficient  $\sigma_{vh}$  over the range of incident angles.

The disagreement in the co-polarized backscattering coefficients at small incident angles is due to the scattering from rough surface. In the configuration of Figure 5, the interfaces have been assumed to be smooth and the rough surface scattering has been ignored. The effect of the roughness at the lower interface of the thick first-year sea ice is negligible since the wave at 14 GHz is attenuated before the sea water is reached. To account for the rough surface effect at the top interface, a Gaussian roughness is now considered with standard deviation  $\sigma_s = 0.6$  mm and correlation length  $\ell_s = 1.5$  cm as depicted in Figure 6, where all other physical parameters are the same as in Figure 4. The rough surface contribution, calculated with the small perturbation method (SPM) [1], is incoherently added to the volume scattering. The comparison between theoretical and experimental results for the co-polarized returns is improved at the low incident angles as seen in Figure 7. For this surface, the additional contribution to the cross-polarized return is small and is actually ignored in the SPM model applied in this case. The cross-polarized return therefore remains unchanged.

The configuration for snow-covered sea ice is shown in Figure 8. The snow is 10-cm thick according to the average of the thickness range reported in [18]. In the snow layer, the oblate spheroidal shape is assumed for the ice grains with correlation lengths  $\ell_p = \ell_z/6 = 0.15$  mm. The physical parameters for the sea ice layer and the sea water are kept unchanged. Both the top and the middle interfaces are rough with standard deviation  $\sigma_s = 0.1$  cm and correlation length  $\ell_s = 1.5$  cm. The theoretical result compare

well with the measurements from the sea ice layer with snow cover as seen in Figure 9 for the conventional backscattering coefficients. The theoretical cross-polarized returns are, however, lower than the measurements. For a medium with high fractional volume such as snow, a significant part of the total contribution to  $\sigma_{hv}$  can come from higher order scattering which is ignored in the present model. Regarding the scattering mechanisms, volume scattering is dominant at large incident angles. Rough surface effect is still strong at small incident angles with more contribution from the snow-ice interface due to the larger permittivity contrast. The oscillations observed in the curves in Figure 9 are caused by the boundary effect of the snow cover. Comparing the cases with and without snow cover shows that the low-loss dry-snow layer can enhance the backscattering due to the introduction of more scatterers (ice grains) and a better impedance match between the air and the sea ice layer.

The above results have shown that the scattering from the inhomogeneities is dominant at large incident angles while the contribution from the rough surface is important at small incident angles for co-polarized returns. The cross-polarized return due to the inclusions comes from the first-order term under the distorted Born approximation in this model. The spheroidal model in [2] predicts a zero value of cross-polarized backscattering coefficient  $\sigma_{vh}$  under the first-order approximation because the scatterers are vertically aligned. In the next subsections, effects of correlation lengths and polarization signature of sea ice are considered.

#### b. Study on Correlation Lengths

SHAPE	$\ell_x'$	$\ell_y'$	$\ell_z'$	$\ell_x'/\ell_y'$	$\ell_x'/\ell_z'$	$\ell_y'/\ell_z'$	$\ell_x'\ell_y'\ell_z'$
Reference	0.700	0.250	1.200	2.800	1.714	4.800	0.210
Expanded	1.050	0.375	1.800	2.800	1.714	4.800	0.709
Contracted	0.467	0.167	0.800	2.800	1.714	4.800	0.062
Thickened	0.467	0.375	1.200	1.245	2.570	3.200	0.210
Thinned	1.050	0.167	1.200	6.287	1.143	7.186	0.210
Elongated	0.572	0.204	1.800	2.800	3.147	8.824	0.210
Shortened	0.857	0.306	0.800	2.800	0.933	2.614	0.210

**Table 1.** Correlation lengths for various scatterer shapes

The geometry of the brine inclusions in sea ice is not available from the ice characterization data. To study the effect of the scatterer size and shape, scattering coefficients are calculated with variable correlation lengths. To isolate the effect of correlation lengths, bare sea ice with smooth surface configuration in Figure 4 is considered to avoid the contri-

bution from the snow layer and rough interfaces. The correlation lengths used in the data matching serve as a reference. The scatterer is expanded, contracted, thickened, thinned, elongated, and shortened by varying the correlation lengths as shown in Table 1 while the fractional volume is kept constant in all cases.

When all the correlation lengths are varied by the same factor, the scatterer shape remains unchanged since the correlation length ratios stay the same. For the same fractional volume, the effective number of scatterers decreases as the scatterer is expanded and increases when the scatterer is contracted. The conventional backscattering coefficients as well as the correlation coefficient  $\rho = \sigma_{hhvv} / \sqrt{\sigma_{hh}\sigma_{vv}}$  [2] between the horizontal and vertical returns are calculated for the volume expansion and contraction with the same factor of 1.5<sup>3</sup>. The results are plotted in Figure 10. For  $\sigma_{hh}$  and  $\sigma_{vv}$ , the scattering coefficients are reduced much more when the correlation volume of the scatterer is contracted as compared to the increases in the case of volume expansion. This shows the nonlinear relation between the volume scattering and the scatterer size. In this case, an underestimate in the scatterer volume, compared to the overestimate with the same factor, will lead to more variation in the co-polarized backscattering coefficients. An interesting observation is the insensitivity of the cross-polarized ratio  $e = \sigma_{hv} / \sigma_{hh}$  as shown in Figure 10. This is because the depolarization is caused by the non-spherical shape of the scatterer, which is kept unchanged. For the correlation coefficient  $\rho$ , the results show that the horizontal and vertical waves become more correlated as the correlation volume increases. For the larger volume, the sea ice medium is more lossy and wave path is effectively reduced. Consequently, the anisotropic effect causing the decorrelation between the horizontal and vertical waves is weakened.

When the correlation length ratios are varied while the scatterer volume and the fractional volume are kept, the scatterer shape is deformed and the number of scatterers remains unchanged. For the same vertical correlation length  $\ell_z$ , the horizontal correlation lengths are now modified by a factor of 1.5 to thicken and thin the scatterer as indicated in Table 1. In Figure 11, the co-polarized returns are rather insensitive since the horizontal cross section of the scatterer is not varied ( $\ell_x \ell_z = 0.175 \text{ mm}^2$ ). It is obvious that the cross-polarized ratio is strongly dependent on the scatterer shape. The depolarization effect is more prominent as the scatterer is further deformed from the spheroidal shape. For the magnitude of  $\rho$ , the variation is larger at small incident angles where the scatterer shapes are more different as compared to the cases at large incident angles. The phase of  $\rho$  started from 0° at normal due to the azimuthal symmetry [20] and increases with incident angles. Also, the absolute value of the phase is larger for the thicker scatterer since the anisotropy is stronger.

While the correlation length ratio  $\ell_x / \ell_y$  and the fractional volume are not changed, the scatterer is elongated and shortened by varying the vertical correlation length  $\ell_z$  by a factor of 1.5. Figure 12 presents the results for these cases compared with the reference.

There are large changes in the co-polarized returns due to the corresponding differences in the horizontal cross section of the scatterer. The variation in the cross-polarized ratio is small since the horizontal correlation length ratio is not varied. The magnitude of  $\rho$  differs more at large incident angle where the shape difference is more significant. The phase of  $\rho$  is closer to zero as the scatterer becomes shorter and the sea ice medium approaches the isotropic condition. As shown in this subsection, the scatterer volume and the horizontal cross section affect the level of the co-polarized returns. The depolarization effect characterized by the cross-polarized ratio is controlled by the scatterer shape. The ellipsoidal shape of the scatterer with preferential vertical alignment is also responsible for the anisotropy of the medium and consequently the behavior of the complex correlation coefficient  $\rho$  between the horizontal and vertical returns.

### c. Polarimetric Simulation

To investigate how polarization signatures relate to the corresponding covariance matrix and convey information regarding different sea ice configurations and scattering mechanisms, polarimetric data are simulated for sea ice with bare surface and with snow cover at different incident angles. The configurations under consideration are in Figure 4 for bare sea ice with smooth surface, in Figure 6 for bare sea ice with rough surface, and in Figure 8 for snow-covered sea ice. Due to the azimuthal symmetry of the scattering configuration, the covariance matrix has the form of [20]

$$\overline{\overline{C}} = \sigma_{hh} \begin{bmatrix} 1 & 0 & \rho\sqrt{\gamma} \\ 0 & e & 0 \\ \rho^*\sqrt{\gamma} & 0 & \gamma \end{bmatrix} \quad (32)$$

where the co-polarized ratio is  $\gamma = \sigma_{vv}/\sigma_{hh}$ . The elements of the covariance matrix is used to calculate the Mueller matrix to obtain the signature  $\sigma(\alpha_r, \beta_r, \alpha_i, \beta_i)$  as defined in [2] for polarization angles  $\alpha_r$  and  $\alpha_i$  and ellipticity angles  $\beta_r$  and  $\beta_i$  of the received ( $r$ ) and the incident ( $i$ ) waves, respectively. For a co-polarized signature,  $\alpha_r = \alpha_i = \alpha$  and  $\beta_r = \beta_i = \beta$ .

Normalized co-polarized signatures denoted by  $\sigma_n$  for bare sea ice with smooth and rough surfaces at incident angles of  $20^\circ$  and  $45^\circ$  are presented in Figure 13. At  $\theta_{0i} = 20^\circ$ , the signatures for smooth sea ice due to volume scattering and for rough sea ice due to surface scattering are similar because both covariance matrices have  $\gamma$  close to unity, small  $e$ , and  $\rho$  with small phase as seen in Figure 14. However, the magnitude of  $\rho$  shown in Figure 14 are distinctively smaller for the volume scattering mechanism with smooth surface. At  $\theta_{0i} = 45^\circ$ , the volume scattering is dominant in both smooth and rough cases whose correlation coefficients have larger phase giving rise to the signatures in Figures 13c and 13d with more distortion compared to those at  $20^\circ$ . For snow-covered sea ice, Figure

15 reveal that  $|\rho|$  is closer to unity and the phase is smaller at incident angles of  $20^\circ$  and  $45^\circ$ . Thus, the corresponding signatures for the snow-cover sea ice in Figure 15 have much less distortion due to the effects of the rough surfaces and the isotropic snow layer which mask the anisotropic information from the lower sea ice layer at the X-band frequency. The boundary effects due to snow cover can also be observed with the oscillation in the phase of  $\rho$  in Figure 14.

## 5. SUMMARY

In this paper, an anisotropic layer model with ellipsoidal scatterers have been developed. The top layer is an isotropic medium with randomly oriented spheroids. In the anisotropic layer, the ellipsoids are aligned vertically and oriented randomly in azimuthal directions. Further medium complexity such as multi-species, size and shape distributions have not been incorporated in this model and can be considered for future model development. The effective permittivities are derived with the extended strong fluctuation theory and the polarimetric scattering coefficients are calculated under the distorted Born approximation. In this model, the cross-polarized return is obtained from the first-order distorted Born approximation due to non-spherical shapes of the scatterers; however, higher order contributions are ignored. The effects of rough surfaces are estimated with the incoherent addition method and higher-order interactions between volume and surface scattering mechanisms are not included. The theoretical results compare well with the measured data for thick first-year sea ice with bare surface and snow cover. The effects of the scatterer geometry are investigated by varying correlation lengths which change the shape and the volume of the scatterer. Polarization signatures are then simulated for the thick first-year with and without snow cover. The volume and surface scattering mechanisms are discussed in terms of conventional backscattering coefficients as well as polarization signatures and correlation coefficient  $\rho$  between the vertical and the horizontal returns.

## Acknowledgments

The research described in this paper was carried out by the Jet Propulsion Laboratory, California Institute of Technology, under a contract with the National Aeronautics and Space Administration; and by the Massachusetts Institute of Technology, under a contract with the Office of Naval Research (N00014-89-J-1107).

## REFERENCES

- [1] Tsang, L., J. A. Kong, and R. T. Shin, *Theory of Microwave Remote Sensing*, John Wiley & Sons, New-York, 1985.

- [2] Nghiem, S. V., M. Borgeaud, J. A. Kong, and R. T. Shin, Polarimetric remote sensing of geophysical media with layer random medium model, *Progress in Electromagnetics Research*, ed. by J. A. Kong. Volume 3: *Polarimetric Remote Sensing*, Chap. 1, pp. 1-73, Elsevier, New York, 1990.
- [3] Zuniga, M. A., T. M. Habashy, and J. A. Kong, "Active Remote Sensing of Layered Random Media," *IEEE Trans. Geosci. Electron.*, Vol. GE-17, No. 4, pp. 296-302, October 1979.
- [4] Lee, J. K., and J. A. Kong, "Active Microwave Remote Sensing of an Anisotropic Random Medium Layer," *IEEE Transactions on Geoscience and Remote Sensing*, Vol. GE-23, No. 6, pp. 910-923, November 1985.
- [5] Borgeaud, M., J. A. Kong, and F. C. Lin, "Microwave Remote Sensing of Snow-covered Sea Ice," *Proceeding of the IGARSS'86 Symposium*, Zürich, Switzerland, pp. 133-138, September 1986.
- [6] Borgeaud, M., R. T. Shin, and J. A. Kong, "Theoretical Models for Polarimetric Radar Clutter," *Journal of Electromagnetic Waves and Applications*, Vol. 1, No. 1, pp. 73-89, 1987.
- [7] Borgeaud, M., S. V. Nghiem, R. T. Shin, and J. A. Kong, "Theoretical Models for Polarimetric Microwave Remote Sensing of Earth Terrain," *Journal of Electromagnetic Waves and Applications*, Vol. 3, No. 1, pp. 61-81, 1989.
- [8] Zuniga, M. A., J. A. Kong, and L. Tsang, "Depolarization Effects in the Active Remote Sensing of Random Media," *Journal of Applied Physics*, Vol. 51, No. 5, pp. 2315-2325, May 1980.
- [9] de Wolf, D. A., "Electromagnetic Reflection from an Extended Turbulent Medium: Cumulative Forward-Scatter Single Backscatter Approximation," *IEEE Transactions on Antennas and Propagation*, Vol. AP-19, No. 2, pp. 254-262, March 1971.
- [10] Rosenbaum, S., and L. W. Bowles, "Clutter Return from Vegetated Areas," *IEEE Transactions on Antennas and Propagation*, Vol. AP-22, No. 2, pp. 227-236, March 1974.
- [11] Lang, R. H., "Electromagnetic Backscattering from a Sparse Distribution of Lossy Dielectric Scatterers," *Radio Science*, Vol. 16, No 1, pp. 15-30, 1981.
- [12] Tsang, L., and J. A. Kong, "Scattering of Electromagnetic Waves from Random Media with Strong Permittivity Fluctuations," *Radio Science*, Vol. 16, No. 3, pp. 303-320, May-June 1981.
- [13] Tsang, L., J. A. Kong, and R. W. Newton, "Application of Strong Fluctuation Random Medium Theory to Scattering of Electromagnetic Waves from a Half-space of Dielectric Mixture," *IEEE Transactions on Antennas and Propagation*, Vol. AP-30, No. 2, pp. 292-302, March 1982.
- [14] Tsang, L., and J. A. Kong, "Application of Strong Fluctuation Random Medium Theory to Scattering from Vegetation-Like Half Space," *IEEE Transactions on Geoscience*

and *Remote Sensing*, Vol. GE-19, No. 1, pp. 62-69, January 1981.

- [15] Lin, F. C., J. A. Kong, and R. T. Shin, "Theoretical Models for Active and Passive Microwave Remote Sensing of Snow-covered Sea Ice," *IGARSS'87*, University of Michigan, Ann Arbor, Michigan, May 1987.
- [16] Nghiem, S. V., T. Le Toan, J. A. Kong, H. C. Han, and M. Borgeaud, "Layer Model with Random Spheroidal Scatterers for Remote Sensing of Vegetation Canopy," *Journal of Electromagnetic Waves and Applications*, accepted for publication, 1992.
- [17] Yueh, H. A., R. T. Shin, and J. A. Kong, "Scattering from Randomly Oriented Scatterers with Strong Permittivity Fluctuations," *Journal of Electromagnetic Waves and Applications*, Vol. 4, No. 10, pp. 983-1004, 1990.
- [18] Kim, Y. S., R. K. Moore, and R. G. Onstott, "Theoretical and Experimental Study of Radar Backscatter from Sea Ice," *RSL Tech. Rep. 331-37*, Remote Sensing Lab., Center for Research, Inc., U. of Kansas, Lawrence, Kansas, 1984.
- [19] Lin, F. C., "Theoretical Models for Microwave Remote Sensing of Snow-covered Sea Ice," *Ph. D. Dissertation*, Department of Electrical Engineering and Computer Science, Massachusetts Institute of Technology, 1988.
- [20] Nghiem, S. V., S. H. Yueh, R. Kwok, and F. K. Li, "Symmetry Properties in Polarimetric Remote Sensing," in press, *Radio Science*, 1992.

### Figure Captions

**Figure 1.** Scattering configuration of layer media.

**Figure 2.** Illustration of a sea-ice horizontal thin section; the arrows represent random horizontal orientations of crystallographic c-axes and ellipsoidal brine inclusions.

**Figure 3.** Geometry of an ellipsoidal scatterer.

**Figure 4.** Scattering configuration of bare thick first-year sea ice with smooth surface.

**Figure 5.** Backscattering coefficients from bare thick first-year sea ice with smooth surface.

**Figure 6.** Scattering configuration of bare thick first-year sea ice with rough surface.

**Figure 7.** Backscattering coefficients from bare thick first-year sea ice with rough surface.

**Figure 8.** Scattering configuration of thick first-year sea ice with snow cover.

**Figure 9.** Backscattering coefficients from thick first-year sea ice with snow cover.

**Figure 10.** Effects of expanded and contracted scatterer volumes.

**Figure 11.** Effects of thickened and thinned scatterer shapes.

**Figure 12.** Effects of elongated and shortened scatterer shapes.

**Figure 13.** Polarization signatures of bare thick first-year sea ice with smooth and rough surfaces at incident angles of  $20^\circ$  and  $45^\circ$ .

**Figure 14.** Correlation coefficient  $\rho$  of thick first-year sea ice with bare smooth surface, bare rough surface, and snow cover.

**Figure 15.** Polarization signatures of thick first-year sea ice with snow cover at incident angles of  $20^\circ$  and  $45^\circ$ .



## EFFECTIVE PERMITTIVITY OF SALINE ICE UNDER THERMAL VARIATION

S. V. Nghiem and R. Kwok  
Jet Propulsion Laboratory  
California Institute of Technology  
Pasadena, California 91109

J. A. Kong and R. T. Shin  
Department of Electrical Engineering and Computer Science  
and Research Laboratory of Electronics  
Massachusetts Institute of Technology  
Cambridge, Massachusetts 02139

A. J. Gow and S. A. Arcone  
U.S. Army Cold Regions Research and Engineering Laboratory  
Hanover, New Hampshire 03755

### ABSTRACT

A model to calculate the effective permittivity of saline ice under thermal variation is presented in this paper. The model includes multi-phase inhomogeneities with multiple species characterized by orientation, size, and shape distributions. The model is then used to derive the effective permittivity as a function of temperature under the strong fluctuation theory which is extended to account for the complexity. The results calculated from the model are compared with experimental data at 4.8 GHz for saline ice grown at the US Army Cold Regions Research and Engineering Laboratory (CRREL). The comparison between measured and calculated complex permittivities is good for the imaginary part and the difference is within 10% for the real part.

### INTRODUCTION

Sea ice consists of crystalline ice, solid salt, liquid brine inclusions, and air bubbles. Temperature strongly affects sea ice structure, constituent characteristics, and thus its electromagnetic properties. The constituent phases in sea ice are related thermodynamically. Fractional volumes of brine inclusions and air bubbles change accordingly as the temperature of sea ice varies. For brine inclusions, the size distribution has been reported to follow the power law [1] and the shape has been observed as substantially ellipsoidal [2] for large and medium sizes and more rounded for small sizes.

When the temperature increases during a warming cycle, the shape of the inclusions becomes less ellipsoidal. For air bubbles, the shape has been considered as rather rounded in the

form of spheroids or spheres, which does not change as much as the shape of brine inclusions. Non-spherical inclusions in sea ice can have preferential alignment in the vertical direction such as in columnar ice and random orientation in azimuthal directions. In this model, the orientation distribution of scatterers is depicted with Eulerian angles. The size variation of scatterers in a species is described in terms of the number density or the fractional volume as a function of normalized volumetric sizes. For various shapes of a scattering constituent, inclusions with similar shape are treated collectively as a subspecies. Strong permittivity fluctuation theory [3] is then extended to derive the anisotropic permittivity tensor of sea ice with the above characteristics. Theoretical results are then compared with measured data for saline ice at different temperatures.

### EFFECTIVE PERMITTIVITY

Consider an inhomogeneous medium consisting of various scattering species embedded in a background medium. First, a species is defined as a set of all scatterers with the same permittivity. Within a species, scatterers of similar shape are classified into a subspecies. For simplicity, a species is now redefined as a set of all scatterers with the same permittivity and shape. Let  $\epsilon_b$  be the permittivity of the background. The inhomogeneous medium has  $N$  scatterer species of ellipsoidal shapes (which can be reduced to spheroidal or spherical shapes) with vertical alignment and random azimuthal orientation. Species  $i$  has permittivity  $\epsilon_i$ , and a fractional volume  $f_i$  in the mixture. Anisotropic effective permittivity tensor of the inhomogeneous medium is a sum of a quasi-static part and a scattering-effect part in the following expression

$$\bar{\epsilon}_{eff} = \bar{\epsilon}_g + \epsilon_0 \left[ \bar{I} - \bar{\epsilon}_{eff} \cdot \bar{S} \right]^{-1} \cdot \bar{\epsilon}_{eff} = \begin{bmatrix} \epsilon_{effx} & 0 & 0 \\ 0 & \epsilon_{effy} & 0 \\ 0 & 0 & \epsilon_{effz} \end{bmatrix} \quad (1)$$

where auxiliary permittivity  $\bar{\epsilon}_g$  and dyadic coefficient  $\bar{S}$  are derived from the condition of secular-term elimination, and the effective dyadic scatterer  $\bar{\epsilon}_{eff}$  is approximated as

$$[\bar{\epsilon}_{eff}]_{jm} = \sum_{i(s)=1}^N \int_{v_i} dv \int_0^{2\pi} d\gamma \int_0^\pi d\beta \int_0^{2\pi} d\alpha p_i(\alpha, \beta, \gamma) \sum_{k,l} \Gamma_{i\epsilon_{jklm}}^{(0)} \left\{ k_0^2 \int_{-\infty}^{\infty} d\vec{k}' [\bar{G}_g(\vec{k}')]_{kl} \Phi_{i\epsilon}(\vec{k}') + [\bar{S}_i]_{kl} \right\} \quad (2)$$

where  $i$  stands for species  $i(s)$ . Quantity  $v$  is the normalized volumetric size defined as the ratio of the volume of a scatterer over that of the smallest scatterer of the same permittivity *regardless of shape*. The integration over  $dv$  accounts for the size distribution in the size range  $v_i$  of the scatterers in species  $i$ . The probability density function of orientation is  $p_i(\alpha, \beta, \gamma)$  where  $\alpha, \beta$ , and  $\gamma$  are Eulerian angles.  $\bar{G}_g$  is the anisotropic Green's function.  $\Phi_{i\epsilon}$  is the Fourier transform of normalized exponential correlation function with correlation lengths  $\ell_{ix'}$ ,  $\ell_{iy'}$ , and  $\ell_{iz'}$ .  $\Gamma_{i\epsilon_{jklm}}^{(0)}$  is local variance of species  $i$ . The condition of secular elimination  $\langle \bar{\epsilon}(\vec{r}) \rangle = 0$  is imposed to find  $\bar{\epsilon}_g = \text{diag}(\epsilon_{gp}, \epsilon_{gp}, \epsilon_{gz})$  and then the integration in (2) is carried out to derive the effective permittivity tensor.

## PHYSICAL DESCRIPTIONS

At microwave frequencies, saline water in brine inclusions has high permittivity which strongly affects electromagnetic properties of sea ice. Size distribution of the inclusions has been reported to follow the power law [1]. The power-law distribution in terms of normalized volumetric size is described by a power-law index  $p$  and the number density  $n_0$  of brine inclusions of smallest size. The normalized volumetric size is defined as the ratio of volume of an inclusion over the volume of the smallest one. When the total fractional volume, the minimum, average, and maximum sizes of the brine inclusions are measured,  $p$  and  $n_0$  can be found and the size distribution is thus determined. At different temperature, volumes of individual brine pockets vary. By assuming that volumes of all brine inclusions change at the same rate and the density number of the inclusions is conserved, the power index can be shown to remain unchanged as the temperature varies. If characterization data are not available at all temperatures under consideration, the index obtained at a temperature may be used at a different temperature when there is no severe brine loss nor deformation. Otherwise, size measurements are necessary to determine the size distribution. For air bubbles, the size distribution is derived in the same manner or obtained from section images.

It has been observed that the shape of brine inclusions is substantially ellipsoid [2]. From ice thin sections [2], only inclusions of small sizes are seen to have a more rounded spheroidal

form. Based on this observation, a slowly varying logarithmic function is used to describe the shape distribution in terms of normalized volumetric size and axial ratios of the ellipsoids. When the temperature is increased during a warming cycle, the shape of the inclusions becomes more rounded. This structural variation in sea ice is characterized with reshaping factors operating on the maximum axial ratios. This thermal variation depicts the smoothing process which makes the brine inclusions approach the more rounded spheroidal form with increased temperature. For air bubbles, the shapes have been considered as rather rounded in the form of spheroids or spheres. Therefore, the shapes of air bubbles do not change as much as those of brine inclusions and are assumed to be unaffected by temperature.

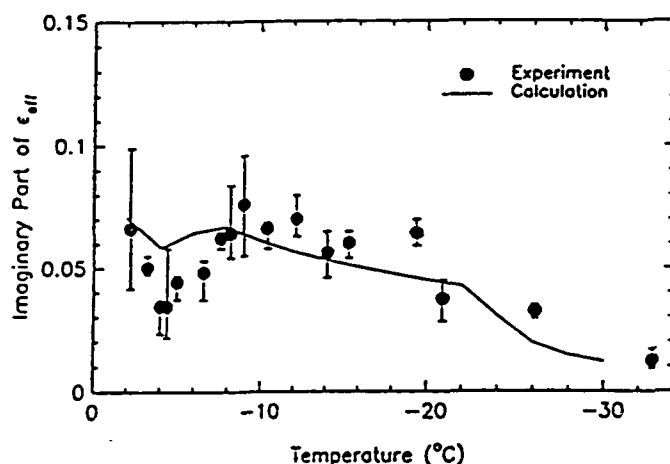
Local correlation lengths of a scatterer can also be estimated by the equivalence condition between the correlation volume and the volume of the scatterer with the same axial ratios [4]. When the size distribution is specified, local correlation lengths of a brine inclusion can therefore be calculated. Furthermore, correlation lengths also vary as a function of temperature since the size of an individual inclusion changes with temperature. If section images of sea ice are available at the temperatures under consideration, sizes of scatterers are measured to obtain the correlation lengths. If the size measurements are only made at a fix temperature  $T_0$ , correlation lengths at a different temperature  $T$  can be estimated for undeformed ice with low brine loss. Correlation lengths for air bubbles can also be obtained in the same manner.

The constituents in sea ice are ice, solid salt, brine inclusions, and air bubbles. For the background ice, the real part of permittivity is not sensitive to temperature; however, the imaginary part is dispersive and varies with temperature. An empirical formula to calculate the imaginary part of ice permittivity as a function of temperature at microwave frequencies is given in [5]. For brine in sea ice, empirical formulas to compute complex dielectric constants of brine in terms of temperatures and microwave frequencies are reported in [6]. To determine fractional volumes of brine inclusions and air bubbles in sea ice, Cox and Weeks [7] have provided equations, based on phase equilibrium, in terms of bulk ice density and salinity for the temperature range of  $-2^\circ\text{C}$  to  $-30^\circ\text{C}$ . The fractional volume of solid salt is low and will be neglected in the calculation. From characterization measurements, input parameters to the sea ice model can be obtained as discussed in this section.

## RESULTS AND DISCUSSIONS

Relative permittivities of ice were measured [2] at CRREL by using the transmission method with wave normally incident on ice slabs; thus, only  $\epsilon_{effx}$  corresponding to the ordinary wave were obtained. Ice slab 85-3 considered here was taken from a saline ice sheet to a laboratory environment. Measurements of permittivity and physical parameters were made during progressive warming of the ice slab from  $-32^\circ\text{C}$  to  $-2^\circ\text{C}$  at 4.8 GHz. During the process, there was some brine loss which can

also be incorporated in the calculations. Results are shown in the enclosed figure for the imaginary part of the relative permittivity of the saline ice. When the temperature is increased, the smoothing effect of rounded inclusions is in competition with the increasing effect of higher fractional volumes to render the slowly increasing trend in the imaginary part. The drop at temperatures higher than  $-8^{\circ}\text{C}$  can be explained by the brine loss and the kink observed at about  $-22^{\circ}\text{C}$  is due to the phase change associated with the precipitation of sodium chloride dihydrate. As seen from the figure, the theoretical curve explains all the trends observed in the experimental data for the imaginary part of the relative effective permittivity. The real parts of the permittivity is rather monotonically increased from low to high temperatures. The calculated values are lower but are within 10% of the measured data.



### SUMMARY

A model which accounts for the complexity of the multiphase inhomogeneities with multiple species characterized by orientation, size, and shapes distributions has been presented in this paper. Anisotropic effective permittivity of the inhomogeneous medium is derived with the extended strong fluctuation theory. The thermodynamics of the constituents in sea ice is also included in the model to incorporate the thermal variations in the ice structure and properties. A comparison of theoretical results with measured data for effective permittivities of saline ice is made and the trends observed from the experimental measurements are explained.

### ACKNOWLEDGMENTS

SVN and RK performed this work under contract with the National Aeronautics and Space Administration at the Jet Propulsion Laboratory, California Institute of Technology.

### REFERENCES

- [1] D. K. Perovich and A. J. Gow, "A Statistical Description of Microstructure of Young Ice," *North American Sea Ice Workshop*, University of Massachusetts, Amherst, Massachusetts, June 26-28, 1989.
- [2] S. A. Arcone, A. J. Gow, and Seth McGrew, "Structure and Dielectric Properties at 4.8 and 9.5 GHz of Saline Ice," *Journal of Geophysical Research*, Vol. 91, No. C12, pages 14281-14303, December 15, 1986.
- [3] L. Tsang and J. A. Kong, "Scattering of Electromagnetic Waves from Random Media with Strong Permittivity Fluctuations," *Radio Science*, Vol. 16, No. 3, pp. 303-320, May-June 1981.
- [4] H. A. Yueh, R. T. Shin, and J. A. Kong, "Scattering from Randomly Oriented Scatterers with Strong Permittivity Fluctuations," *Journal of Electromagnetic Waves and Applications*, Vol. 4, No. 10, pp. 983-1004, 1990.
- [5] M. E. Tiuri, A. H. Sihvola, E. G. Nyfors, and M. T. Hallikainen, "The Complex Dielectric Constant of Snow at Microwave Frequencies," *IEEE Journal of Ocean Engineering*, Vol. OE-9, No. 5, pp. 377-382, December 1984.
- [6] A. Stogryn and G. J. Desargant, "The Dielectric Properties of Brine in Sea Ice at Microwave Frequencies," *IEEE Transactions on Antennas and Propagation*, Vol. AP-33, No. 5, pp. 523-532, May 1985.
- [7] G. F. N. Cox and W. F. Weeks, "Equations for Determining the Gas and Brine Volumes in Sea-ice Samples," *Journal of Glaciology*, Vol. 29, No. 012, pp. 306-316, 1983.

# Direct and Inverse Methods in Radar Polarimetry

## Part 2

edited by

**Wolfgang-M. Boerner**

Communications & Sensing Laboratory,  
EECS Department,  
University of Illinois at Chicago, U.S.A.

**Hans Brand**

High-Frequency Engineering  
Laboratories, University Erlangen-  
Nürnberg, Germany

**Leonard A. Cram**

Thorn EMI, Electronics Ltd., U.K.

**William A. Holm**

GTRI-RAIL/MAL,  
Atlanta, GA,  
U.S.A.

**David E. Stein**

Westinghouse Electric Corporation,  
Baltimore, MD,  
U.S.A.

**Werner Wiesbeck**

IHE, University of Karlsruhe,  
Karlsruhe, Germany

**Wolfgang Keydel**

DLR, Institute for Radio-Frequency  
Technology, Oberpfaffenhofen, Germany

**Dino Giuli**

Radar Research Laboratory,  
Department of Electronics Engineering,  
University of Florence, Italy

**Dag T. Gjessing**

ESTP, Royal Norwegian Council of  
Industrial & Scientific Research, Kjeller,  
Norway

**Frédéric A. Molinet**

Société Mothesim,  
Le Plessis-Robinson,  
France



**Kluwer Academic Publishers**

Dordrecht / Boston / London

Published in cooperation with NATO Scientific Affairs Division



# THEORETICAL MODELS FOR POLARIMETRIC MICROWAVE REMOTE SENSING OF EARTH TERRAIN

M. Borgeaud

DFVLR

Institute for Radiofrequency Technology  
German Aerospace Research Establishment  
Oberpfaffenhofen  
D-8031 Wessling  
Federal Republic of Germany

and

J.A. Kong, R.T. Shin and S. V. Nghiem

Department of Electrical Engineering and Computer Science  
Massachusetts Institute of Technology  
77 Massachusetts Avenue  
Cambridge, MA 02139  
U.S.A.

## Abstract

Earth terrains are modeled by a two-layer configuration with a random permittivity described by a three-dimensional correlation function with horizontal and vertical correlation lengths and variances. Using the wave theory with Born approximations carried to the second order, this model is applied to derive the polarimetric backscattering coefficients of the Mueller and covariance matrices. From a physical point of view, the Born first- and second-order approximations account for the single and double scattering processes, respectively.

For the isotropic random permittivity configuration, five out of the nine elements of the covariance matrix are zero under the Born first-order approximation. For the uniaxial tilted random permittivity case, the covariance matrix does not contain any zero elements. To account for the azimuthal randomness in the growth direction of leaves in tree and grass fields, an averaging scheme is developed in which the backscattering coefficients are averaged over the azimuthal direction. In this case, the covariance matrix is described by four zero elements though the tilt angle is different from zero. Applying the Born approximation to the second-order, the covariance matrix is computed for the isotropic and the uniaxial untilted random permittivity configurations. The covariance matrix has four zero elements, and a depolarization factor is obtained, even for the isotropic case.

To describe the effect of the random medium on electromagnetic waves, the strong permittivity fluctuation theory, which accounts for the losses due to both of the absorption and the scattering, is used to compute the effective permittivity of the medium. For a mixture of two components, only the frequency, the correlation lengths, the fractional volume, and the permittivities of the two constituents are needed to obtain the polarimetric backscattering coefficients. Theoretical predictions are illustrated by comparing the results with experimental data for vegetation fields and sea ice.

1159

W.-M. Boerner et al. (eds.), *Direct and Inverse Methods in Radar Polarimetry*, Part 2, 1159-1189.  
© 1992 Kluwer Academic Publishers. Printed in the Netherlands.

## Introduction

For many types of earth terrain, the scattering effects due to medium inhomogeneities play an important role in the determination of radar backscattering coefficients. The volume scattering properties of a medium have been successfully modeled by the random permittivity fluctuations [1]. The random medium is characterized by a background permittivity and a random permittivity fluctuation modeled by a three-dimensional correlation function with horizontal and vertical correlation lengths and variances.

The objective of this paper is to develop a mathematically rigorous, fully polarimetric model to compute the covariance matrices in the backscattering direction for different kinds of earth terrains with a two-layer configuration medium with either an isotropic or an anisotropic random permittivity. Of all the analytical wave approaches to the study of scattering by random medium, the Born approximation is the simplest. An integral equation is first formed for the electric field using the unperturbed Green's function in the absence of permittivity fluctuations. The integral equation is then solved by iteration with the iteration series known as the Born series. With both the first and second terms of this series which respectively describes a single and a double scattering processes, the polarimetric backscattering coefficients are computed.

## Scattering, Mueller, and Covariance Matrices

Consider an electromagnetic plane wave propagating in the direction  $\vec{k}$ .

$$\vec{E} = (E_h \hat{h} + E_v \hat{v}) e^{i\vec{k} \cdot \vec{r}} \quad (1)$$

where  $E_h$  is the horizontal component,  $E_v$  is the vertical component,  $\hat{h}$  and  $\hat{v}$  are two orthogonal unit vectors satisfying the relation  $\hat{v} \times \hat{h} = \hat{k}$ . Consider an incident plane wave  $\vec{E}_i$  impinging on a particle. This particle will radiate and the scattered electric field  $\vec{E}_s$  can be related to the incident electric field  $\vec{E}_i$  by the scattering matrix [2]:

$$\begin{pmatrix} E_{hs} \\ E_{vs} \end{pmatrix} = \begin{pmatrix} HH & HV \\ VH & VV \end{pmatrix} \cdot \begin{pmatrix} E_{hi} \\ E_{vi} \end{pmatrix} \quad (2)$$

The elements of the scattering matrix are complex and the relation  $VH = HV$  holds [1] in the backscattering direction and for reciprocal media.

Instead of relating the scattered electric field to the incident electric field, the modified Stokes vector, defined by [1], can also be used to relate the scattered Stokes vector to the incident Stokes vector:

$$I_H = \frac{|E_h|^2}{\eta} \quad I_V = \frac{|E_v|^2}{\eta} \quad U = \frac{2}{\eta} \text{Re}(E_h E_v^*) \quad V = \frac{2}{\eta} \text{Im}(E_h E_v^*) \quad (3)$$

This definition is chosen since the first two modified Stokes parameters represent the intensity of the wave in the horizontal and vertical polarizations:

$$\bar{I} = \begin{pmatrix} I_H \\ I_V \\ U \\ V \end{pmatrix} \quad (4)$$

In terms of the elements of the scattering matrix (2), the Mueller matrix  $\bar{M}$  relates the scattered to the incident Stokes vectors according to

$$\bar{I}_s = \bar{M} \cdot \bar{I}_i \quad (5)$$

is found to be

$$\begin{pmatrix} |HH|^2 & |HV|^2 & \operatorname{Re}(HH \cdot HV^*) & -\operatorname{Im}(HH \cdot HV^*) \\ |VH|^2 & |VV|^2 & \operatorname{Re}(VH \cdot VV^*) & -\operatorname{Im}(VH \cdot VV^*) \\ 2\operatorname{Re}(HH \cdot VH^*) & 2\operatorname{Re}(HV \cdot VV^*) & \operatorname{Re}(HH \cdot VV^* + HV \cdot VH^*) & -\operatorname{Im}(HH \cdot VV^* - HV \cdot VH^*) \\ 2\operatorname{Im}(HH \cdot VH^*) & 2\operatorname{Im}(HV \cdot VV^*) & \operatorname{Im}(HH \cdot VV^* + HV \cdot VH^*) & \operatorname{Re}(HH \cdot VV^* - HV \cdot VH^*) \end{pmatrix} \quad (6)$$

where all the Mueller matrix elements are real numbers. From the four elements of the scattering matrix (2), the covariance matrix may also be defined. In general the covariance is a complex matrix of sixteen elements. In the special case of the backscattering direction and for a reciprocal medium, the covariance matrix is transformed to a matrix of nine elements as follows

$$\bar{C} = \begin{pmatrix} HH \\ HV \\ VV \end{pmatrix} \begin{pmatrix} HH^* & HV^* & VV^* \end{pmatrix} = \begin{pmatrix} |HH|^2 & HH \cdot HV^* & HH \cdot VV^* \\ HV \cdot HH^* & |HV|^2 & HV \cdot VV^* \\ VV \cdot HH^* & VV \cdot HV^* & |VV|^2 \end{pmatrix} \quad (7)$$

By comparing the scattering (2), the Mueller (6), and the covariance matrices (7), it is easily seen that all the polarimetric information may be expressed in any of these matrices. The covariance and Mueller matrices can be transformed to each other since they contain the same information. However, from these two matrices, the scattering matrix cannot be fully retrieved because the absolute phase factor is not taken into account in either the covariance matrix or in the Mueller matrix.

In our study of microwave remote sensing, the random medium model is used to simulate the permittivity of the earth terrain. This implies that the simple case of a single particle can no longer be considered but the ensemble average of the electric field needs to be calculated. The polarimetric bistatic scattering coefficient  $\gamma_{\mu\nu\kappa}(\bar{k}_i, \bar{k}_s)$  is defined by [3]

$$\gamma_{\mu\nu\kappa}(\bar{k}_i, \bar{k}_s) = \lim_{r \rightarrow \infty} \frac{4\pi r^2}{A \cos \theta_{0i}} \frac{\langle E_{\mu s} E_{\nu s}^* \rangle}{E_{\tau i} E_{\kappa i}^*} = \lim_{r \rightarrow \infty} \frac{4\pi r^2}{A \cos \theta_{0i}} \langle \mu \tau \cdot \nu \kappa^* \rangle \quad (8)$$

where  $A$  is the area illuminated by the radar,  $r$  is the distance between the radar and the observed terrain, and  $\theta_{0i}$  is the polar incident angle. Furthermore,  $\bar{k}_i$  and  $\bar{k}_s$  are the incident and scattered wave vectors, respectively. The subscripts  $s$  and  $i$  stand for scattered and incident waves, respectively. Finally,  $\mu\tau$  and  $\nu\kappa$  are the four components of the scattering matrix where  $\mu$ ,  $\tau$ ,  $\nu$ , and  $\kappa$  represent either the horizontal  $h$  or vertical  $v$  polarizations.

The polarimetric backscattering coefficient  $\sigma_{\mu\tau\nu\kappa}$  is defined [3] from the bistatic coefficient when  $\bar{k}_s = -\bar{k}_i$

$$\sigma_{\mu\tau\nu\kappa} = \gamma_{\mu\tau\nu\kappa}(\bar{k}_i, -\bar{k}_i) \cos \theta_{0i} = \lim_{\substack{A \rightarrow \infty \\ r \rightarrow \infty}} \frac{4\pi r^2}{A} \frac{\langle E_{\mu s} E_{\nu s}^* \rangle}{E_{\tau i} E_{\kappa i}^*} = \lim_{\substack{A \rightarrow \infty \\ r \rightarrow \infty}} \frac{4\pi r^2}{A} \langle \mu\tau \cdot \nu\kappa^* \rangle \quad (9)$$

The polarimetric backscattering coefficients  $\sigma_{\mu\tau\nu\kappa}$  are complex except the three "traditional" real-valued backscattering coefficients

$$\begin{aligned} \sigma_{hhhh} &\Rightarrow \sigma_{hh} \\ \sigma_{hhvv} &\Rightarrow \sigma_{hv} \\ \sigma_{vvvv} &\Rightarrow \sigma_{vv} \end{aligned} \quad (10)$$

Similarly, the covariance matrix (7) constituted by the different polarimetric backscattering coefficients can be derived

$$\bar{C} = \lim_{\substack{A \rightarrow \infty \\ r \rightarrow \infty}} \frac{4\pi r^2}{A} \begin{pmatrix} HH \\ HV \\ VV \end{pmatrix} \cdot (HH^* \quad HV^* \quad VV^*) = \begin{pmatrix} \sigma_{hh} & \sigma_{hhvv} & \sigma_{hhvv} \\ \sigma_{hhvv}^* & \sigma_{hv} & \sigma_{hvvv} \\ \sigma_{hhvv} & \sigma_{hvvv}^* & \sigma_{vv} \end{pmatrix} \quad (11)$$

Therefore, the complete polarimetric information can be obtained by computing only six backscattering coefficients in which three are real ( $\sigma_{hh}$ ,  $\sigma_{hv}$ , and  $\sigma_{vv}$ ) and three are complex ( $\sigma_{hhvv}$ ,  $\sigma_{hhvv}^*$ ,  $\sigma_{hvvv}$ ).

## Formulation

Consider an electromagnetic plane wave impinging upon a two-layer random medium configuration as shown in Fig. 1. The top layer represents free space with a permittivity  $\epsilon_0$  while the bottom layer has a deterministic permittivity  $\epsilon_2$ . In between, a layer with thickness  $d$  and extending infinitely in the lateral direction is characterized by a random permittivity  $\epsilon_1(\bar{r})$

$$\epsilon_1(\bar{r}) = \epsilon_{1m} + \epsilon_{1f}(\bar{r}) \quad (12)$$

This random variable has a mean value  $\epsilon_{1m}$  and a small fluctuating term  $\epsilon_{1f}(\bar{r})$  whose average is zero. The wave equations for both regions may be written as

$$\nabla \times \nabla \times \bar{E}_0(\bar{r}) - k_0^2 \bar{E}_0(\bar{r}) = 0 \quad (13)$$



$$\nabla \times \nabla \times \bar{E}_1(\bar{r}) - k_{1m}^2 \bar{E}_1(\bar{r}) = Q(\bar{r}) \bar{E}_1(\bar{r}) \quad (14)$$

where  $\bar{E}_0(\bar{r})$  and  $\bar{E}_1(\bar{r})$  denote the electric fields fluctuation in region 0 and region 1, respectively.

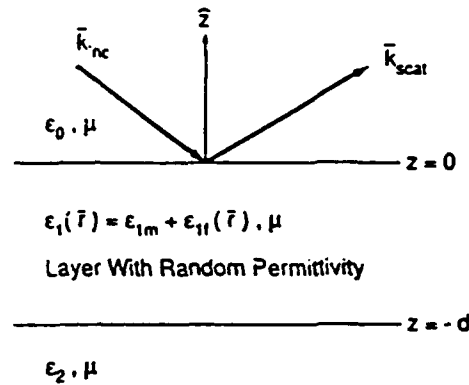


Figure 1: Isotropic two-layer configuration.

Furthermore, the following variables have been defined

$$k_0^2 = \omega^2 \mu \epsilon_0 \quad k_{1m}^2 = \omega^2 \mu \epsilon_{1m} \quad Q(\bar{r}) = \omega^2 \mu \epsilon_{1f}(\bar{r}) \quad (15)$$

With the effective source term  $Q(\bar{r}) \bar{E}_1(\bar{r})$ , (13) and (14) can be expressed in integral form as follows

$$\bar{E}_0(\bar{r}) = \bar{E}_0^{(0)}(\bar{r}) + \int d^3 \bar{r}_1 \bar{G}_{01}(\bar{r}, \bar{r}_1) Q(\bar{r}_1) \cdot \bar{E}_1(\bar{r}_1) \quad (16)$$

$$\bar{E}_1(\bar{r}) = \bar{E}_1^{(0)}(\bar{r}) + \int d^3 \bar{r}_1 \bar{G}_{11}(\bar{r}, \bar{r}_1) Q(\bar{r}_1) \cdot \bar{E}_1(\bar{r}_1) \quad (17)$$

where  $\bar{E}_0^{(0)}(\bar{r})$  and  $\bar{E}_1^{(0)}(\bar{r})$  are the specular or coherent electric fields in the absence of random permittivity in region 1. Furthermore  $\bar{G}_{01}(\bar{r}, \bar{r}_1)$  and  $\bar{G}_{11}(\bar{r}, \bar{r}_1)$  are the dyadic Green's functions for observers in regions 0 and 1, respectively, with the source in region 1. Solutions to these two coupled equations can be obtained by iteration. Substituting (17) into (16), the total electric field in region 0 is found to be in form of the Neumann series

$$\bar{E}_0(\bar{r}) = \bar{E}_0^{(0)}(\bar{r}) + \sum_{n=1}^{\infty} \bar{E}_0^{(n)}(\bar{r}) \quad (18)$$

where the  $n^{\text{th}}$  order field is given by

$$\bar{E}_0^{(n)}(\bar{r}) = \int d^3\bar{r}_1 \cdots d^3\bar{r}_n \bar{G}_{01}(\bar{r}, \bar{r}_1) Q(\bar{r}_1) \cdot \bar{G}_{11}(\bar{r}_1, \bar{r}_2) Q(\bar{r}_2) \cdots \bar{G}_{11}(\bar{r}_{n-1}, \bar{r}_n) Q(\bar{r}_n) \cdot \bar{E}_1^{(0)}(\bar{r}_n) \quad (19)$$

The so-called "Born first-order approximation" is obtained by letting  $n = 1$  in the previous equation. Hence

$$\bar{E}_0^{(1)}(\bar{r}) = \int d^3\bar{r}_1 \bar{G}_{01}(\bar{r}, \bar{r}_1) Q(\bar{r}_1) \cdot \bar{E}_1^{(0)}(\bar{r}_1) \quad (20)$$

and the "Born second-order approximation" is derived by letting  $n = 2$

$$\bar{E}_0^{(2)}(\bar{r}) = \int d^3\bar{r}_1 d^3\bar{r}_2 \bar{G}_{01}(\bar{r}, \bar{r}_1) Q(\bar{r}_1) \cdot \bar{G}_{11}(\bar{r}_1, \bar{r}_2) Q(\bar{r}_2) \cdot \bar{E}_1^{(0)}(\bar{r}_2) \quad (21)$$

## Born First-Order Approximation

### a) Isotropic random medium model

Consider an electromagnetic plane wave impinging upon a two-layer random medium configuration as shown in Fig. 1. For an incident electric field in region 0 of the following form

$$\bar{E}_0(\bar{r}) = [E_{0h}\hat{h}(-k_{0zi})e^{-ik_{0zi}z} + E_{0v}\hat{v}(-k_{0zi})e^{-ik_{0zi}z}] e^{i\bar{k}_0 \cdot \bar{r}} \quad (22)$$

where  $\hat{h}(-k_{0zi})$  and  $\hat{v}(-k_{0zi})$  are respectively the horizontal and vertical unit vectors in region 0 associated with down-going waves, the coherent electric field in the random medium is obtained [4]

$$\begin{aligned} \bar{E}_1^{(0)}(\bar{r}) = & \{ E_{0h} [A_{hi}\hat{h}(k_{1zi})e^{ik_{1zi}z} + B_{hi}\hat{h}(-k_{1zi})e^{-ik_{1zi}z}] \\ & + E_{0v} [A_{vi}\hat{v}(k_{1zi})e^{ik_{1zi}z} + B_{vi}\hat{v}(-k_{1zi})e^{-ik_{1zi}z}] \} e^{i\bar{k}_0 \cdot \bar{r}} \end{aligned} \quad (23)$$

in which the following coefficients are defined [3]

$$\begin{aligned} A_{hi} &= \frac{X_{01i}}{D_{2i}} R_{12i} e^{i2k_{1zi}d} & A_{vi} &= \frac{k_0}{k_1} \frac{Y_{01i}}{F_{2i}} S_{12i} e^{i2k_{1zi}d} \\ B_{hi} &= \frac{X_{01i}}{D_{2i}} & B_{vi} &= \frac{k_0}{k_1} \frac{Y_{01i}}{F_{2i}} \\ D_{2i} &= 1 + R_{01i}R_{12i} e^{i2k_{1zi}d} & F_{2i} &= 1 + S_{01i}S_{12i} e^{i2k_{1zi}d} \\ R_{abi} &= \frac{k_{azi} - k_{bzi}}{k_{azi} + k_{bzi}} & S_{abi} &= \frac{\epsilon_b k_{azi} - \epsilon_a k_{bzi}}{\epsilon_b k_{azi} + \epsilon_a k_{bzi}} \\ X_{abi} &= 1 + R_{abi} & Y_{abi} &= 1 + S_{abi} \end{aligned} \quad (24)$$

As can be seen in (23), the  $A$  coefficients are associated with the up-going waves while the  $B$  coefficients describe the down-going waves. Under the far-field approximation, the Green's function in (20) takes the following form in the backscattering direction [5]

$$\bar{G}_{01}(\bar{r}, \bar{r}_1) = \hat{h}(-k_{0zi})\bar{G}_{01h}(\bar{r}, \bar{r}_1) + \hat{v}(-k_{0zi})\bar{G}_{01v}(\bar{r}, \bar{r}_1) \quad (25)$$

$$\bar{G}_{01h}(\bar{r}, \bar{r}_1) = \frac{e^{ik_{0z}r}}{4\pi r} [A_{hi}\hat{h}(k_{1zi})e^{ik_{1zi}z_1} + B_{hi}\hat{h}(-k_{1zi})e^{-ik_{1zi}z_1}] e^{i\bar{k}_0 \cdot \bar{r}_1} \quad (26)$$

$$\bar{G}_{01v}(\bar{r}, \bar{r}_1) = \frac{e^{ik_{0z}r}}{4\pi r} [A_{vi}\hat{v}(k_{1zi})e^{ik_{1zi}z_1} + B_{vi}\hat{v}(-k_{1zi})e^{-ik_{1zi}z_1}] e^{i\bar{k}_0 \cdot \bar{r}_1} \quad (27)$$

For each polarization, both  $\bar{G}_{01}(\bar{r}, \bar{r}_1)$  and  $\bar{E}_1^{(0)}(\bar{r})$  are constituted by a down- and an up-going waves. Therefore,  $\bar{E}_0^{(1)}(\bar{r})$  is formed by the sum of four different terms as shown in Fig. 2. All the multiple reflections occurring at the boundaries are also incorporated in the model and the backscattered wave is due to the single scattering process under the Born first-order approximation.

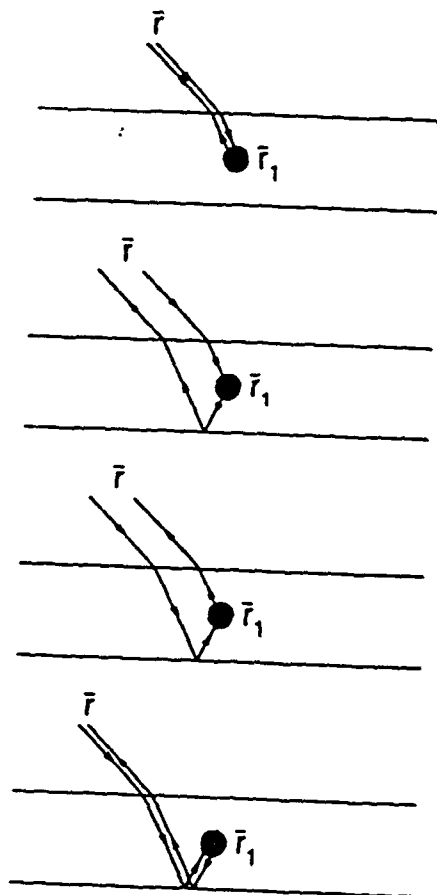


Figure 2: Physical interpretation for Born first-order approximation.

To compute the polarimetric backscattering coefficients (9), only the components of the backscattered electric field are needed. Furthermore, the polarization of the incident wave  $\vec{E}_1^{(0)}(\vec{r})$  is only along one direction, either horizontal or vertical. With the Fourier transform of the autocorrelation of the permittivity fluctuation for a statistical homogeneous random medium

$$\langle Q(\vec{r}_1)Q(\vec{r}_2)^* \rangle = \delta\omega^4 \mu^2 |\epsilon_{1m}|^2 \int_{-\infty}^{\infty} d^3\vec{\beta} \Phi(\vec{\beta}) e^{-i\vec{\beta} \cdot (\vec{r}_1 - \vec{r}_2)} \quad (28)$$

the ensemble average for the first-order backscattered intensity takes the following form

$$\langle E_{0\mu}^{(1)}(\bar{r}) E_{0\nu}^{(1)}(\bar{r})^* \rangle = \delta\omega^4 \mu^2 |\epsilon_{1m}|^2 \int d^3\bar{r}_1 d^3\bar{r}_2 \int d^3\bar{\beta} \Phi(\bar{\beta}) e^{-i\bar{\beta} \cdot (\bar{r}_1 - \bar{r}_2)} \left[ \bar{G}_{01\mu}(\bar{r}, \bar{r}_1) \cdot \bar{E}_{1\tau}^{(0)}(\bar{r}_1) \right] \left[ \bar{G}_{01\nu}(\bar{r}, \bar{r}_2) \cdot \bar{E}_{1\kappa}^{(0)}(\bar{r}_2) \right]^* \quad (29)$$

where  $\tau$  and  $\kappa$  represent either the horizontal or vertical component of the transmitted wave and  $\mu$  and  $\nu$  represent either the horizontal or vertical component of the received wave. From (23), the following term has been defined

$$\bar{E}_{1\alpha}^{(0)}(\bar{r}) = \sum_{p=-1}^1 E_{0\alpha i} X_{\alpha p i} \hat{\alpha}(pk_{1zi}) e^{ipk_{1zi}z} e^{i\bar{k}_p \cdot \bar{r}} \quad (30)$$

where  $\alpha$  stands either for  $h$  or  $v$ , and  $p$  describes either up or down-going waves. In a similar manner,

$$\bar{G}_{01\alpha}(\bar{r}, \bar{r}_1) = \frac{e^{ik_0 r}}{4\pi r} \sum_{p=-1}^1 X_{\alpha p i} \hat{\alpha}(pk_{1zi}) e^{ipk_{1zi}z_1} e^{i\bar{k}_p \cdot \bar{r}_1} \quad (31)$$

where the following definitions have been used

$$X_{h1i} = A_{hi} \quad X_{h-1i} = B_{hi} \quad X_{v1i} = A_{vi} \quad X_{v-1i} = B_{vi} \quad (32)$$

Substituting (30) and (31) into (29), a sum of 16 terms is obtained

$$\begin{aligned} \langle E_{0\mu}^{(1)}(\bar{r}) E_{0\nu}^{(1)}(\bar{r})^* \rangle &= \frac{\delta\omega^4 \mu^2 |\epsilon_{1m}|^2}{16\pi^2 r^2} E_{0\tau i} E_{0\kappa i}^* \sum_{p,q,r,s=-1}^1 [X_{\mu p i} X_{\tau q i} \hat{\mu}(pk_{1zi}) \cdot \hat{\tau}(qk_{1zi})] \\ &\quad [X_{\nu r i} X_{\kappa s i} \hat{\nu}(rk_{1zi}) \cdot \hat{\kappa}(sk_{1zi})]^* \int d^3\bar{r}_1 d^3\bar{r}_2 \int d^3\bar{\beta} \Phi(\bar{\beta}) \\ &\quad e^{-i\bar{\beta} \cdot (\bar{r}_1 - \bar{r}_2)} \left[ e^{i(pk_{1zi} + qk_{1zi})z_1} e^{2i\bar{k}_p \cdot \bar{r}_1} \right] \left[ e^{i(rk_{1zi} + sk_{1zi})z_2} e^{2i\bar{k}_r \cdot \bar{r}_2} \right]^* \quad (33) \end{aligned}$$

As can be seen, all the polarization information is contained outside the integral. Also, the intensity is expressed as a sum of sixteen terms since the electric field is composed of four elements. With the two following scalar quantities

$$\Psi_{\mu\tau\nu\kappa}^{pqrs} = X_{\mu p i} X_{\tau q i} X_{\nu r i}^* X_{\kappa s i}^* \quad (34)$$

$$\Omega_{\mu\tau\nu\kappa}^{pqrs} = [\hat{\mu}(pk_{1zi}) \cdot \hat{\tau}(qk_{1zi})] [\hat{\nu}(rk_{1zi}) \cdot \hat{\kappa}(sk_{1zi})]^* \quad (35)$$

(33) can be written as

$$\begin{aligned} \langle E_{0\mu}^{(1)}(\bar{r}) E_{0\nu}^{(1)}(\bar{r})^* \rangle &= \frac{\delta\omega^4 \mu^2 |\epsilon_{1m}|^2}{16\pi^2 r^2} E_{0\tau i} E_{0\kappa i}^* \sum_{p,q,r,s=-1}^1 \Psi_{\mu\tau\nu\kappa}^{pqrs} \Omega_{\mu\tau\nu\kappa}^{pqrs} \int d^3\bar{r}_1 d^3\bar{r}_2 \\ &\quad \int d^3\bar{\beta} \Phi(\bar{\beta}) e^{-i\bar{\beta} \cdot (\bar{r}_1 - \bar{r}_2)} \left[ e^{i(pk_{1zi} + qk_{1zi})z_1} e^{2i\bar{k}_p \cdot \bar{r}_1} \right] \\ &\quad \left[ e^{i(rk_{1zi} + sk_{1zi})z_2} e^{2i\bar{k}_r \cdot \bar{r}_2} \right]^* \quad (36) \end{aligned}$$

The integrals in (36) are solved by decomposing the variables of integration into their lateral and vertical components. By using the property of the Delta function and introducing the illuminated area  $A$ , the integration over the lateral variables  $\bar{\rho}_1$ ,  $\bar{\rho}_2$ , and  $\bar{\beta}_\rho$  yields

$$\begin{aligned} \langle E_{0\mu}^{(1)}(\bar{r}) E_{0\nu}^{(1)}(\bar{r})^* \rangle &= \frac{\delta\omega^4 \mu^2 |\epsilon_{lm}|^2 A}{4r^2} E_{0ri} E_{0\kappa i}^* \sum_{p,q,r,s=-1}^1 \Psi_{\mu\tau\nu\kappa}^{pqrs} \Omega_{\mu\tau\nu\kappa}^{pqrs} \int d\beta_z dz_1 dz_2 \\ &\quad \Phi(\bar{\beta}_\rho = 2\bar{k}_{\rho i}, \beta_z) e^{iz_1[pk_{1zi} + qk_{1zi} - \beta_z]} e^{-iz_2[(rk_{1zi} + sk_{1zi})^* - \beta_z]} \end{aligned} \quad (37)$$

In order to solve the last set of equations, let us define first the two complex quantities

$$a = pk_{1zi} + qk_{1zi} \quad b = [rk_{1zi} + sk_{1zi}]^* \quad (38)$$

Hence, the integral part of (37) may be written

$$\int dz_1 dz_2 e^{ia z_1} e^{-ib z_2} \int d\beta_z \Phi(\bar{\beta}_\rho = 2\bar{k}_{\rho i}, \beta_z) e^{-i\beta_z(z_1 - z_2)} \quad (39)$$

Due to Cauchy's theorem, the integral over  $\beta_z$  yields the following expression by distinguishing two cases depending upon the sign of  $z_1 - z_2$

$$\int d\beta_z \Phi(2\bar{k}_{\rho i}, \beta_z) e^{-i\beta_z(z_1 - z_2)} = \begin{cases} 2\pi i \operatorname{Res} \Phi(2\bar{k}_{\rho i}, \beta_z^+) e^{-i\beta_z^+(z_1 - z_2)} & \text{if } z_1 < z_2 \\ -2\pi i \operatorname{Res} \Phi(2\bar{k}_{\rho i}, \beta_z^-) e^{-i\beta_z^-(z_1 - z_2)} & \text{if } z_1 > z_2 \end{cases} \quad (40)$$

where it is assumed that the spectrum density  $\Phi(\bar{\beta}_\rho, \beta_z)$  has only one pair of complex conjugate poles at  $\beta_z = \beta_z^\pm$ , and  $\Phi(\bar{\beta}_\rho, \beta_z)$  vanishes everywhere on the infinite circle. For the random medium of infinite lateral dimension and vertical extension from  $z = -d$  to  $z = 0$ , (39) becomes

$$\begin{aligned} &2\pi i \operatorname{Res} \Phi(\bar{\beta}_\rho = 2\bar{k}_{\rho i}, \beta_z^+) \int_{-d}^0 dz_1 \int_{z_1}^0 dz_2 e^{iz_1(a - \beta_z^+)} e^{-iz_2(b - \beta_z^+)} \\ &- 2\pi i \operatorname{Res} \Phi(\bar{\beta}_\rho = 2\bar{k}_{\rho i}, \beta_z^-) \int_{-d}^0 dz_1 \int_{-d}^{z_1} dz_2 e^{iz_1(a - \beta_z^-)} e^{-iz_2(b - \beta_z^-)} \end{aligned} \quad (41)$$

For  $\operatorname{Res}(\bar{\beta}_\rho = 2\bar{k}_{\rho i}, \beta_z^-) = -\operatorname{Res}(\bar{\beta}_\rho = 2\bar{k}_{\rho i}, \beta_z^+)$ , these integrals may be easily solved to get

$$\begin{aligned} &2\pi i \operatorname{Res} \Phi(\bar{\beta}_\rho = 2\bar{k}_{\rho i}, \beta_z^+) \left[ \frac{1 - e^{-i(a - \beta_z^+)d}}{(a - \beta_z^+)(b - \beta_z^+)} - \frac{1 - e^{-i(a - b)d}}{(a - b)(b - \beta_z^+)} \right. \\ &\left. + \frac{1 - e^{-i(a - b)d}}{(a - b)(b - \beta_z^-)} - \frac{e^{i(b - \beta_z^-)d}}{(a - \beta_z^-)(b - \beta_z^-)} + \frac{e^{-i(a - b)d}}{(a - \beta_z^-)(b - \beta_z^-)} \right] \end{aligned} \quad (42)$$

To simplify the expression, let us define the following term

$$I^{pqrs} = \left[ \frac{1 - e^{-i(a-\beta_z^+)d}}{(a-\beta_z^+)(b-\beta_z^+)} - \frac{1 - e^{-i(a-b)d}}{(a-b)(b-\beta_z^+)} + \frac{1 - e^{-i(a-b)d}}{(a-b)(b-\beta_z^-)} - \frac{e^{i(b-\beta_z^-)d}}{(a-\beta_z^-)(b-\beta_z^-)} + \frac{e^{-i(a-b)d}}{(a-\beta_z^-)(b-\beta_z^-)} \right] \quad (43)$$

From (38),  $a$  is different from  $b$  for most cases because of the complex conjugation. However, for the special case when  $a = b = 0$ , (43) may be written as

$$I^{pqrs} = \left[ \frac{1 - e^{i\beta_z^+d}}{\beta_z^{+2}} + \frac{id}{\beta_z^+} - \frac{id}{\beta_z^-} + \frac{1 - e^{-i\beta_z^-d}}{\beta_z^{-2}} \right] \quad (44)$$

Substituting (43) and (44) into (37) and using (9), the polarimetric backscattering coefficients are found to be

$$\sigma_{\mu\nu\kappa} = 2\pi^2\delta\omega^4\mu^2|\epsilon_{1m}|^2 iRes\Phi(\bar{\beta}_\rho = 2\bar{k}_{\rho i}, \beta_z^+) \sum_{p,q,r,s=-1}^1 \Psi_{\mu\nu\kappa}^{pqrs} \Omega_{\mu\nu\kappa}^{pqrs} I^{pqrs} \quad (45)$$

Only three polarimetric backscattering coefficients are different from zero. This comes from the factor  $\Omega_{\mu\nu\kappa}^{pqrs}$  in (35). They are zero due to the definition of the unit vectors [3]. Hence, the final results are

$$\begin{aligned} \sigma_{hh} &= 2\pi^2\delta\omega^4\mu^2|\epsilon_{1m}|^2 iRes\Phi(\bar{\beta}_\rho = 2\bar{k}_{\rho i}, \beta_z^+) \sum_{p,q,r,s=-1}^1 \Psi_{hhhh}^{pqrs} I^{pqrs} \\ \sigma_{vv} &= 2\pi^2\delta\omega^4\mu^2|\epsilon_{1m}|^2 iRes\Phi(\bar{\beta}_\rho = 2\bar{k}_{\rho i}, \beta_z^+) \sum_{p,q,r,s=-1}^1 \Psi_{vvvv}^{pqrs} \Omega_{vvvv}^{pqrs} I^{pqrs} \\ \sigma_{hhvv} &= 2\pi^2\delta\omega^4\mu^2|\epsilon_{1m}|^2 iRes\Phi(\bar{\beta}_\rho = 2\bar{k}_{\rho i}, \beta_z^+) \sum_{p,q,r,s=-1}^1 \Psi_{hhvv}^{pqrs} \Omega_{hhvv}^{pqrs} I^{pqrs} \end{aligned} \quad (46)$$

$$\sigma_{hv} = \sigma_{vh} = \sigma_{hhvv} = \sigma_{vvvv} = 0 \quad (47)$$

For an autocorrelation function for the random permittivity (12) of the form

$$\langle \epsilon_{1f}(\bar{r}_1)\epsilon_{1f}(\bar{r}_2)^* \rangle = \delta|\epsilon_{1m}|^2 e^{-\frac{|\bar{r}_1-\bar{r}_2|^2}{l_p^2}} e^{-\frac{|\bar{r}_1-\bar{r}_2|^2}{l_v^2}} e^{-\frac{|\bar{r}_1-\bar{r}_2|^2}{l_z^2}} \quad (48)$$

where  $\delta$  is the variance,  $l_p$  and  $l_z$  are the lateral and vertical correlation lengths, respectively, the spectrum density (28) is given by

$$\Phi(\beta_x, \beta_y, \beta_z) = \frac{l_p^2 l_z}{\pi^3 (1 + \beta_x^2 l_p^2) (1 + \beta_y^2 l_p^2) (1 + \beta_z^2 l_z^2)} \quad (49)$$

The spectral density goes to zero as  $\bar{\beta}$  tends to infinity satisfying the requirement for the complex integration (40). The poles  $\beta_z$  of the spectrum density are obtained

$$\beta_z^{\pm} = \pm \frac{i}{l_z} \quad (50)$$

Furthermore, the associated residues are found to be

$$\text{Res} \Phi(\beta_x, \beta_y, \beta_z^{\pm}) = \pm \frac{l_p^2}{2\pi^3 i (1 + \beta_x^2 l_p^2) (1 + \beta_y^2 l_p^2)} \quad (51)$$

#### b) Anisotropic random medium model

In order to describe earth terrains exhibiting an anisotropic behavior, the random permittivity is chosen to be uniaxial in a tilted coordinate system [6]. Earth terrains such as sea ice and corn fields display such a property. From (12), the random permittivity is written in a tensor form

$$\bar{\epsilon}_1(\bar{r}) = \bar{\epsilon}_{1m} + \bar{\epsilon}_{1f}(\bar{r}) \quad (52)$$

where  $\bar{\epsilon}_{1f}(\bar{r})$  is a function of position characterizing the randomly fluctuating component of the permittivity. For the random medium, it is assumed that both  $\bar{\epsilon}_{1m}$  and  $\bar{\epsilon}_{1f}(\bar{r})$  are uniaxial in a coordinate system  $xy'z'$  tilted respectively at an angle  $\psi$ ,  $\psi_f$  around the  $\bar{z}$  axis as represented in Fig. 3. In this tilted coordinate system, the permittivity tensor  $\bar{\epsilon}_{1m}$  takes the following form

$$\bar{\epsilon}_{1m} = \begin{pmatrix} \epsilon_1 & 0 & 0 \\ 0 & \epsilon_1 & 0 \\ 0 & 0 & \epsilon_{1z} \end{pmatrix} \quad (53)$$

In the coordinate system  $xyz$ , the permittivity tensor can be expressed as

$$\bar{\epsilon}_{1m} = \begin{pmatrix} \epsilon_{11} & 0 & 0 \\ 0 & \epsilon_{22} & \epsilon_{23} \\ 0 & \epsilon_{32} & \epsilon_{33} \end{pmatrix} \quad (54)$$

where

$$\begin{aligned} \epsilon_{11} &= \epsilon_1 \\ \epsilon_{22} &= \epsilon_1 \cos^2 \psi + \epsilon_{1z} \sin^2 \psi \\ \epsilon_{23} &= \epsilon_{32} = (\epsilon_{1z} - \epsilon_1) \sin \psi \cos \psi \\ \epsilon_{33} &= \epsilon_1 \sin^2 \psi + \epsilon_{1z} \cos^2 \psi \end{aligned} \quad (55)$$



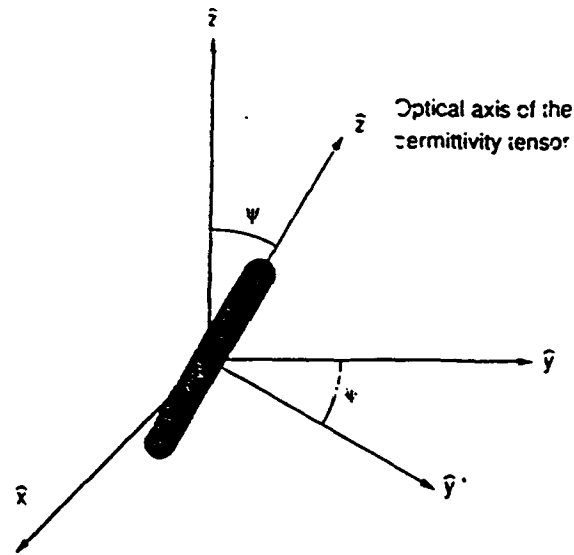


Figure 3: Geometrical configuration of the permittivity tensor in an anisotropic random medium.

Similar equations may be written for  $\bar{\epsilon}_{1f}(\bar{r})$  with the tilt angle  $\psi_f$ . From (20), the "Born first-order approximation" yields for the anisotropic case

$$\bar{E}_0^{(1)}(\bar{r}) = \int d^3\bar{r}_1 \bar{G}_{01}(\bar{r}, \bar{r}_1) \cdot \bar{Q}(\bar{r}_1) \cdot \bar{E}_1^{(0)}(\bar{r}_1) \quad (56)$$

where  $\bar{Q}(\bar{r}) = \omega^2 \mu \bar{\epsilon}_{1f}(\bar{r})$ . Using Euler notation and decomposing the electric field in horizontal and vertical components, the ensemble average for the first-order backscattered intensity may be written as

$$\begin{aligned} \langle E_{0\mu}^{(1)}(\bar{r}) E_{0\nu}^{(1)}(\bar{r})^* \rangle = & \sum_{j,k,l,m=1}^3 \int d^3\bar{r}_1 d^3\bar{r}_2 [G_{01\mu j}(\bar{r}, \bar{r}_1) E_{1\tau k}^{(0)}(\bar{r}_1)] \\ & [G_{01\nu l}(\bar{r}, \bar{r}_2) E_{1\kappa m}^{(0)}(\bar{r}_2)]^* \langle Q_{jk}(\bar{r}_1) Q_{lm}^*(\bar{r}_2) \rangle \end{aligned} \quad (57)$$

where the average of the components of the electric field has been computed by defining  $\mu$  and  $\nu$  as the received polarizations and  $\tau$  and  $\kappa$  as the transmitted polarizations.

As shown in Fig. 4, a horizontally or a vertically polarized incident electric field will generate both an ordinary and an extraordinary waves, due to the anisotropic permittivity in region 1, defined by their respective wave numbers [6]

$$k_{1zi}^o = \sqrt{\omega^2 \mu \epsilon_1 - k_{\rho i}^2}$$

$$\begin{aligned}
 k_{1zi}^{eo} &= -\frac{\epsilon_{23}}{\epsilon_{33}}k_{yi} + \frac{1}{\epsilon_{33}}\sqrt{\omega^2\mu\epsilon_1\epsilon_{1z}\epsilon_{33} - \epsilon_{1z}\epsilon_{33}k_{xi}^2 - \epsilon_{1z}\epsilon_{1z}k_{yi}^2} \\
 k_{1zi}^{ed} &= -\frac{\epsilon_{23}}{\epsilon_{33}}k_{yi} - \frac{1}{\epsilon_{33}}\sqrt{\omega^2\mu\epsilon_1\epsilon_{1z}\epsilon_{33} - \epsilon_{1z}\epsilon_{33}k_{xi}^2 - \epsilon_{1z}\epsilon_{1z}k_{yi}^2}
 \end{aligned}
 \quad (58)$$

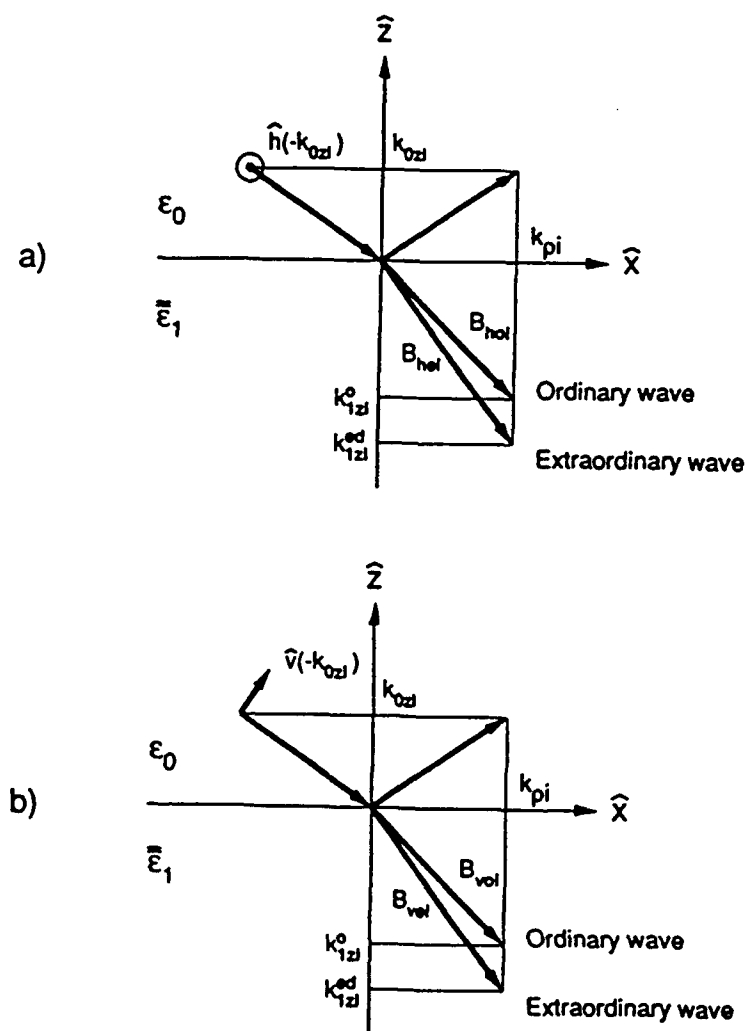


**Figure 4:** Ordinary and extraordinary electromagnetic waves excited by the anisotropic random medium. (a) Horizontally polarized incident electric field. (b) Vertically polarized electric field.

The components of the unperturbed electric field  $\bar{E}_1^{(0)}(\bar{r})$  and the Green's function  $\bar{G}_{01}(\bar{r}, \bar{r}_1)$  may be written as [7]

$$\bar{E}_{1\alpha}^{(0)}(\bar{r}) = \sum_{p=o, -o, eu, ed} E_{0\alpha i} X_{\alpha p i} \hat{p}(k_{1\alpha i}^p) e^{ik_{1\alpha i}^p \cdot \bar{r}} e^{i\bar{k}_{\alpha i} \cdot \bar{r}} \quad (59)$$

$$\bar{G}_{01\alpha}(\bar{r}, \bar{r}_1) = \frac{e^{ik_0 r}}{4\pi r} \sum_{p=o, -o, eu, ed} X_{\alpha p i} \hat{p}(k_{1\alpha i}^p) e^{ik_{1\alpha i}^p \cdot \bar{r}_1} e^{i\bar{k}_{\alpha i} \cdot \bar{r}_1} \quad (60)$$

where  $\alpha$  stands for either  $h$  or  $v$ , and  $p$  describes either an ordinary up-going wave ( $o$ ), an ordinary down-going wave ( $-o$ ), an extraordinary up-going ( $eu$ ), or an extraordinary down-going wave ( $ed$ ). Both the incident electric field and the Green's function are formed each by four terms meaning that backscattered electric field computed with Born first-order approximation will be constituted by sixteen terms. Furthermore, the coefficients  $X_{\alpha p i}$ , the unit vectors  $\hat{p}(k_{1\alpha i}^p)$ , and the wave numbers  $k_{1\alpha i}^p$  take on the following expressions depending on the value of  $p$

$$\begin{array}{lll} p = o \Rightarrow k_{1\alpha i}^p = k_{1\alpha i}^o & \hat{p}(k_{1\alpha i}^p) = \hat{o}(k_{1\alpha i}^o) & X_{\alpha p i} = A_{\alpha o i} \\ p = -o \Rightarrow k_{1\alpha i}^p = -k_{1\alpha i}^o & \hat{p}(k_{1\alpha i}^p) = \hat{o}(-k_{1\alpha i}^o) & X_{\alpha p i} = B_{\alpha o i} \\ p = eu \Rightarrow k_{1\alpha i}^p = k_{1\alpha i}^{eu} & \hat{p}(k_{1\alpha i}^p) = \hat{e}(k_{1\alpha i}^{eu}) & X_{\alpha p i} = A_{\alpha e i} \\ p = ed \Rightarrow k_{1\alpha i}^p = k_{1\alpha i}^{ed} & \hat{p}(k_{1\alpha i}^p) = \hat{e}(k_{1\alpha i}^{ed}) & X_{\alpha p i} = B_{\alpha e i} \end{array} \quad (61)$$

Hence, substituting (59) and (60) into (57) yields

$$\begin{aligned} \langle E_{0\mu}^{(1)}(\bar{r}) E_{0\nu}^{(1)*}(\bar{r}) \rangle &= \frac{\omega^4 \mu^2 |\epsilon_1|^2}{16\pi^2 r^2} E_{0\nu i} E_{0\alpha i}^* \sum_{j,k,l,m=1}^3 \sum_{p,q,r,s=o}^{ed} \\ & [X_{\mu p i} X_{r q i} \hat{p}(k_{1\alpha i}^p)_j \cdot \hat{q}(k_{1\alpha i}^q)_k] [X_{\nu r i} X_{s i} \hat{r}(k_{1\alpha i}^r)_l \cdot \hat{s}(k_{1\alpha i}^s)_m]^* \int d^3 \bar{r}_1 d^3 \bar{r}_2 \\ & \int d^3 \bar{\beta} \Phi_{jklm}(\bar{\beta}) e^{-i\bar{\beta} \cdot (\bar{r}_1 - \bar{r}_2)} \left[ e^{i(k_{1\alpha i}^p + k_{1\alpha i}^q) \cdot \bar{\beta}} e^{2i\bar{k}_{\alpha i} \cdot \bar{\beta}_1} \right] \left[ e^{i(k_{1\alpha i}^r + k_{1\alpha i}^s) \cdot \bar{\beta}} e^{2i\bar{k}_{\alpha i} \cdot \bar{\beta}_2} \right]^* \end{aligned} \quad (62)$$

As can be seen, all the polarization information is contained outside the integral. The parameters  $p$ ,  $q$ ,  $r$ , and  $s$  can take the values  $o$ ,  $-o$ ,  $eu$ , or  $ed$  as described in (61). The intensity is hence given by a sum of 256 terms. For each of these terms, 81 products (sum over  $jklm$ ) have to be computed due to the anisotropic behavior of the random medium. In order to simplify this result, let us define the two following scalar quantities

$$\Psi_{\mu\nu\alpha}^{pqrs} = X_{\mu p i} X_{r q i} X_{\nu r i}^* X_{s i}^* \quad (63)$$

$$\Omega_{jklm}^{pqrs} = [\hat{p}(k_{1\alpha i}^p)_j \cdot \hat{q}(k_{1\alpha i}^q)_k] [\hat{r}(k_{1\alpha i}^r)_l \cdot \hat{s}(k_{1\alpha i}^s)_m]^* \quad (64)$$

Hence, (62) may be written

$$\begin{aligned} \langle E_{0\mu}^{(1)}(\bar{r}) E_{0\nu}^{(1)}(\bar{r})^* \rangle &= \frac{\omega^4 \mu^2 |\epsilon_1|^2}{16\pi^2 r^2} E_{0\mu} E_{0\nu}^* \sum_{j,k,l,m=1}^3 \sum_{p,q,r,s=0}^{cd} \Psi_{\mu\tau\nu\kappa}^{pqrs} \Omega_{jklm}^{pqrs} \\ &\int d^3\bar{r}_1 d^3\bar{r}_2 \int d^3\bar{\beta} \Phi_{jklm}(\bar{\beta}) e^{-i\bar{\beta} \cdot (\bar{r}_1 - \bar{r}_2)} \left[ e^{i(k_{1z}^p + k_{1z}^q)z_1} e^{2i\bar{k}_{\rho 1} \cdot \bar{\rho}_1} \right] \left[ e^{i(k_{1z}^r + k_{1z}^s)z_2} e^{2i\bar{k}_{\rho 2} \cdot \bar{\rho}_2} \right]^* \end{aligned} \quad (65)$$

By following a similar procedure as in the isotropic case described in (37) through (45), the parameters  $a$  and  $b$  are first defined as

$$a = k_{1zi}^p + k_{1zi}^q \quad b = [k_{1zi}^r + k_{1zi}^s]^* \quad (66)$$

By assuming a spectrum density  $\Phi(\bar{\beta}_\rho, \beta_z)$  with  $n$  pairs of complex conjugate poles at  $\beta_z = \beta_{zn}^\pm$  and defining the following factors

$$I_{n+}^{pqrs} = \frac{1 - e^{-i(a - \beta_{zn}^+)d}}{(a - \beta_{zn}^+)(b - \beta_{zn}^+)} - \frac{1 - e^{-i(a-b)d}}{(a-b)(b - \beta_{zn}^+)} \quad (67)$$

$$I_{n-}^{pqrs} = \frac{1 - e^{-i(a-b)d}}{(a-b)(b - \beta_{zn}^-)} - \frac{e^{i(b - \beta_{zn}^-)d}}{(a - \beta_{zn}^-)(b - \beta_{zn}^-)} + \frac{e^{-i(a-b)d}}{(a - \beta_{zn}^-)(b - \beta_{zn}^-)} \quad (68)$$

the six polarimetric backscattering coefficients (11) are finally found to be [8]

$$\begin{aligned} \sigma_{\mu\tau\nu\kappa} &= 2\pi^2 \omega^4 \mu^2 |\epsilon_1|^2 \sum_{p,q,r,s=0}^{cd} \Psi_{\mu\tau\nu\kappa}^{pqrs} \sum_{j,k,l,m=1}^3 \Omega_{jklm}^{pqrs} \\ &i \sum_n \left\{ \text{Res} \Phi_{jklm}(\bar{\beta}_\rho = 2\bar{k}_{\rho i}, \beta_{zn}^+) I_{n+}^{pqrs} - \text{Res} \Phi_{jklm}(\bar{\beta}_\rho = 2\bar{k}_{\rho i}, \beta_{zn}^-) I_{n-}^{pqrs} \right\} \end{aligned} \quad (69)$$

Compared to the results of the isotropic case shown in (46) and (47), there is no zero elements. This is due to the anisotropic behavior and the excitation of both ordinary and extraordinary waves.

## Born Second-Order Approximation

For this case, only the isotropic random permittivity will be considered. From (21), the second-order scattered electric field is given by

$$\bar{E}_0^{(2)}(\bar{r}) = \int d^3\bar{r}_1 d^3\bar{r}_2 \bar{G}_{01}(\bar{r}, \bar{r}_1) Q(\bar{r}_1) \cdot \bar{G}_{11}(\bar{r}_1, \bar{r}_2) Q(\bar{r}_2) \cdot \bar{E}_1^{(0)}(\bar{r}_2) \quad (70)$$

where  $\bar{E}_1^{(0)}(\bar{r})$  and  $\bar{G}_{01}(\bar{r}, \bar{r}_1)$  are given by (30) and (31), respectively. The Green's function  $\bar{G}_{11}(\bar{r}_1, \bar{r}_2)$  relates the field observed in region 1 at a position  $\bar{r}_1$  due to a source in region 1 located at  $\bar{r}_2$ . It takes the following form from [9]

$$\bar{G}_{11}(\bar{r}_1, \bar{r}_2) = \frac{i}{8\pi^2} \int d^2\bar{k}_\rho \left\{ \begin{array}{l} \bar{g}_{11}^>(\bar{k}_\rho, z_1, z_2) \\ \bar{g}_{11}^<(\bar{k}_\rho, z_1, z_2) \end{array} \right\} e^{i\bar{k}_\rho \cdot (\bar{r}_1 - \bar{r}_2)} \quad \left\{ \begin{array}{l} z_1 > z_2 \\ z_1 < z_2 \end{array} \right. \quad (71)$$

where

$$\bar{g}_{11}^>(\bar{k}_\rho, z_1, z_2) = \frac{1}{k_{1z}} \sum_{q,r=-1}^1 e^{iqk_{1z}z_1} e^{ir k_{1z}z_2} \sum_{\alpha=h,v} C_{\alpha q r}^>(\bar{k}_\rho) \hat{\alpha}(qk_{1z}) \hat{\alpha}(-rk_{1z}) \quad (72)$$

$$\bar{g}_{11}^<(\bar{k}_\rho, z_1, z_2) = \frac{1}{k_{1z}} \sum_{q,r=-1}^1 e^{iqk_{1z}z_1} e^{ir k_{1z}z_2} \sum_{\alpha=h,v} C_{\alpha q r}^<(\bar{k}_\rho) \hat{\alpha}(qk_{1z}) \hat{\alpha}(-rk_{1z}) \quad (73)$$

Here  $\alpha$  denotes the polarization direction along  $h$  or  $v$ , and the coefficients  $C$  take the following values [3]

$$\begin{aligned} C_{h11}^>(\bar{k}_\rho) &= C_{h11}^<(\bar{k}_\rho) = R_{12} e^{i2k_{1z}d} / D_2 & C_{h1-1}^>(\bar{k}_\rho) &= C_{h-11}^<(\bar{k}_\rho) = 1/D_2 \\ C_{h-11}^>(\bar{k}_\rho) &= C_{h1-1}^<(\bar{k}_\rho) = R_{10} R_{12} e^{i2k_{1z}d} / D_2 & C_{h-1-1}^>(\bar{k}_\rho) &= C_{h-1-1}^<(\bar{k}_\rho) = R_{10} / D_2 \\ C_{v11}^>(\bar{k}_\rho) &= C_{v11}^<(\bar{k}_\rho) = S_{12} e^{i2k_{1z}d} / F_2 & C_{v1-1}^>(\bar{k}_\rho) &= C_{v-11}^<(\bar{k}_\rho) = 1/F_2 \\ C_{v-11}^>(\bar{k}_\rho) &= C_{v1-1}^<(\bar{k}_\rho) = S_{10} S_{12} e^{i2k_{1z}d} / F_2 & C_{v-1-1}^>(\bar{k}_\rho) &= C_{v-1-1}^<(\bar{k}_\rho) = S_{10} / F_2 \end{aligned} \quad (74)$$

The physical meaning of the Born second-order approximation (70) are interpreted based on the fact that  $\bar{G}_{01}(\bar{r}, \bar{r}_1)$ ,  $\bar{G}_{11}(\bar{r}_1, \bar{r}_2)$ , and  $\bar{E}_1^{(0)}(\bar{r})$  are composed of a down- and an up-going wave for each polarization. Therefore,  $\bar{E}_0^{(1)}(\bar{r})$  is formed by the sum of sixteen different terms as shown in Fig. 5. All the multiple reflections occurring at the boundaries are accounted for and the backscattered wave is due to the double scattering process under the Born second-order approximation.

With (30), (31), and (70), the ensemble average for the second-order intensity is given by

$$\begin{aligned} \langle E_{0\mu}^{(2)}(\bar{r}) E_{0\nu}^{(2)*}(\bar{r}) \rangle &= \int d^3\bar{r}_1 d^3\bar{r}_2 d^3\bar{r}_3 d^3\bar{r}_4 \langle Q(\bar{r}_1) Q(\bar{r}_2) Q(\bar{r}_3)^* Q(\bar{r}_4)^* \rangle \\ &\quad \left[ \bar{G}_{01\mu}(\bar{r}, \bar{r}_1) \cdot \bar{G}_{11}(\bar{r}_1, \bar{r}_2) \cdot \bar{E}_{1\nu}^{(0)}(\bar{r}_2) \right] \left[ \bar{G}_{01\nu}(\bar{r}, \bar{r}_3) \cdot \bar{G}_{11}(\bar{r}_3, \bar{r}_4) \cdot \bar{E}_{1\mu}^{(0)*}(\bar{r}_4) \right]^* \quad (75) \end{aligned}$$

where  $\mu$ ,  $\nu$ ,  $\tau$ , and  $\kappa$  represent either the horizontal or vertical polarization. Furthermore,  $\mu$  and  $\nu$  are associated with the receiver whereas  $\tau$  and  $\kappa$  are associated with the transmitter. By assuming gaussian random variables and considering only the backscattering direction, the random term of (75) may be written as a sum of two terms

$$\begin{aligned} \langle Q(\bar{r}_1)Q(\bar{r}_2)Q(\bar{r}_3)^*Q(\bar{r}_4)^* \rangle = & \langle Q(\bar{r}_1)Q(\bar{r}_3)^* \rangle \langle Q(\bar{r}_2)Q(\bar{r}_4)^* \rangle \\ & + \langle Q(\bar{r}_1)Q(\bar{r}_4)^* \rangle \langle Q(\bar{r}_2)Q(\bar{r}_3)^* \rangle \end{aligned} \quad (76)$$

$$\bar{G}_{01}(\bar{r}, \bar{r}_1) \quad \times \quad \bar{G}_{11}(\bar{r}_1, \bar{r}_2) \quad \times \quad \bar{E}_1^{(0)}(\bar{r}_2)$$

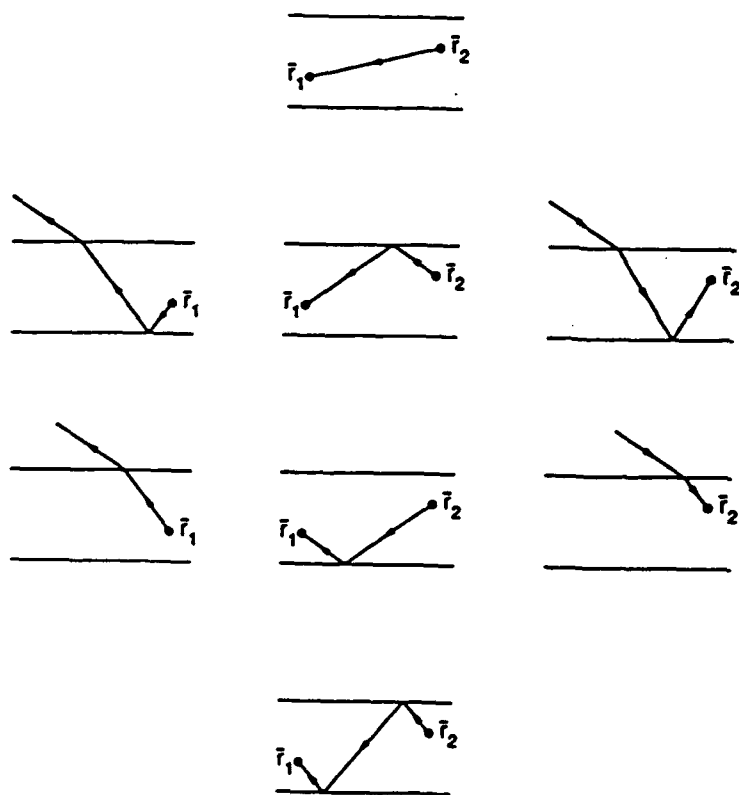


Figure 5: Physical interpretation for Born second-order approximation.

Similarly to (28), by using the spectrum density of the autocorrelation function and integrating over the lateral variables, the ensemble average takes the following form

$$\begin{aligned}
 \langle E_{0\mu}^{(2)}(\bar{r}) E_{0\nu}^{(2)}(\bar{r})^* \rangle &= \frac{\delta^2 \omega^8 \mu^4 |\epsilon_{1m}|^4 A}{16r^2} E_{0\tau i} E_{0\alpha i}^* \int d^2 \bar{k}_\rho \int dz_1 dz_2 dz_3 dz_4 \\
 &\int d\beta_{z1} d\beta_{z2} \Phi(\bar{k}_\rho + \bar{k}_\rho, \beta_{z1}) \Phi(\bar{k}_\rho - \bar{k}_\rho, \beta_{z2}) \frac{1}{|k_{1z}|^2} \sum_{\substack{p, q, r, s \\ p', q', r', s' = -1}}^1 \Psi_{\mu\nu\kappa}^{p, p', s, s'} \\
 &e^{i(p k_{1z} + q k_{1z})z_1} e^{i(s k_{1z} + r k_{1z})z_2} e^{-i(p' k_{1z} + q' k_{1z})z_3} e^{-i(s' k_{1z} + r' k_{1z})z_4} \sum_{\alpha, \gamma = h, v} \Upsilon_{\alpha\gamma\delta_1\delta_2}^{q, q', r, r'}(\bar{k}_\rho) \\
 &\left\{ \Omega_{\mu\nu\kappa, \alpha\gamma}^{p, p', s, s'}(\bar{k}_\rho) e^{-i\beta_{z1}(z_1 - z_3)} e^{-i\beta_{z2}(z_2 - z_4)} \right. \\
 &\left. + \Omega_{\mu\nu\kappa, \alpha\gamma}^{p, p', s, s'}(-\bar{k}_\rho) e^{-i\beta_{z1}(z_1 - z_4)} e^{-i\beta_{z2}(z_2 - z_3)} \right\} \quad (77)
 \end{aligned}$$

where the following terms have been defined

$$\Psi_{\mu\nu\kappa}^{p, p', s, s'} = X_{\mu p i} X_{\tau s i} X_{\nu p' i}^* X_{\kappa s' i}^* \quad (78)$$

$$\Upsilon_{\alpha\gamma\delta_1\delta_2}^{q, q', r, r'}(\bar{k}_\rho) = C_{\alpha q}^{\delta_1}(\bar{k}_\rho) C_{\gamma q'}^{\delta_2}(\bar{k}_\rho) \quad (79)$$

$$\begin{aligned}
 \Omega_{\mu\nu\kappa, \alpha\gamma}^{p, p', s, s'}(\bar{k}_\rho) &= [\hat{\mu}(p k_{1z}) \cdot \hat{\alpha}(q k_{1z}) \hat{\alpha}(-r k_{1z}) \cdot \hat{\tau}(s k_{1z})] \\
 &[\hat{\nu}(p' k_{1z}) \cdot \hat{\gamma}(q' k_{1z}) \hat{\gamma}(-r' k_{1z}) \cdot \hat{\kappa}(s' k_{1z})]^* \quad (80)
 \end{aligned}$$

$$\begin{aligned}
 \Omega_{\mu\nu\kappa, \alpha\gamma}^{p, p', s, s'}(-\bar{k}_\rho) &= [\hat{\mu}(p k_{1z}) \cdot \hat{\alpha}(q k_{1z}) \hat{\alpha}(-r k_{1z}) \cdot \hat{\tau}(s k_{1z})] \\
 &[\hat{\nu}(p' k_{1z}) \cdot \hat{\gamma}(-q' k_{1z}) \hat{\gamma}(r' k_{1z}) \cdot \hat{\kappa}(s' k_{1z})]^* \quad (81)
 \end{aligned}$$

In the polar coordinate system, (77) becomes

$$\begin{aligned}
 \langle E_{0\mu}^{(2)}(\bar{r}) E_{0\nu}^{(2)}(\bar{r})^* \rangle &= \frac{\delta^2 \omega^8 \mu^4 |\epsilon_{1m}|^4 \pi A}{64r^2} E_{0\tau i} E_{0\alpha i}^* \int dk_\rho \int dz_1 dz_2 dz_3 dz_4 \\
 &\frac{k_\rho}{|k_{1z}|^2} \sum_{\substack{p, q, r, s \\ p', q', r', s' = -1}}^1 \Psi_{\mu\nu\kappa}^{p, p', s, s'} e^{i(p k_{1z} + q k_{1z})z_1} e^{i(s k_{1z} + r k_{1z})z_2} e^{-i(p' k_{1z} + q' k_{1z})z_3} e^{-i(s' k_{1z} + r' k_{1z})z_4} \\
 &\sum_{\alpha, \gamma = h, v} \Upsilon_{\alpha\gamma\delta_1\delta_2}^{q, q', r, r'}(k_\rho) \left\{ \Omega_{\mu\nu\kappa, \alpha\gamma}^{p, p', s, s'}(k_\rho) \int d\beta_{z1} d\beta_{z2} \Phi(k_\rho + k_\rho, \beta_{z1}) \Phi(k_\rho - k_\rho, \beta_{z2}) \right. \\
 &e^{-i\beta_{z1}(z_1 - z_3)} e^{-i\beta_{z2}(z_2 - z_4)} + \Omega_{\mu\nu\kappa, \alpha\gamma}^{p, p', s, s'}(-k_\rho) \int d\beta_{z1} d\beta_{z2} \Phi(k_\rho + k_\rho, \beta_{z1}) \\
 &\left. \Phi(k_\rho - k_\rho, \beta_{z2}) e^{-i\beta_{z1}(z_1 - z_4)} e^{-i\beta_{z2}(z_2 - z_3)} \right\} \quad (82)
 \end{aligned}$$

where the integration over  $\phi$  has yielded [3]

$$\frac{4}{\pi} \int_0^{2\pi} d\phi \Omega_{\mu\nu\kappa, \alpha\gamma}^{p, p', s, s'}(\bar{k}_\rho) = \Omega_{\mu\nu\kappa, \alpha\gamma}^{p, p', s, s'}(k_\rho) \quad (83)$$

$$\frac{1}{\pi} \int_0^{2\pi} d\phi \Omega_{\mu\nu\kappa,\alpha\gamma}^{pqrs,p'q'r's'}(-\bar{k}_\rho) = I_{\mu\nu\kappa,\alpha\gamma}^{pqrs,p'-q-r's'}(k_\rho) \quad (84)$$

Using the Cauchy's theorem, the integration over  $\beta_{z1}$  and  $\beta_{z2}$  may be carried out. The final result for the polarimetric backscattering coefficients are obtained [3]

$$\begin{aligned} \sigma_{\mu\nu\kappa} &= \frac{\pi^4 \delta^2 \omega^8 \mu^4 |\epsilon_{1m}|^4}{4} \int dk_\rho \frac{k_\rho}{|k_{1z}|^2} iRes\Phi(k_\rho + k_\rho, \beta_z^+) \\ iRes\Phi(k_\rho - k_\rho, \beta_z^+) &= \sum_{\substack{p,q,r,s,p',q',r',s' \\ p',q',r',s'=-1}}^1 \Psi_{\mu\nu\kappa}^{pqrs,p'q'r's'} \sum_{\alpha,\gamma=h,v} \sum_{\xi_1, \xi_2=-1}^1 \Upsilon_{\alpha\gamma, \xi_1 \xi_2}^{pqrs,p'q'r's'}(k_\rho) \\ &\{ I_{\mu\nu\kappa,\alpha\gamma}^{pqrs,p'q'r's'}(k_\rho) M_{\xi_1 \xi_2}^{pqrs,p'q'r's'}(k_\rho) + I_{\mu\nu\kappa,\alpha\gamma}^{pqrs,p'-q-r's'}(k_\rho) N_{\xi_1 \xi_2}^{pqrs,p'q'r's'}(k_\rho) \} \quad (85) \end{aligned}$$

The factors  $M$  and  $N$  are defined in [3]. It is noted that the integral over  $k_\rho$  cannot be solved analytically but only numerically. From the integration over the azimuthal variable  $\phi$  in (83) and (84), it is found that  $\sigma_{hvv} = \sigma_{hhv} = 0$ . However, the depolarization term  $\sigma_{hv}$  is different from zero, unlike the result obtained with the isotropic Born first-order approximation.



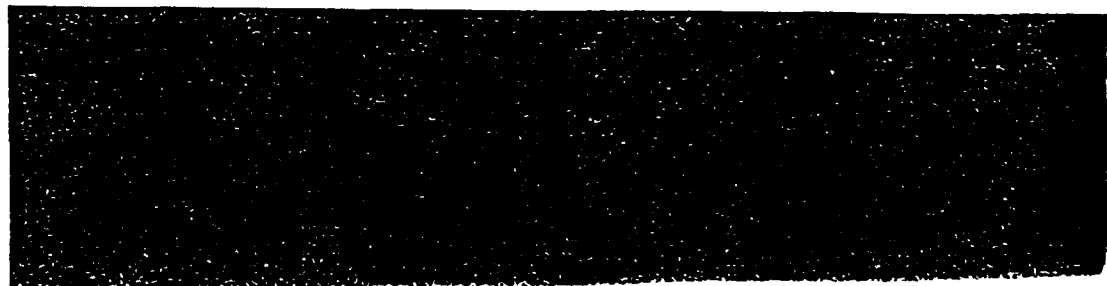
## Results

### a) Born first-order approximation

With the Born first-order approximation, the polarimetric backscattering coefficients have been obtained for the two-layer isotropic and anisotropic random medium configurations. For the anisotropic random medium, the depolarization term  $\sigma_{hv} \neq 0$  exists even with Born first-order approximation. In general, all the backscattering coefficients  $\sigma_{hh}$ ,  $\sigma_{hv}$ ,  $\sigma_{vv}$ ,  $\sigma_{hhvv}$ ,  $\sigma_{hhhv}$ ,  $\sigma_{hvvv}$ , are different from zero for the anisotropic case. However, when  $\psi = \psi_f = 0^\circ$  but  $\epsilon_1 \neq \epsilon_{1z}$ , no depolarization term is obtained for this uniaxial untilted case and  $\sigma_{hv} = \sigma_{hhhv} = \sigma_{hvvv} = 0$ . Also, for  $\psi = 0$  but  $\psi_f \neq 0$ , the non-zero depolarization terms  $\sigma_{hhhv}$  and  $\sigma_{hvvv}$  are obtained. Finally, when  $\psi \neq 0$ , all the backscattering coefficients are different from zero. In a similar manner, when  $\phi = 90^\circ$ , implying that the plane of incidence contains the scatterers, there is no depolarization factor, and only three backscattering coefficients are different from zero ( $\sigma_{hv} = \sigma_{hhhv} = \sigma_{hvvv} = 0$ ).

Fig. 6 illustrates dependence of the backscattering coefficients on the angle of incidence for  $\sigma_{hh}$ ,  $\sigma_{vv}$  and  $\sigma_{hv}$  for a two-layer configuration, and these results are matched with experimental data for sea ice taken in 1984 in Point Barrow in Alaska by [10]. The input parameters  $\epsilon_1$ ,  $\epsilon_{1z}$ ,  $\delta$ , and  $\delta_z$  are obtained using the strong fluctuation theory developed in [11]. The tilt angle is chosen to be  $\psi = \psi_f = 20^\circ$ , and the azimuthal angle is assumed to be  $\phi = 20^\circ$ . The good correspondence is noted between the experimental results and the theoretical predictions. Fixing the incident angle at  $\theta_{oi} = 40^\circ$  in Fig. 6, the covariance matrix for the backscattering coefficient (14) is shown in Fig. 7. As can be seen, this matrix does not contain any zero elements.

For an earth terrain medium such as trees or grass, leaves grow randomly in the azimuthal direction. This can be modeled by assuming that one patch illuminated by the radar is oriented in a certain direction whereas the next patch is oriented in a different direction and so on. To obtain the backscattering coefficients, the average over many patches should be taken. This model is used in the theory by assuming a fixed direction of the scatterers but modifying the position of the radar over the azimuthal direction. This is shown in Fig. 8 for grass and in Fig. 9 for trees where both these vegetation fields are simulated by averaging the backscattering coefficients over  $\phi$ . The step of averaging is  $\Delta\phi = 1^\circ$ . Though the tilt angle  $\psi$  is different from zero, there is a depolarization factor ( $\sigma_{hv} \neq 0$ ), but  $\sigma_{hhhv} = \sigma_{hvvv} = 0$ . This is due to symmetrical reasons because the contribution of these two backscattering coefficients at  $\phi$  is cancelled by the one at  $180^\circ - \phi$ . Also in Fig. 8 and in Fig. 9, experimental polarimetric radar data obtained by MIT Lincoln Laboratory are displayed [14]. The frequency of operation was 35 GHz, and the angle of incidence was  $82^\circ$  (depression angle of  $8^\circ$ ). The radar illuminated on a vegetation field consisting of either grass or trees at a range of  $\sim 2$  km. A good correspondence between the theoretical predictions and the experimental results is obtained.



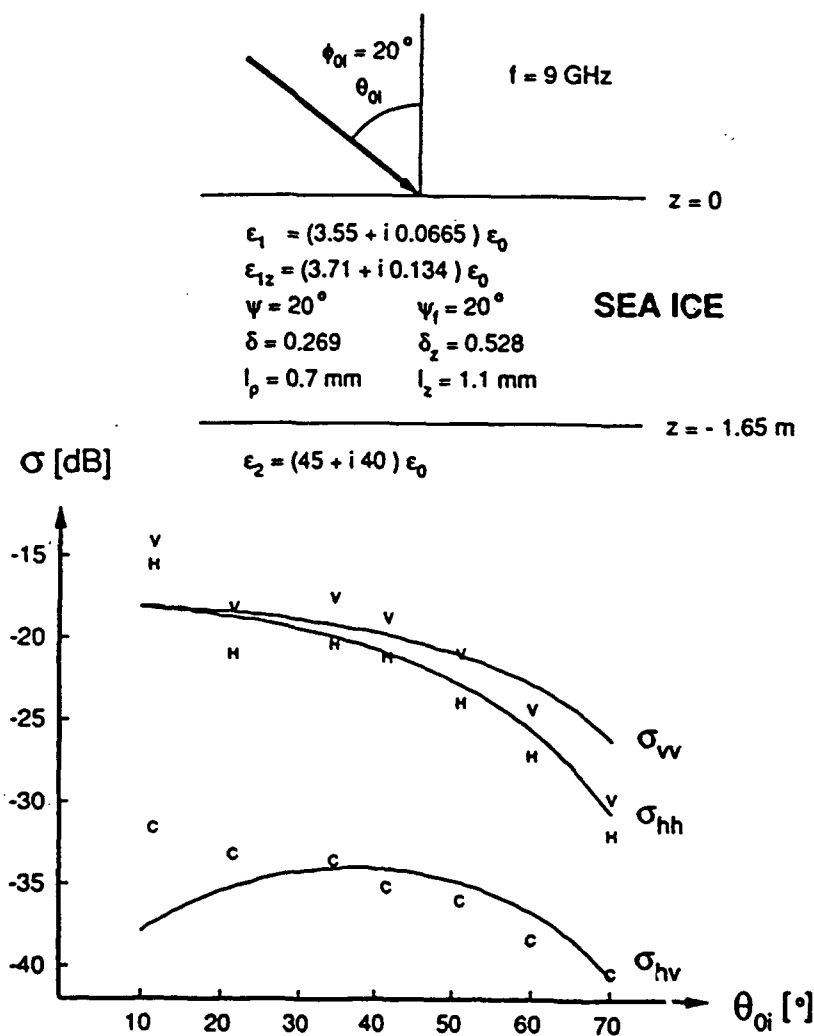
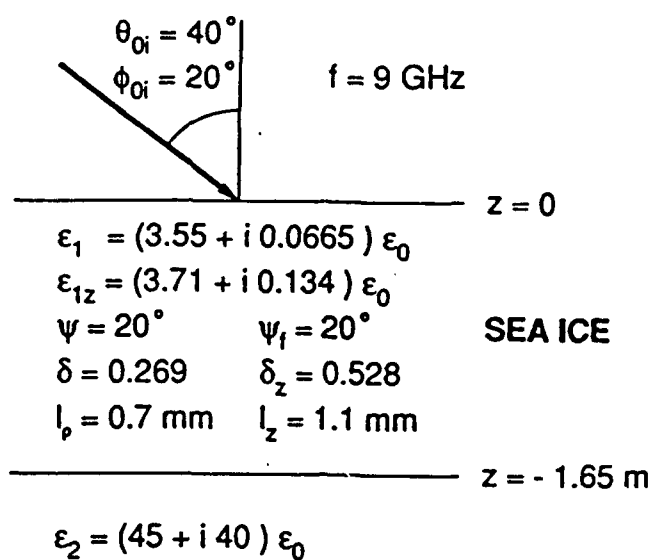


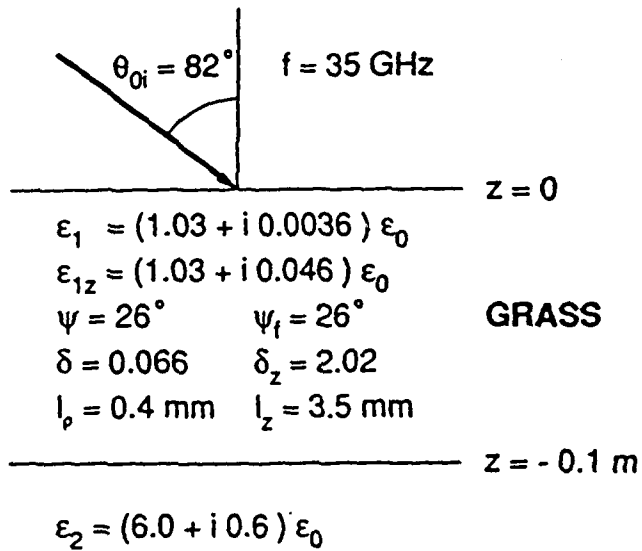
Figure 6: Backscattering coefficient at 9 GHz as a function of incident polar angle matched for sea ice.



Covariance matrix:

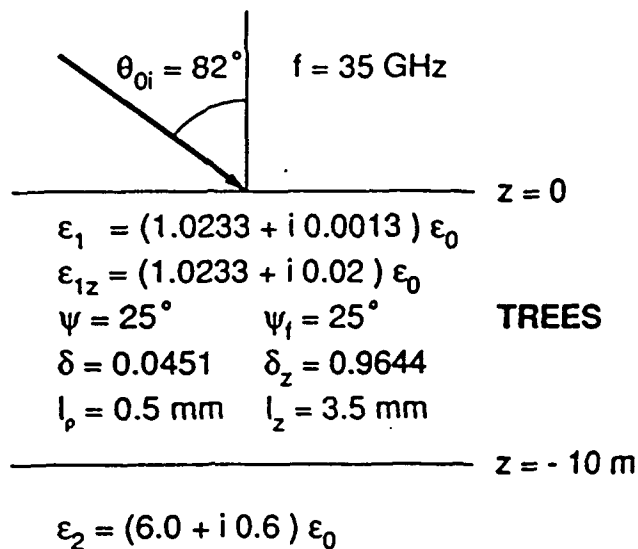
$$10^{-3} \cdot \begin{pmatrix} 8.43 & 0.23 + i 1.18 & 9.40 - i 0.76 \\ 0.23 - i 1.18 & 0.39 & 0.02 - i 1.34 \\ 9.40 + i 0.76 & 0.02 + i 0.134 & 10.6 \end{pmatrix}$$

Figure 7: Covariance matrix for the backscattering coefficients at  $\theta_{oi} = 40^\circ$  for sea ice.



	$\sigma_{hh} \text{ (dB)}$	$\frac{\sigma_{hv}}{\sigma_{hh}}$	$\frac{\sigma_{vw}}{\sigma_{hh}}$	$\frac{\text{Re}(\sigma_{hhvw})}{\sqrt{\sigma_{hh} \sigma_{vw}}}$	$\frac{\text{Im}(\sigma_{hhvw})}{\sqrt{\sigma_{hh} \sigma_{vw}}}$
Experiment	-14.5	0.19	1.4	0.54	0.03
Born	-14.4	0.17	1.3	0.59	0.04

Figure 8: Covariance matrix elements for grass region using the average over the azimuthal angle  $\phi$  with  $\Delta\phi = 1^\circ$ . Experimental measurements and theoretical calculations are shown.



	$\sigma_{hh} \text{ (dB)}$	$\frac{\sigma_{hv}}{\sigma_{hh}}$	$\frac{\sigma_{vw}}{\sigma_{hh}}$	$\frac{\text{Re}(\sigma_{hhvw})}{\sqrt{\sigma_{hh} \sigma_{vw}}}$	$\frac{\text{Im}(\sigma_{hhvw})}{\sqrt{\sigma_{hh} \sigma_{vw}}}$
Experiment	-10.8	0.12	1.2	0.64	0.01
Born	-10.6	0.12	1.2	0.65	0.05

Figure 9: Covariance matrix elements for tree region using the average over the azimuthal angle  $\phi$  with  $\Delta\phi = 1^\circ$ . Experimental measurements and theoretical calculations are shown.

## b) Born second-order approximation

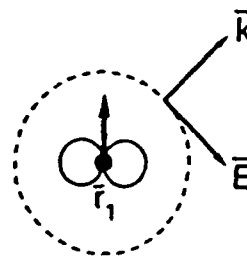
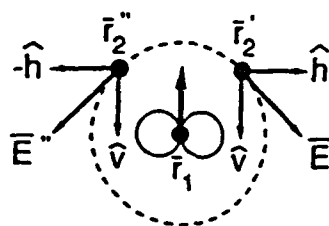
Unlike the isotropic Born first-order approximation, a depolarization factor  $\sigma_{hv} \neq 0$  is obtained with the isotropic Born second-order approximation [9]. Furthermore, it was shown that  $\sigma_{hhvv} = \sigma_{hvvv} = 0$ . Hence, the covariance matrix can be written from (11)

$$\bar{C} = \begin{pmatrix} \sigma_{hh} & 0 & \sigma_{hhvv} \\ 0 & \sigma_{hv} & 0 \\ \sigma_{hhvv}^* & 0 & \sigma_{vv} \end{pmatrix} \quad (86)$$

Although a mathematical proof has been used to show that five elements of the covariance matrix are zero, this fact may also be illustrated from a physical point of view. Let us concentrate on the term  $\sigma_{vvhr}$  which is proportional to  $\langle VV \cdot HV^* \rangle$  from (11). By assuming that a vertically polarized electric field is transmitted, symbolized by  $\hat{v}$  in Fig. 10, the product of the waves polarized in the horizontal and vertical directions at the receiver is taken. The wave hits a first scatterer at position  $\bar{r}_1$  and then hits a second scatterer at position  $\bar{r}_2$ . At that location, the electric field  $\bar{E}$  induces a dipole which can be decomposed into horizontal and vertical components. From that point, the wave is backscattered and the receiver collects either  $HV^*$  or  $VV$ . Due to symmetry reasons, the second scatterer may be located at position  $\bar{r}_2'$ . The corresponding electric field  $\bar{E}'$  is decomposed into a vertical component and a horizontal component which is in the opposite direction from the component created by  $\bar{r}_2$ . At the receiver, either  $HV^*$  or  $VV$  is collected. In order to obtain  $\sigma_{vvhr}$ , the product of these two quantities must be taken. However, the product created by the location at  $\bar{r}_2$  will have an opposite sign from the one created at the location  $\bar{r}_2'$ . By taking the average, these two contributions cancel and  $\sigma_{vvhr} = 0$  is obtained. Similarly for every point, there is a symmetric scatterer which will cancel its contribution.

The depolarization factor is proportional to  $\langle HV \cdot HV^* \rangle$ , i.e., a vertically polarized electric field is transmitted and the horizontal component of the scattered field is received. Unlike the term  $\langle VV \cdot HV^* \rangle$ , both quantities  $HV$  and  $HV^*$  due to the dipole at location  $\bar{r}_2'$  are in the opposite direction from the ones created by the scatterer at  $\bar{r}_2$ . This implies that the product of the two quantities, which have the same sign independent of the position of the second scatterer  $\bar{r}_2'$  or  $\bar{r}_2''$ , renders the average backscattering coefficient  $\sigma_{hv}$  different from zero as shown in Fig. 11.

Incident wave

First scatterer at  $\vec{r}_1$ Second scatterer at  $\vec{r}_2$ 

Backscattering

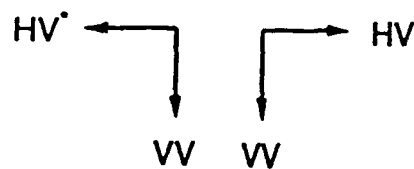


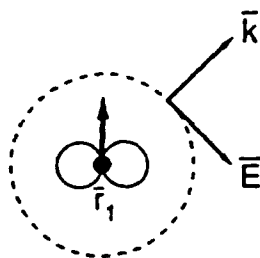
Figure 10: Interpretation of the term  $\langle VV \cdot HV^* \rangle$  with the Born second order approximation.

1:96

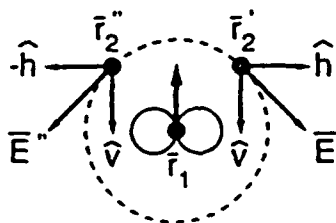
Incident wave



First scatterer at  $\vec{r}_1$



Second scatterer at  $\vec{r}_2$



Backscattering

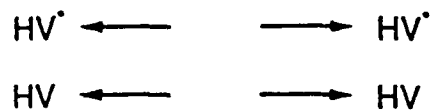


**Figure 11:** Interpretation of the term  $\langle HV \cdot HV^* \rangle$  with the Born second order approximation.



### c) Strong permittivity fluctuation theory

The variance of permittivity fluctuations is usually large in geophysical media consisting of mixtures of constituents with very different properties. With the diagrammatic approach [1], the propagation and scattering in random media can be studied. The diagrammatic approach leads to the Dyson's equation for the mean field. It should be noted that in solving Dyson's equation with the bilocal approximation, both the observation point and the source point within the random medium can coincide with each other in the domain of integration. To take care of the singular nature of the dyadic Green's functions, a strong permittivity fluctuation theory that applies to both small and large variances of the permittivity functions has been developed [11].

The mean field and the mean Green's function are calculated by replacing the medium with an equivalent medium having an effective permittivity which accounts for losses due to both absorption and scattering.

It should be emphasized that the effect of the random medium on electromagnetic waves is better described with the strong permittivity fluctuation theory than in the case of the traditional "weak permittivity fluctuations". For the case of a random medium described by a mixture of two components, only the fractional volume, the correlation lengths, the permittivity of the two components, and the frequency are necessary to describe the effect of the earth terrain. The other parameters, that is the variances and the mean permittivities, needed for the Born approximation are computed with the strong permittivity fluctuation theory.

In order to illustrate the results of the strong permittivity fluctuation theory, we compare  $\sigma_{hh}$  in Fig. 12 obtained with the weak permittivity fluctuation theory compared with the strong permittivity fluctuation theory. We use a correlation function exponentially decaying in all directions with  $l_p = l_z = 0.3$  mm. The physical parameters chosen in Fig. 12 characterized a layer of dry snow [13]. In Fig. 12, we plot  $\sigma_{hh}$  in the function of the frequency for  $\theta_0 = 60^\circ$ . As shown, the results obtained with the strong permittivity fluctuation theory are smaller than those obtained with the weak permittivity fluctuation theory. This difference gets larger with increasing frequencies. This is due to the fact that the losses due to scattering, which increase with increasing frequencies, are taken into account in the strong permittivity fluctuation theory.

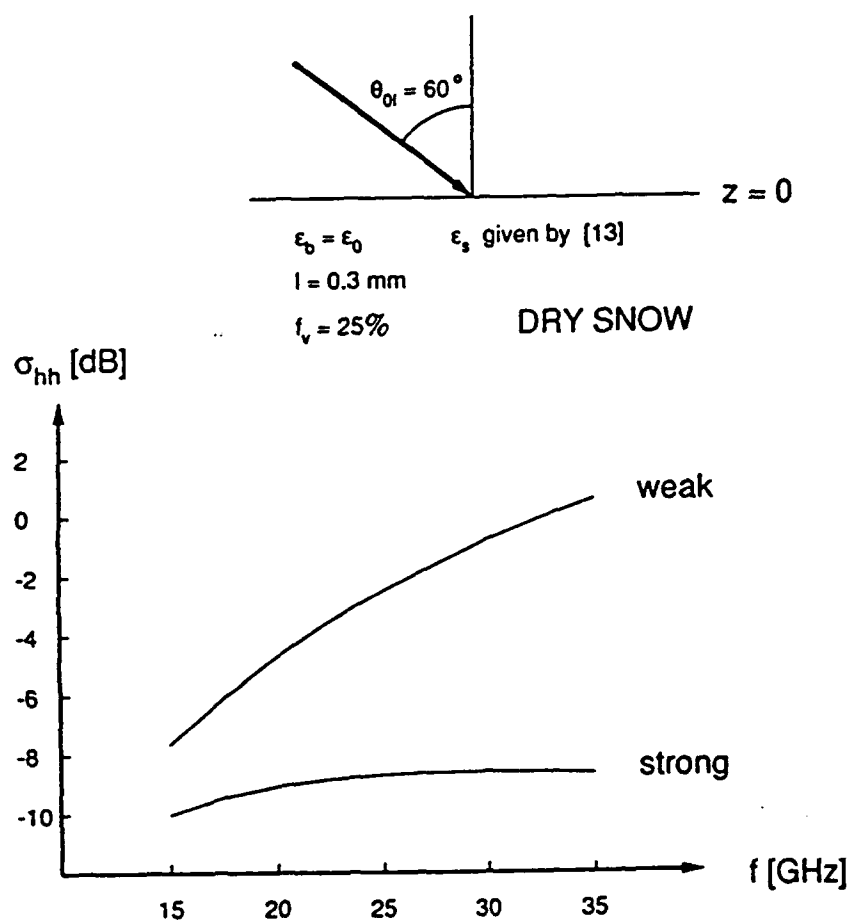


Figure 12: Backscattering coefficient  $\sigma_{hh}$  in function of the frequency computed with the weak and strong permittivity fluctuation theories.

## References

- [1] L. Tsang, J.A. Kong, and R.T. Shin, *Theory of Microwave Remote Sensing*, John Wiley & Sons, New-York, 1985.
- [2] J.R. Huynen, "Measurement of the Target Scattering Matrix," *Proceedings of the IEEE*, Vol. 53, No. 8, pp. 936-946, August 1965.
- [3] M. Borgeaud, "Theoretical Models for Polarimetric Microwave Remote Sensing of Earth Terrain," *Ph.D. Thesis*, Department of Electrical Engineering and Computer Science, Massachusetts Institute of Technology, December 1987.
- [4] M.A. Zuniga and T.M. Habashy. "Active Remote Sensing of Layered Random Media," *IEEE Transactions on Geoscience Electronics*, Vol. GE-17, No. 4, pp. 296-302, October 1979.
- [5] M.A. Zuniga and J.A. Kong. "Active Remote Sensing of Random Media," *Journal of Applied Physics*, Vol. 51, No. 1, pp. 74-79, January 1980.
- [6] J.K. Lee and J. A. Kong, "Active Microwave Remote Sensing of an Anisotropic Random Medium Layer," *IEEE Transactions on Geoscience and Remote Sensing*, Vol. GE-23, No. 6, pp. 910 - 923, November 1985.
- [7] J.K. Lee and J.A. Kong, "Dyadic Green's Functions for Layered Anisotropic Medium," *Electromagnetics*, Vol. 3, pp. 111-130, 1983.
- [8] M. Borgeaud, J.A. Kong and R.T. Shin, "Polarimetric Radar Clutter Modeling with a Two-layer Anisotropic Random Medium," *International Union of Radio Science, Commission F, U.R.S.I. Meeting*, pp. 4.4.1-4.4.4. Durham, New Hampshire, July 28 - August 1, 1986.
- [9] M.A. Zuniga, J.A. Kong, and L. Tsang. "Depolarization Effects in the Active Remote Sensing of Random Media," *Journal of Applied Physics*, Vol. 51, No. 5, pp. 2315-2325, May 1980.
- [10] Y.S. Kim, R.K. Moore, and R.G. Onstott, "Theoretical and Experimental Study of Radar Backscattered from Sea Ice," *Technical Report*, Remote Sensing Laboratory, University of Kansas, Lawrence, January 1984.
- [11] L. Tsang and J.A. Kong. "Scattering of Electromagnetic Waves from Random Media with Strong Permittivity Fluctuations," *Radio Science*, Vol. 16, No. 3, pp. 303-320, May-June 1981.
- [12] M. Borgeaud, R.T. Shin, and J.A. Kong, "Theoretical Models for Polarimetric Radar Clutter," *Journal of Electromagnetic Waves and Applications*, Vol. 1, No. 1, pp. 73-89, 1987.
- [13] M.E. Tiuri, A.H. Shivola, E.G. Nyfors, and T.M. Hallikainen. "The Complex Dielectric Constant of Snow at Microwave Frequencies," *IEEE Journal of Oceanic Engineering*, Vol. OE-9, No. 5, pp. 377-382, December 1984.
- [14] J.A. Kong, F.C. Lin, M. Borgeaud, H.A. Yueh, A.A. Swartz, H.H. Lim, I.M. Novak, and R.T. Shin. "Polarimetric Clutter Modeling: Theory and Applications," *GACIAC PR-88-03, The Polarimetric Technology Workshop*, Redstone Arsenal, U.S. Army Missile Command, Huntsville, Alabama, August 16-19, 1988.